

APPROVAL SHEET

Title of Dissertation: Data-driven Techniques for the Study of Brain Dynamics and Identification of Subgroups: Application to Multi-subject Resting-state fMRI Data

Name of Candidate: Qunfang Long
Doctor of Philosophy, 2020

Dissertation and Abstract Approved: _____
Dr. Tülay Adalı
Distinguished University Professor
Department of Computer Science and
Electrical Engineering

Date Approved: _____

ABSTRACT

Title of Dissertation: Data-driven Techniques for the Study of Brain Dynamics and Identification of Subgroups: Application to Multi-subject Resting-state fMRI Data

Qunfang Long, Doctor of Philosophy, 2020

Dissertation directed by: Dr. Tülay Adalı
Distinguished University Professor
Department of Computer Science and
Electrical Engineering

Functional magnetic resonance imaging (fMRI) captures the blood-oxygen-level-dependent (BOLD) response and has been a valuable tool for understanding human brain function. Data-driven techniques have proven to be very effective in fMRI analysis and identified unique biomedical patterns in neurological disorders such as in schizophrenia (SZ), atrophy, degenerative dementias, Alzheimer's disease, and many others. There are a number of data-driven techniques developed for fMRI analysis to extract functional networks and their associated properties, but there are still a number of important challenges. First, there is a need to better understand the properties of different approaches to be able to select the best method for a given scenario. Then, a big challenge has been capturing the subject variability while simultaneously performing analysis on multi-subject fMRI. This motivates the development of a method that is able to preserve variabilities across datasets, so that one can identify statistically significant groupings of subjects, another major research thrust in medical imaging. Finally, besides investigating static functional patterns, extracting dynamic features to study brain dynamics is becoming important due to the evidence that brain functional patterns exhibit changes during the scanning period of fMRI. Both BOLD activity and functional network connectivity (FNC) are shown to be related to mental and cognitive processes. However most previous dynamic studies only conduct a dynamic FNC (dFNC) analysis and few studies have evaluated the inter-relationships of these two domains of function. It is desirable to incorporate dynamic BOLD activity (dBA)

to gain insight into the activity-connectivity co-evolution in the study of brain dynamics.

In this dissertation, we address these challenges by working within the source separation umbrella for fMRI analysis. We first demonstrate that jointly incorporating multiple types of diversity is more desirable by proposing the use of objective global metrics to assess the performance of different data-driven algorithms—independent component analysis (ICA), dictionary learning, and sparse version of ICA—that each make use of different types of diversity. Independent vector analysis (IVA) extends ICA to multiple datasets by additionally making use of dependence across datasets, and hence can preserve the correlation structure across datasets but suffers from the dimensionality issue. We develop a new method, IVA for common subspace analysis (IVA-CS) for subspace analysis of multi-subject fMRI by leveraging the strengths of IVA and addressing the dimensionality issue. We show that IVA-CS is able to extract meaningful common and distinct subspaces as well as group-specific neuroimaging features that allow for the identification of significant subgroups of SZ subjects. In order to enable a study of brain dynamics in terms of both dBA and dFNC, we propose a novel use of adaptively constrained IVA (acIVA) to capture activity variabilities and efficiently quantify the spatial property of dBA (sdBA). We first address the challenge in dFNC analysis by proposing a goal-driven scheme to successfully select an optimal value for the number of dFNC states. The efficient quantification of sdBA enables a careful investigation of the association between temporal property of dBA (tdBA) and sdBA, and the activity-connectivity co-evolution of sdBA and dFNC computed using the spatial maps (sdFNC). The application to multi-subject resting-state fMRI data detects significant tdBA-sdBA patterns and activity-connectivity co-evolution patterns. Moreover, we identify significant subgroups of SZs using tdBA-sdBA association and sdBA-sdFNC co-evolution, demonstrating the effectiveness of dynamic features for studying heterogeneity of disorders.

**Data-driven Techniques for the Study of Brain Dynamics
and Identification of Subgroups: Application to
Multi-subject Resting-state fMRI Data**

by
Qunfang Long

Dissertation submitted to the Faculty of the Graduate School
of the University of Maryland in partial fulfillment
of the requirements for the degree of
Doctor of Philosophy
2020

To my wonderful husband Mingze Gao and my loving family

ACKNOWLEDGMENTS

Though it is truly a difficult journey to complete a PhD, I extraordinarily appreciate receiving so many supporting and encouraging words and actions from everyone around me to help and guide me through it. It is hard to express my gratitude fully to them with my limited words but I will try my best.

First, to my advisor, Dr. Tülay Adalı, I must thank her for her enthusiasm and remarkable foresight in this research field that inspire me all the time. Dr. Adalı created a wonderful environment where we do research in a collaborative way and questions and discussions are always encouraged. She is the person who mostly influenced my interest in machine learning for neuroimaging analysis. Her countless valuable advices about technical writing, presentations, and communication skills also helped me a lot.

I would like to express my deep appreciation to Dr. Vince Calhoun for providing extremely prompt guidance and feedback to my research with his professional insight. I would thank Dr. Yuri Levin-Schwartz, Dr. Zois Boukouvalas, and Rami Mowakea for many helpful discussions to start my research work. I must thank Dr. Suchita Bhinge for her great help and close collaboration to help proceed my work. I am very grateful to all current and former members of the MLSP lab: Mohammad Abu Bak Siddique Akhonda, Chunying Jia, Ben Gabrielson, Darren Emge, and Xiaowei Song for their valuable feedback and help.

I would also like to thank the members of my committee: Dr. Linda Chang, Dr. Thomas Ernst, Dr. Seung-Jun Kim, Dr. Vince Calhoun, and Dr. Zois Boukouvalas for taking time to review my work and providing very insightful comments.

I owe my deepest thanks to my husband Mingze Gao and my loving family for their constant support and believe in me. I would like to thank all my friends who kept me

accompanied at those important moments and all those who ever helped me along my life.

It is worth mentioning that this work was supported by grants NSF-CCF 1618551, NSF-NCS 1631838, and NIH R01-MH 118695.

TABLE OF CONTENTS

DEDICATION	ii
ACKNOWLEDGMENTS	iii
LIST OF TABLES	ix
LIST OF FIGURES	x
List of Abbreviations	xx
Chapter 1 INTRODUCTION	1
1.1 Analysis of fMRI data	1
1.1.1 Subspace analysis of multi-subject fMRI data	3
1.1.2 Study of brain dynamics	4
1.1.3 Model-driven and data-driven techniques	7
1.2 Contributions	10
1.3 Overview of dissertation	13
Chapter 2 BACKGROUND	16
2.1 Multi-subject resting-state fMRI data	16
2.2 Data-driven BSS techniques for a single dataset	19

2.2.1	Independence as type of diversity: ICA	19
2.2.2	Sparsity as type of diversity: DL	22
2.2.3	Balancing independence and sparsity: SparseICA	23
2.3	Data-driven BSS techniques for multiple datasets	24
2.3.1	Group ICA	24
2.3.2	IVA	25
2.3.3	MCCA	28
2.4	Summary	29

Chapter 3 THE ROLE OF DIVERSITY IN MULTI-SUBJECT FMRI DATA ANALYSIS 31

3.1	Introduction	31
3.2	Global metrics for performance assessment	34
3.2.1	Frequency analysis	34
3.2.2	Network connection summary	34
3.2.3	Graph-theoretical metrics	36
3.3	Experimental results	37
3.3.1	Implementation	37
3.3.2	Power ratio comparison	45
3.3.3	Network connection summary	46
3.3.4	Graph-theoretical analysis	47
3.3.5	Discussion	50
3.4	Summary	54

Chapter 4 IVA FOR SUBSPACE ANALYSIS OF MULTI-SUBJECT FMRI DATA 55

4.1	Introduction	56
4.2	Strengths and challenges of IVA	58
4.2.1	Identification condition for IVA	58
4.2.2	Dimensionality issue of IVA	64
4.3	IVA for common subspace analysis	67
4.3.1	IVA-CS: Subset analysis	68
4.3.2	IVA-CS: Common subspace identification	70
4.4	Experimental results	71
4.4.1	Common subspace identification using IVA-G-CS	71
4.4.2	Analysis of group-specific SCVs	77
4.4.3	Discussion	81
4.5	Summary	82
Chapter 5	QUANTITATIVE STUDY OF RESTING-STATE DFNC	84
5.1	Introduction	85
5.2	Methods	87
5.2.1	Data formation for dynamic analysis	88
5.2.2	Adaptively constrained IVA	89
5.2.3	Reference signal extraction	91
5.2.4	Graph-theoretical analysis	91
5.2.5	A goal-driven scheme	92
5.3	Application to multi-subject resting-state fMRI data	92
5.3.1	Graph-theoretical analysis based quantitative study of dFNC	95
5.4	Summary	101

Chapter 6	STUDY THE ACTIVITY-CONNECTIVITY CO-EVOLUTION OF DBA AND DFNC	102
6.1	Introduction	102
6.2	Efficient quantification of sdBA	104
6.2.1	Simulation study	105
6.2.2	Application to real fMRI data	108
6.3	Co-evolution of dBA and dFNC	110
6.4	Study of heterogeneity of SZ using dynamic features	112
6.5	Summary	118
Chapter 7	CONCLUSIONS AND FUTURE WORK	119
7.1	Conclusions	119
7.2	Future directions	122
7.2.1	Full automation of IVA-CS	123
7.2.2	Subspace study across multiple groups/tasks/modalities	124
7.2.3	Subspace analysis of task-evoked fMRI data	126
	REFERENCES	128

LIST OF TABLES

3.1	Description of graph-theoretical metrics in both node and graph level. . . .	36
-----	--	----

LIST OF FIGURES

1.1	Dynamic features that quantify the evolution of BOLD activity and functional connectivity are useful for the study of brain dynamics. (a) Both spatial maps and time courses of RSNs change over time, leading to changes in the constructed FNC that measures the association between the BOLD activation patterns of RSNs. (b) Static features measure the average BOLD activity and FNC over time and hence cannot describe the dynamics.	5
2.1	The fMRI machine and the obtained fMRI data.	17
2.2	The linear mixture model used by data-driven BSS techniques for fMRI analysis.	18
2.3	The generative model of IVA	26
3.1	The relative contribution of statistical independence and sparsity (a)–(c) in SparseICA-EBM, the violin plot of the time course power ratio (d) and the spatial maps of motor components estimated by SparseICA-EBM when $\lambda_s = 10^{-5}$ and $\lambda_s = 10^{-4}$ (e). In (a)–(c), the x-axis denotes the number of SparseICA-EBM iterations and y-axis denotes the cost. In (e), Z-maps corresponding to the mean components averaged across all subjects for motor components are shown. The maps are thresholded using a threshold $Z_t = 2$	38

3.2	Comparison of several components from DL using different values of λ . Z-maps corresponding to the mean components averaged across all subjects for DMN, auditory (AUD), motor, sensorimotor (SM) and frontoparietal (F-P) component are shown. The maps are thresholded using a threshold $Z_t = 2$. The peak coordinates in mm are shown to the right. Note that for $\lambda = 10^2$, there are two FP components that are estimated.	42
3.3	The violin plot of the time course power ratio for all 85 mean components of (a) DL using different values of λ and (b) five algorithms. Note that s-EBM refers to SparseICA-EBM.	43
3.4	Comparison of several components from five algorithms. Z-maps corresponding to the mean components averaged across all subjects for the anterior DMN, DMN and frontoparietal (F-P) component are shown. The maps are thresholded using a threshold $Z_t = 2$. The peak coordinates in mm are shown to the right. Note that s-EBM refers to SparseICA-EBM.	46
3.5	Network connection summary of components from EBM. (a) Spatial maps of 50 functional networks. Functional networks are divided into groups based on their anatomical and functional properties. COG: Cognitive control; DM: default mode; AUD: auditory; VIS: visual; CB: cerebellum. (b) The functional connectivity matrix. Connectivity is measured using normalized MI. (c) Network connectivity visualization. The outermost circle demonstrates one slice of the spatial map of individual mean component. The colored circle indicates the index corresponding to each component and different colors refer to different functional network clusters. Curves in the center carry the exact connectivity among these components.	48

3.6	Number of nodes showing significant group difference in each graph as a function of link density for (a) characteristic path length (PL) and (b) betweenness centrality. Note that s-EBM refers to SparseICA-EBM.	49
3.7	Comparison of the normalized STD of (a) clustering coefficient (CC) and (b) small-worldness (SW) in SZs and HCs. Note that s-EBM refers to SparseICA-EBM.	49
4.1	The definition of common subspace and other two sets of SCVs in signal space (a) and the subset analysis and common subspace identification of IVA-CS (b). The number of SCVs in each of the three sets in (a) are denoted by N_C , N_G and N_D separately.	60
4.2	Correlation matrices of true SCVs (a), the estimated ones from IVA-G (b), MCCA-GENVAR (c), MCCA-MAXVAR (d), and MCCA-SSQCOR (e) in simulation.	61
4.3	Boxplots of the correlation values between the estimates and the ground truth for IVA-G in blue and IVA-L-SOS in magenta for the four cases. Statistics are calculated from 100 independent runs with different initialization. The box plot displays the median, the 25th and 75th percentiles of the correlation values with whiskers extending to the 99.3% confidence interval using the default settings.	63
4.4	Plot of joint-ISI as a function of the number of subjects when performing IVA-G on the hybrid data. The mean and standard deviation calculated from the results of 20 runs are shown.	65

4.5	(Part 1) Smoothed distribution of the correlation values of the five subsets of SZ group. The red crosses and the green squares denote the mean and median. Two ratios q and \tilde{q} are plotted in yellow and purple. Two vertical red lines denotes the margins between different groups of SCVs. Blue and magenta horizontal lines denotes 0.6 and 0.2 which are used for a comparison of the three groups of SCVs.	72
4.6	(Part 2) Smoothed distribution of the correlation values of the five subsets of SZ group. The red crosses and the green squares denote the mean and median. Two ratios q and \tilde{q} are plotted in yellow and purple. Two vertical red lines denotes the margins between different groups of SCVs. Blue and magenta horizontal lines denotes 0.6 and 0.2 which are used for a comparison of the three groups of SCVs.	73
4.7	(Part 1) Smoothed distribution of the correlation values of the five subsets of HC group. The red crosses and the green squares denote the mean and median. Two ratios q and \tilde{q} are plotted in yellow and purple. Two vertical red lines denotes the margins between different groups of SCVs. Blue and magenta horizontal lines denotes 0.6 and 0.2 which are used for a comparison of the three groups of SCVs.	74
4.8	(Part 2) Smoothed distribution of the correlation values of the five subsets of HC group. The red crosses and the green squares denote the mean and median. Two ratios q and \tilde{q} are plotted in yellow and purple. Two vertical red lines denotes the margins between different groups of SCVs. Blue and magenta horizontal lines denotes 0.6 and 0.2 which are used for a comparison of the three groups of SCVs.	75

4.9	Spatial maps of the common components in six categories: Motor; COG, cognitive control; DM, default mode; AUD, auditory, VIS, visual; CB, cerebellum. (a)-(d) for SZ group and (e)-(h) for HC group. The number of independent components (ICs) that are composited in each subfigure is listed and different colors refer to the spatial maps of individual components.	76
4.10	The clustering and modularization processes of the correlation matrices of group-specific SCVs and the two clusters that yield clear subgroups of patients (a-c). Subgroup 1, 2, and 3 are labeled by orange, magenta, and red squares separately. The differences of spatial activation patterns across subgroups in Cluster I (d) and Cluster II (e) are represented by the <i>t</i> -statistic from a two sample <i>t</i> -test with FDR (≤ 0.05) control and the associated confidence interval (CI) is reported. The brain regions that show significant subgroup (SG) differences including: posterior cingulate gyrus (PCG), BA31, secondary visual cortex (SVC), anterior cingulate gyrus (ACG), primary somatosensory and motor cortex (SSM), angular gyrus (Ang), inferior frontal gyrus (IFG), and BA30.	78
4.11	The median (connected by solid lines), minimum, and maximum (connected by dash lines) values of each PANSS score of subgroups in Cluster I (a) and Cluster II (c), and the dominant (bright orange, magenta, and cyan) and absent (fade orange, magenta, and cyan) symptoms of each subgroup in Cluster I (b) and Cluster II (d). In (b) and (d), the bold symptoms refer to those that are unique for a subgroup and the translucent symptoms refer to those that are absent from all three subgroups.	80
5.1	Dynamic study using acIVA with windowing strategy	88

5.2	Spatial maps of the eight common components of HC and SZ groups. SP-V-C: super parietal-visual-cerebellum, F-P: frontoparietal, SMA: supplementary motor area.	93
5.3	Ratio of the number of dFNC matrices in each state for SZ and HC groups as the value of N_s changes when using sdFNC (a) and tdFNC (b). The number of states with different ratios between the two groups is summarized in (c). The detailed results of the knee point detection that determines the number of states with different SZ and HC subjects are shown in (d). . .	94
5.4	Summary of the statistical test results of global graph-theoretical metrics for the cases with $N_s = 5, 6, 7, 8,$ and 9 . In each plot, the boxplot on the top summarizes the p -values with FDR control, the barplot gives the number of graphs with different link density that has a p -value survives the FDR correction, and the triangular over a bar means the test results show the graph-theoretical metric has higher value in SZs (red) or HCs (blue). The red dot in the upper right corner indicates the number of SZ and HC subjects are different in a state. Ef-g: global efficiency, Ef-l: local efficiency, PL: path length, CC: clustering coefficient, SW: small-worldness, BCt: betweenness centrality, CCt: closeness centrality, ECt: eigenvector centrality .	96

5.5 Summary of the statistical test results of nodal graph-theoretical metrics for states 5 and 6 when $N_s = 6$. In each plot, the boxplot on the top summarizes the p -values with FDR control, the barplot gives the number of graphs with different link density that has a p -value survives the FDR correction, and the triangular over a bar means the test results show the graph-theoretical metric has higher value in SZs (red) or HCs (blue). Ef-g: global efficiency, Ef-l: local efficiency, PL: path length, CC: clustering coefficient, BCt: betweenness centrality, CCt: closeness centrality, ECt: eigenvector centrality . 98

5.6 Summary of the statistical test results of nodal GT metrics for the complex component (IC5) and the supplementary motor area component (IC7) when $N_s = 6$. In each plot, the boxplot on the top summarizes the p -values with the false discovery rate (FDR) control, the barplot gives the number of graphs with different link density that has a p -value survives the FDR correction, and the triangular over a bar means the test results show the GT metric has higher value in SZs (red) or HCs (blue). Ef-g: global efficiency, Ef-l: local efficiency, PL: path length, CC: clustering coefficient, BCt: betweenness centrality, CCt: closeness centrality, ECt: eigenvector centrality 99

5.7 Summary of the statistical test results of nodal GT metrics for the fronto-parietal component (IC6) and the supplementary motor area component (IC7) when $N_s = 6$. In each plot, the boxplot on the top summarizes the p -values with the false discovery rate (FDR) control, the barplot gives the number of graphs with different link density that has a p -value survives the FDR correction, and the triangular over a bar means the test results show the GT metric has higher value in SZs (red) or HCs (blue). Ef-g: global efficiency, Ef-l: local efficiency, PL: path length, CC: clustering coefficient, BCt: betweenness centrality, CCt: closeness centrality, ECt: eigenvector centrality 100

6.1 Visualization of the correlation matrices and the decomposition results of acIVA in the four cases of simulation. In the ticklabels of x -axis in the boxplots, “H” refers to the results of components that are highly correlated (c_1) with the reference signal, “L” refers to the results of components that are not highly correlated (c_2), and “diff” refers to the cases where we summarize the differences between the tuned values of $\hat{\rho}$ and the ground truth. The boxplot displays the median, the 25th and 75th percentiles of the values with whiskers extending to the 99.3% confidence interval and some outliers in red asterisks beyond whisker. 105

6.2 The tuned values of $\hat{\rho}$ in acIVA and the computed correlation $\tilde{\rho}$ between the estimates and the reference signals as a function of windows for a HC subject and an SZ subject (a). The spatial activation of the DMN component varies across windows in HC subject (b) and SZ subject (c). The values of spatial activation are normalized to be z -scores and thresholded using $z_t = 2$. 109

6.3 Cross-correlation between sdBA ($\tilde{\rho}$) and tdba (fALFF) (a) and activity-connectivity co-evolution computed using sdBA ($\tilde{\rho}$) and sDFNC (b). 111

6.4 Cross-correlation matrices of two types of dBA (a) and activity-connectivity co-evolution matrices computed using dBA and dFNC (b) that are averaged across subjects in SZ and HC groups. The values of t -statistic with an FDR control are shown. 111

6.5 Mean cross-correlation matrices of each subgroup and the statistical test results (with an FDR control) for three scenarios with different values of N_s . The robust clusters of SZ subjects are listed under the correlation matrices using different colors. The colored font in bold refer to clusters that are robustly detected in all three scenarios and the regular colored font refer to clusters that are detected in two scenarios. The font in black refer to subjects that are not belong to any robust clusters. The numbers in brackets denote the number of subjects in each subgroup. 113

6.6 (Part 1) Mean activity-connectivity co-evolution matrices $\bar{\mathbf{E}}_{SGi}, i = 1, 2, 3, 4, 5, 6$, of each subgroup and the statistical test results (with an false discovery rate control at $p < 0.05$) for three scenarios with $N_s = 4, 5$, and, 6 . The robust clusters of SZ subjects that are denoted using numbers $k = 1, \dots, 88$ are listed on the top of the figure using different colors. The colored font in bold refer to clusters that are robustly detected in all three scenarios and the regular colored font refer to clusters that are detected in two scenarios. The font in black refer to subjects that are not belong to any robust clusters. The numbers in brackets denote the number of subjects in each subgroup. (cont.) 114

6.7	(Part 2) Mean activity-connectivity co-evolution matrices $\bar{\mathbf{E}}_{SGi}, i = 1, 2, 3, 4, 5, 6,$ of each subgroup and the statistical test results (with an false discovery rate control at $p < 0.05$) for three scenarios with $N_s = 4, 5,$ and, $6.$ The robust clusters of SZ subjects that are denoted using numbers $k = 1, \dots, 88$ are listed on the top of the figure using different colors. The colored font in bold refer to clusters that are robustly detected in all three scenarios and the regular colored font refer to clusters that are detected in two scenarios. The font in black refer to subjects that are not belong to any robust clusters. The numbers in brackets denote the number of subjects in each subgroup.	115
6.8	Correlation between the positive, negative, and general PANSS scores for each subgroup when $N_s = 6$ for the case using $\mathbf{C}^{[k]}$ (a)-(c) and $\mathbf{E}_n^{[k]}$ (d)-(f). The large chart plots the data of six subgroups together for a easier visual comparison and the small charts on its right plot the data of individual subgroups with the correlation value and its associated significance level listed.	117
7.1	Improved method for the identification of subgroups of subjects.	124
7.2	IVA for joint study of multi-group/multi-task/multimodal data. Note that M denotes the number of groups/tasks/modalities, K denotes the number of datasets in each group/task/modality, and V denotes the sample number.	125
7.3	Transformed IVA model for task subspaces extraction using task-evoked fMRI data.	127

LIST OF ABBREVIATIONS

ACG	anterior cingulate gyrus
acIVA	adaptively constrained IVA
Ang	angular gyrus
ANOVA	univariate analysis of variance
AUD	auditory
BA	Brodmann area
BCt	betweenness centrality
BOLD	blood-oxygen-level-dependent
BSS	blind source separation
CB	cerebellum
CC	clustering coefficient
CCt	closeness centrality
CI	confidence interval
COBRE	Center of Biomedical Research Excellence
COG	cognitive control
dBA	dynamic BOLD activity
dFNC	dynamic FNC
DL	dictionary learning
DM(N)	default mode (network)
EBM	entropy bound minimization
ECt	eigenvector centrality
Ef-g	global efficiency
Ef-l	local efficiency

ERBM	entropy rate bound minimization
ER-FM	entropy rate-based finite memory
fALFF	fractional amplitude of low-frequency fluctuation
FDR	false discovery rate
fMRI	functional magnetic resonance imaging
FNC	functional network connectivity
F-P	frontoparietal
GGD	generalized Gaussian distribution
GICA	direct group ICA back-reconstruction
HC	healthy control
HOS	higher than second-order statistics
IFG	inferior frontal gyrus
ICA	independent component analysis
IC	independent component
Infomax	information maximization
IPC	inferior parietal cortex
ISI	intersymbol-interference
IVA	independent vector analysis
IVA-CS	IVA for common subspace analysis
IVA-G	IVA with multivariate Gaussian
IVA-G-CS	IVA-CS using IVA-G
IVA-MGGD	IVA with multivariate generalized Gaussian distribution
IVA-L	IVA with multivariate Laplacian
IVA-L-SOS	IVA-L with SOS
MANOVA	multivariate analysis of variance

MCCA	multiset canonical correlation analysis
MCCA-GENVAR	MCCA with GENVAR cost function
MCCA-MAXVAR	MCCA with MAXVAR cost function
MCCA-SSQCOR	MCCA with SSQCOR cost function
MGGD	multivariate generalized Gaussian distribution
MI	mutual information
ML	maximum likelihood
MNI	Montreal Neurologic Institute
PANSS	positive and negative syndrome scale
PCA	principal component analysis
PCC	posterior cingulate cortex
PCG	posterior cingulate gyrus
PDF	probability density function
PL	path length
RSN	resting-state network
SCV	source component vector
sdBA	spatial property of dBA
sdFNC	dFNC computed using the spatial maps
ShSSDL	shared and subject-specific DL
SM	sensorimotor
SMA	supplementary motor area
SOS	second-order statistics
SparseICA-EBM/s-EBM	sparse ICA by entropy bound minimization
SP-V-C	super parietal-visual-cerebellum
SSM	somatosensory and motor cortex

SVC	secondary visual cortex
SW	small-worldness
SZ	schizophrenia
tdBA	temporal property of dBA
tdFNC	dFNC computed using the time courses
vACC	ventral anterior cingulate cortex
VIS	visual

Chapter 1

INTRODUCTION

1.1 Analysis of fMRI data

Functional magnetic resonance imaging (fMRI) is a neuroimaging modality that detects changes in the blood-oxygen-level-dependent (BOLD) response that are caused by the neuronal activation in the brain, opening a new window for the interpretation of human brain function. The fMRI data observes BOLD activity in brain spatially within a volume of high resolution (typically in millimeters) and temporally at different time instants of low resolution (typically every one or two seconds), yielding a four-dimensional dataset for each subject. In most fMRI data analysis, each fMRI volume at a specific time instant is flattened to a vector to transform the original four-dimensional data into a two-dimensional data matrix with time points vertically presented and the voxels horizontally summarized. From the observed fMRI data we can extract BOLD activation patterns of functional regions or coherent networks in spatial and temporal domains. This therefore enables an investigation of the BOLD activity and the brain connectivity in order to study how the normal brain functions and how it is affected by drug abuse and neurological disorders, and how the brain attempts to recover after proper treatment. For example, the abuse of ecstasy, amphetamine, cannabis, and nicotine is found to be associated with abnormal functional alternations in human brain [104, 185]. In the study of neurological disorders, a common hypothesis that the brain function is less efficient for subjects with a certain type of disorder

der compared with the healthy controls (HCs). There is rich work that successfully identify distinct biomedical patterns in a variety of disorders such as schizophrenia (SZ), atrophy, degenerative dementias, Alzheimer's disease, and post-traumatic stress disorder through the analysis of fMRI data, enabling a better understanding of these disorders hence potentially providing useful clinical guidance [30,45,82,140,160,169,192]. Clinical factors such as emotional measures, behavioral performance, and positive and negative syndrome scale (PANSS) that is special for SZ are shown to correlate with functional biomedical patterns in neurological disorders [20,109,179]. Also, the effect of drug use and the effectiveness of treatment in disorders, such as the use of cannabis [134] and antipsychotic medications [42] in SZ, have been studied using fMRI data.

However, the extraction of interpretable functional BOLD activity patterns from fMRI data is complicated by many factors, such as the low signal to noise ratio, random noise, constant biological processes (breathing and heartbeat), subject motion, and inter-subject anatomical variabilities. Many preprocessing techniques, such as filtering for noise and registration for subject motion, are adopted to reduce the effect of these factors but it is very hard to eliminate it. Another big challenge in fMRI analysis is the lack of prior knowledge of the data especially the resting-state fMRI data. The analysis of resting-state fMRI data is emphasized because it captures the intrinsic neural activities when the brain is not constrained by any external input or task stimuli, and the obtaining of resting-state fMRI is easier and less expensive without training the participants. Therefore, methods that effectively analyze fMRI data in a data-driven manner and are robust to the effect of these complicated factors are preferable. Computational complexity is also crucial in multi-subject fMRI data analysis due to the increasing number of large fMRI datasets that include hundreds or even thousand of subjects. It is important to investigate the offset between a joint analysis of a large number of datasets and an effective preservation of dataset-specific

variabilities.

All these challenges should be taken into account when addressing problems of interest in multi-subject resting-state fMRI data analysis. Two critical ones that have received much attention lately are subspace analysis and the study of brain dynamics. Subspace analysis of multi-subject fMRI data started gaining attention since it is able to extract group-specific BOLD activation patterns that help identify subgroups of subjects, allowing for a more comprehensive study of mental disorders such as SZ that has been clinically recognized to possess the property of heterogeneity. The study of brain dynamics on the other hand aims at extracting and modeling the dynamics of functional biomedical patterns in human brain. It has been shown that the brain with different mental disorders also demonstrates significant differences in dynamic patterns compared with that of the normal brain [62, 81, 162]. In this work, we develop effective methods to resolve these two important problems in fMRI analysis by addressing the challenges we introduced above as well as other specific challenges in the two problems we present as follows.

1.1.1 Subspace analysis of multi-subject fMRI data

Identification of common and distinct subspaces from multiple datasets transforms the high dimensional datasets into lower dimensional joint and disjoint subspaces, and allows for a more detailed analysis of the group-specific as well as distinct information. Along with identifying a common subspace comprised of components correlated across all subjects, the extraction of common components across a subgroup of subjects is also of interest. Clinical heterogeneity of patients with mental disorders, especially in SZ has been recognized [69, 101, 102], and there has been significant interest in studying their subtypes [82, 89, 150]. The study of subtypes can be made possible by identifying subgroups of patients that share specific common information and can help better understand the uncertainty in the need of precision medicine [167] during clinical diagnosis and treat-

ment. Subtypes of SZ have been well studied using genetic information [89, 150] but not yet using other neuroimaging modalities such as fMRI data, which has been successfully used in the study of SZ [45, 82, 140]. The common subspace analysis motivates us to find a way to identify subgroups of patients with subtypes of SZ by summarizing their shared information.

Given the importance of subspace analysis in medical image analysis, a number of recent studies had a focus on this aspect, in particular for fusion of different modalities such as fMRI, structural MRI and electroencephalograph, or of fMRI data from different tasks [5, 65, 114, 126, 135, 161, 176, 184]. However these cases have only been demonstrated for joint decomposition of a small number of datasets. As we have discussed, distinct and common subspace analysis also promises to be attractive for multi-subject analyses. The models used for identification of common and distinct subspaces in fusion study have not been well-studied in the context of the joint analysis of more than a couple of datasets. Multi-subject data analysis involves joint analysis of at least tens, or more typically hundreds of subjects. This motivates the development of an effective method that allows for a subspace analysis of multi-subject imaging data by successfully preserving the correlation structure across datasets.

1.1.2 Study of brain dynamics

There is evidence showing that the intrinsic functional patterns in human brain change over time and the time-varying—dynamic—patterns are captured and studied using resting-state fMRI data [58, 90, 94, 95]. A decomposition of resting-state fMRI data extracts resting-state networks (RSN) that consists of cortical and subcortical areas with synchronized BOLD activities. BOLD activation pattern of a RSN varies in both spatial and temporal domains over time, which are referred to as spatial maps and time courses separately, leading to the changes in the constructed functional network connectivity (FNC) that mea-

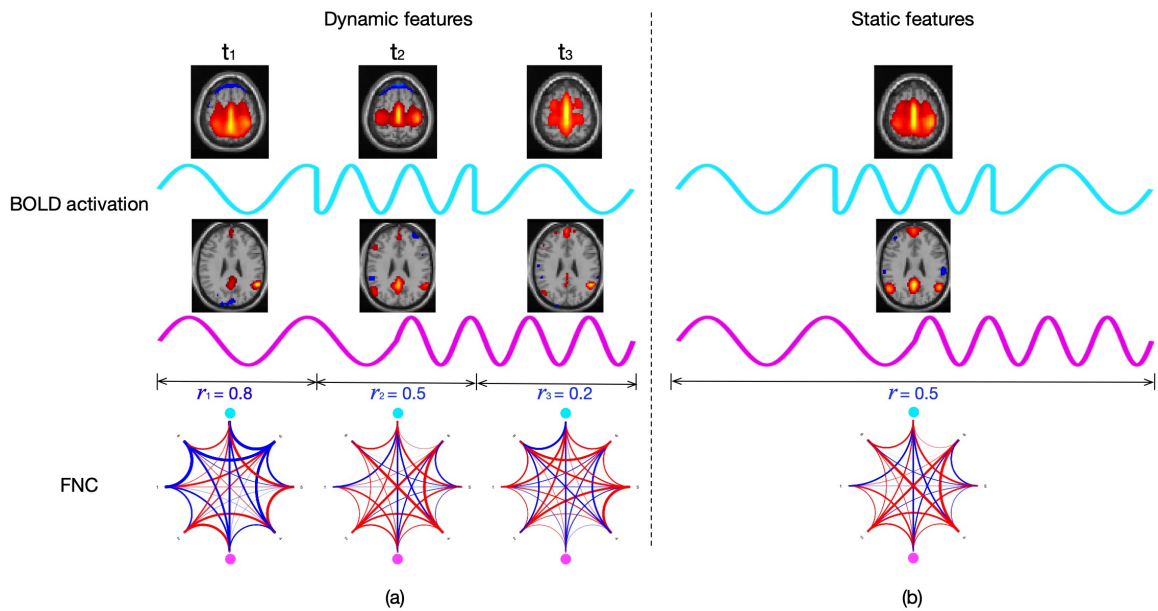


FIG. 1.1. Dynamic features that quantify the evolution of BOLD activity and functional connectivity are useful for the study of brain dynamics. (a) Both spatial maps and time courses of RSNs change over time, leading to changes in the constructed FNC that measures the association between the BOLD activation patterns of RSNs. (b) Static features measure the average BOLD activity and FNC over time and hence cannot describe the dynamics.

sures the association between the BOLD activation patterns, as shown in Fig. 1.1. Static features quantify the average BOLD activity and FNC across time and hence are not able to precisely describe the functional evolution in brain, limiting the interpretation of brain function. Therefore, conducting a study of brain dynamics through the use of dynamic features is important in order to gain a better understanding of the brain function.

Based on the time-varying BOLD activation patterns of RSNs, most dynamic studies obtain a FNC matrix as a function of time [10, 30, 51, 62, 79, 103, 155, 189]. A dynamic FNC (dFNC) analysis allows a systematical study of evolving functional patterns by jointly taking multiple brain networks into consideration. Identifying discrete transient states that are characterized by FNC patterns is a common strategy in order to study the dynamic evolution of brain function [141, 196]. The determination of the number of states is essential

while there is no effective method for its selection. People either select the value that yields the lowest error or cost regarding the clustering methods they use to identify the states, or use multiple values and conduct a comparison.

There is rich work showing that both BOLD activity and functional connectivity are related to mental and cognitive processes, see e.g., [37,93,145,146]. Differences in BOLD activity and functional connectivity has been separately reported in multiple mental disorders especially in SZ, such as the reduced amplitude of low-frequency fluctuation (ALFF) in cuneus [91,180], reduced BOLD activation in anterior cingulate gyrus [19,165], dysconnectivity in default mode network [183,198], and dysconnectivity between thalamus and sensory regions [49,117,143,149,198]. However, the association between dynamic BOLD activity (dBA) and dFNC is not well studied and it is desirable to incorporate dBA to gain insight into the activity-connectivity co-evolution by identifying highly correlated patterns between dBA and dFNC.

In [80], the authors investigate the associations between dBA and dFNC in temporal domain, *i.e.*, they measure dBA and dFNC using the temporal variabilities of functional networks and observe that dBA and dFNC are significantly correlated in time in some cases and not in others and SZ patients show lower or nonexistent associations between dBA and dFNC compared with HCs. However, like in [80], most previous studies conduct a dFNC analysis using the time courses of BOLD activity by assuming the spatial domain is static [10,51,103,189]. As we illustrate in Fig. 1.1, the BOLD activation of RSNs varies in both the spatial and temporal domains. Spatial variation of BOLD activity is observed as changes in the volume of a functional network or variations in the activated regions within a functional network and has started to attract attention, since they enrich the dynamic study of brain function [98–100]. Previous studies have shown that simultaneously considering temporal and spatial changes yields more distinguishable RSNs between subject groups

[100, 105, 116]. Studies that compute dFNC using the spatial maps of brain networks also have emphasized the importance of the assumption of spatial variability in a dynamic study, by detecting significant differences between the patients with mental disorder such as between those with SZ and the HCs [25, 27, 141]. However, the spatial activation patterns of dBA themselves are not well explored primarily due to the lack of effective quantification strategies of the spatial property of dBA (sdBA). An efficient quantification of sdBA does not only enable the investigation of the spatial activation patterns of dBA but also leads to a study of activity-connectivity co-evolution using sdBA and dFNC that is computed using the spatial maps (sdFNC). More importantly, due to the dynamic nature of human brain, it is desirable to investigate the effectiveness of dynamics neuroimaging features for identifying subgroups of subjects that enable the study of the heterogeneity of mental disorders such as SZ.

1.1.3 Model-driven and data-driven techniques

Methods to analyze fMRI data can be studied under two broad categories as model driven and data driven. Model-driven methods are typically based on priori models that specify the structure of temporal variation or spatial activation patterns of functional networks or brain regions, and have been the traditional approach for analyzing fMRI data. They assume that certain types of prior information about the data are known. Seed-based approach is a type of model-driven method that makes use of the spatial maps of pre-defined templates of brain regions of interest and is known as a univariate method that treats each voxel independently and obtains the corresponding temporal variation patterns by averaging the time series of the voxels in each region [59, 85, 127]. However, the use of pre-defined templates assumes that all the selected regions have a similar activation pattern and leads to the analysis results highly dependent on the choice of regions of interest. Additionally, time series usually involve a significant level of noise. One potential solution is

denoising, yet it is difficult to remove all kinds of noise because of the unknown nature of noise. Another model-driven method is general linear model that specifies a user-defined matrix of time courses hence are robust to the effect of noise. However, the strong assumption on the time courses limits the application of general linear model to task-evoked fMRI data where the task stimuli are known and can be used to define the matrix [43, 75, 77, 106]. With the fixed matrix of time courses, the general linear model estimates the spatial maps of functional networks using the regression approach.

Data-driven techniques have been growing in importance for analysis of both resting-state and task-evoked fMRI data since the underlying assumptions are minimized [127, 133, 183] which makes data-driven methods more flexible, and hence more desirable especially for the study of multi-subject resting-state fMRI data as there is no a priori information in this case. Moreover, data-driven methods can be built on using different forms of diversity—statistical properties of the data—hence maximally taking the information into account through a multivariate model in order to study the spontaneous BOLD fluctuations. When a group of neurons in different functional networks are activated at a time instant, their BOLD response is added up linearly and can be modeled using a linear mixture model, forming a typical blind source separation (BSS) problem. The latent sources—functional networks—can be recovered through a matrix factorization of the observed fMRI data, in general, using a generative model that yields a mixing matrix and a source component matrix. The time courses of the functional networks are conveyed in the mixing matrix and the spatial maps are expressed in the source component matrix. The assumptions in data-driven BSS methods are, in part, based on different forms of diversity of either the observations or the underlying sources, such as independence and sparsity, resulting in the development of different data-driven algorithms.

Independent component analysis (ICA) has been a popular data-driven BSS technique

that decomposes the observed data by maximizing a measure of (statistical) independence among the underlying sources [50, 127, 183]. This popularity has, in part, led to the development of different ICA algorithms that can be derived from the maximum likelihood (ML) principle, each designed to achieve the independent component decomposition through exploiting different forms of diversity of the signals, such as higher than second-order statistics (HOS), noncircularity, and sample dependence [4, 48, 66, 96]. Dictionary learning (DL) is another data-driven BSS technique that makes use of sparsity as the starting point for the decomposition and has been shown to be useful for the analysis of fMRI data as well [3, 121, 142, 186]. Recent work [35, 36] introduces a unified mathematical framework that enables a dynamic exploitation of both independence and sparsity, which we refer to as the SparseICA framework. Source sparsity is incorporated through the use of the ICA cost function, penalized by an ℓ^1 regularization term. Although independence and sparsity have demonstrated their utility for the analysis of fMRI data, there is no study that explores the role of each type of diversity in terms of global objective metrics for real fMRI datasets.

Both ICA and DL are originally developed for the decomposition of a single dataset. However, the analysis of fMRI data typically involves multiple datasets that are collected from different subjects. Group ICA [48] and independent vector analysis (IVA) [4] are two algorithms that extend ICA to multiple datasets. Group ICA concatenates the datasets to form a single one and assumes a common signal space across datasets hence bounding the solution space. IVA is a more flexible method that jointly decomposes multiple datasets by making effective use of the dependence across datasets through the definition of a source component vector (SCV) [4, 111, 112]. DL can also be applied to multiple datasets by concatenating the datasets in the same way as group ICA does. IVA has been successfully used for the analysis of multi-subject fMRI data [6, 70, 120] and has been shown to be more effective in capturing dataset variabilities compared with the group ICA

approach [119, 148]. Through the selection of an effective density model for the SCV, IVA can model and estimate the statistical dependence across datasets. Additionally, the strong identification condition of IVA—*i.e.*, the ability to uniquely identify the underlying latent variables—enables the preservation of subspace structure even using only second-order statistics (SOS). However, multiset canonical correlation analysis (MCCA), another widely used data-driven algorithm for multiple datasets, has a limited identification condition hence is good for investigating the association to some extent while not the variabilities across datasets.

1.2 Contributions

As motivated above, providing insight into the comparative advantage of emphasizing one form of diversity over another in the decomposition helps guiding the selection of data-driven BSS techniques for the analysis of multi-subject fMRI data. In the application to fMRI data that is collected from different groups such the SZ group and a HC group, enabling a subspace analysis helps study group-specific RSNs and more importantly identify subgroups of SZ subjects that facilitate a study of the heterogeneity of SZ. Furthermore, it is desirable to study the dynamics of brain using spatial variabilities and investigate the activity-connectivity co-evolution using dBA and dFNC to better interpret the functional organization in brain. Due to the nature of a dynamic change in human brain, it is also of interest to study the heterogeneity of mental diseases such as SZ using dynamic features. In this work, we propose methods to address these challenges. The main contributions are summarized as follows.

i. Study the role of diversity in data-driven algorithms

Algorithmic comparison is difficult as decompositions can be quite different depending on the modeling assumptions of a particular algorithm, thus matching of all the estimated com-

ponents one-to-one is usually not possible. In addition, each method is based on a different cost function. In order to enable a comparison among different data-driven algorithms, we propose to use the global metrics that are objective. We

- Conduct a comparative study to provide insight into the role of different forms of diversity on a decomposition of multi-subject fMRI data. For this task, we choose Infomax, entropy bound minimization (EBM), entropy rate bound minimization (ERBM), DL and SparseICA by EBM(SparseICA-EBM) for the comparison as they are good representations of algorithms that use different types of diversity;
- Propose to use objective global measures, *e.g.*, time course frequency power ratio, network connection summary and graph-theoretical metrics, for performance assessment;
- Provide a general guide to the practitioners about the selection of the appropriate algorithm for a specific situation.

ii. IVA for common subspace analysis

Though ICA and DL have been extended to the analysis of multiple datasets by assuming a common signal space in either the spatial domain or the temporal domain, the group ICA and DL do not make effective use of the dependence across datasets. IVA extends ICA to the analysis of multiple datasets to effectively make use of the dependence across datasets by the definition of SCV, making it an attractive choice for subspace analysis. We

- Study the strengths and challenges of applying IVA to multi-subject fMRI data;
- Demonstrate that IVA can successfully preserve the correlation structure across datasets compared with MCCA using a simulation study;
- Propose and implement a new method IVA for common subspace analysis (IVA-CS) by leveraging the strengths of IVA and addressing the dimensionality issue of IVA;

- Apply IVA-CS to multi-subject fMRI and extract interpretable group-specific RSNs for SZ and HC groups;
- Identify subgroups of SZ subjects that demonstrate significant differences in terms of their imaging data analysis results and their clinical symptoms.

iii. Quantitative study of dFNC using graph-theoretical analysis

A common way of using dFNC for the dynamic study is to identify transient states with the dFNC information as features. It is challenging to determine the optimal number of states.

We

- Propose the use of a recent algorithm adaptively constrained IVA (acIVA) to capture BOLD variability in both temporal and spatial domain;
- Emphasize the importance of making use of spatial variabilities by comparing two forms of dFNC that are computed using time courses (tdFNC) and spatial maps (sdFNC) separately in terms of their potential to extract distinguishable features between groups;
- Propose the use of a goal-driven scheme for the determination of the number of transient states in a more interpretable way in dynamic study;
- Demonstrate the effectiveness of the goal-driven scheme by conducting a dynamic study of a multi-subject fMRI data and quantitatively studying the dFNC using graph-theoretical analysis.

IV. Activity-connectivity co-evolution

Study of the activity-connectivity co-evolution using dBA and dFNC is motivated by the fact that both BOLD activity and network connectivity are related to mental and cognitive processes in human brain. A key task is to find metrics to quantify dBA in either temporal

or spatial domain. Moreover, it will be interesting if we enable the study of heterogeneity of mental diseases such as SZ using dynamic features. Therefore, we

- Propose a novel use of acIVA to efficiently quantify the spatial property of dBA (sdBA) as part of the algorithm and demonstrate its desirable performance through a simulation study;
- Study the cross-correlation between temporal property of dBA (tdBA) and sdBA;
- Investigate the activity-connectivity co-evolution using sdBA and sdFNC;
- Identify subgroups of SZ subjects in order to study the heterogeneity of SZ using dynamic features and investigate clinical differences across the subgroups.

1.3 Overview of dissertation

This dissertation is organized as follows.

In Chapter 2, we provide an introduction to multi-subject fMRI data and a number of data-driven BSS techniques we will be discussing throughout this work. We begin with a brief introduction of the popularity of studying human brain through the analysis of multi-subject fMRI data, and the dataset we use in this work. Then we present three categories of algorithms—ICA, DL, and SparseICA—that make use of different forms of diversity of the data to enable the decomposition of a single dataset. After that we introduce the algorithms for the decomposition of multiple datasets, including group ICA, IVA and MCCA.

In Chapter 3, we present our first contribution of providing insight into the comparative advantage of emphasizing one form of diversity over another when applying the data-driven algorithms to the decomposition of multi-subject fMRI data. We clarify the challenges of making such a performance comparison across data-driven algorithms and propose the use of global metrics in performance assessment. We demonstrate that global

metrics help with the comparative study in the application to multi-subject fMRI data analysis.

In Chapter 4, we introduce the proposed IVA-CS algorithm and its application to the subspace analysis of multi-subject fMRI data. We study the strengths and challenges of IVA and demonstrate its desirable performance in preserving the correlation structure across datasets, proving a good starting point for subspace analysis. Then the two stages of IVA-CS, subset analysis and common subspace identification, are presented in detail. We summarize the results of applying IVA-CS to real fMRI data and highlight its effectiveness in studying of the heterogeneity of SZ.

Chapter 5 presents a quantitative study of dFNC using graph-theoretical analysis in dynamic study. We show that the recently proposed method acIVA effectively captures dBA in both temporal and spatial domains. We investigate the potential of a separate use of tdFNC and sdFNC to extract distinguishable dynamic features to emphasize the importance of using the rich samples in spatial domain for a reliable computation of dFNC. We propose the use of a goal-driven scheme for the determination of the number of transient states and demonstrate the effectiveness of the goal-driven scheme by using a comprehensive study of graph-theoretical metrics when applied to multi-subject fMRI data.

In Chapter 6, we propose a novel use of acIVA to efficiently quantify sdBA and study the cross-correlation between tdBA and sdBA as well as the activity-connectivity co-evolution using sdBA and sdFNC. We first use a simulation study to demonstrate that acIVA accurately captures the spatial variabilities by making use of reference signals. When applied to real fMRI data, we show that the tdBA-sdBA cross-correlation and the activity-connectivity co-evolution features are useful in identifying subgroups of SZ subjects, enabling a study of heterogeneity of SZ.

Finally, we summarize all the contributions made in this work and suggest possible

directions for future work in Chapter 7.

Chapter 2

BACKGROUND

Data-driven algorithms that are designed for a single dataset such as ICA, DL, and the recently proposed method SparseICA either make use of one of the two forms of diversity—independence and sparsity—of the latent sources or jointly take both into consideration. In addition, in most real world applications, there are multiple datasets to be jointly analyzed such as the fMRI data that is collected from multiple subjects. Group ICA and IVA are two algorithms that extend ICA to multiple datasets. DL can also be applied to multiple datasets by concatenating them like what group ICA does. Another data-driven algorithm that is proven powerful in the joint analysis of multiple datasets is MCCA. In this Chapter, we introduce the multi-subject resting-state fMRI data and the commonly used data-driven algorithms for fMRI analysis.

2.1 Multi-subject resting-state fMRI data

The resting-state fMRI data captures the variations of BOLD response that result from the changes in the magnetic properties of the blood during a neuronal activation when the brain is not constrained by any external input or task stimuli. The onset of neuronal activation causes a large demand of glucose that is transported by blood hence more oxygenated blood flows in the area of neuronal activation. Aggregation of oxygenated blood leads to a net decrease in deoxygenated blood. This makes it possible to capture the small changes in

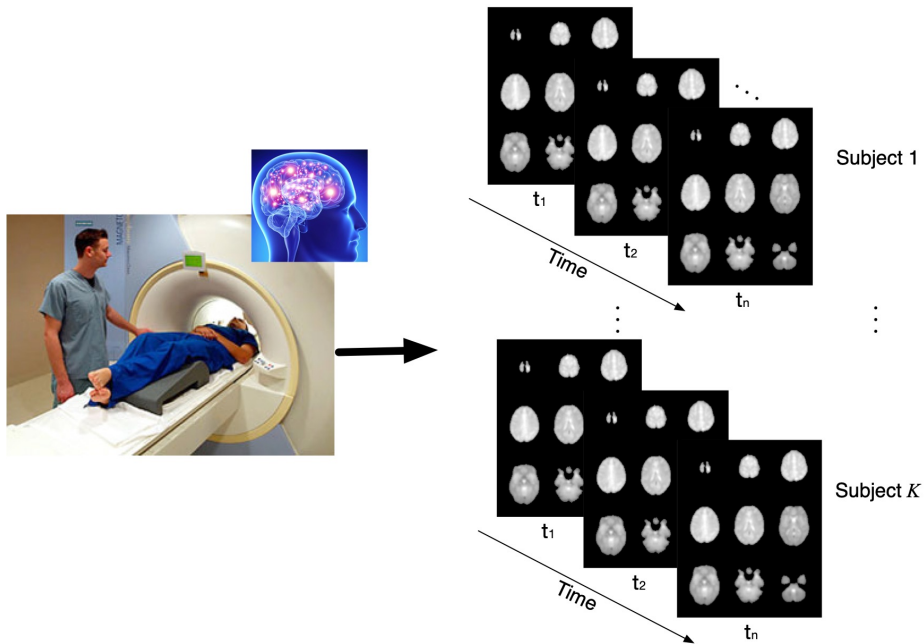


FIG. 2.1. The fMRI machine and the obtained fMRI data.

magnetic sensitivity that reflect the neural activity using fMRI machine since the magnetic properties are slightly different between oxygenated and deoxygenated blood. The machine scans the whole brain at a series of time instants during a certain period, yielding a sequence of volume data—a four-dimensional data—for each subject, as shown in Fig. 2.1. Each entry—voxel—of a volume quantifies the BOLD activity at a specific location hence providing a high quality visualization of the activation patterns of brain. When a group of neurons in different functional networks are activated at a time instant, their BOLD response is added up linearly and can be modeled using a linear mixture model, as shown in Fig. 2.2. The observed fMRI data, the latent source components, and the mixing matrix of time courses are denoted using \mathbf{X} , \mathbf{S} , and \mathbf{A} , respectively. Therefore, matrix factorization techniques such as data-driven BSS methods are exploited to effectively decompose the observed fMRI data and recover the latent sources.

A joint analysis of fMRI data that is collected from multiple subjects, especially those of different groups such as a group of subjects with SZ and a group of HC, makes use

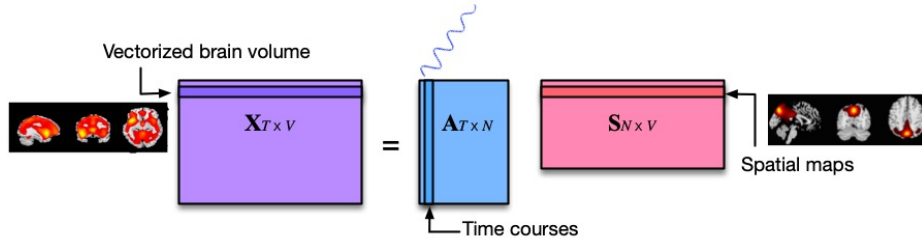


FIG. 2.2. The linear mixture model used by data-driven BSS techniques for fMRI analysis.

of the rich information across datasets. The comparative study of brain function between groups leads to a better understanding of the mental disease by identifying unique biomedical patterns for the patient group. Generally, brain function is relatively more efficiently organized across healthy subjects than subjects with a certain type of mental disorder [28]. It is desirable to study the intrinsic functional patterns of mental disorders when the brain is at a resting state without being constrained by any task stimulus which may force it to act as normal.

In this work, we demonstrate the effectiveness of our proposed methods using a multi-subject resting-state fMRI data from the Center of Biomedical Research Excellence (COBRE), which is available on the collaborative informatics and neuroimaging suite data exchange repository (<https://coins.trendscenter.org/>) [7, 57, 166]. The data includes 88 SZs (average age: 37 ± 14) and 91 HCs (average age: 38 ± 12). For this study, the participants were asked to keep their eyes open during the entire scanning period. All images were collected on a single 3-Tesla Siemens Trio scanner with a 12-channel radio frequency coil using the following parameters: TE = 29 ms, TR = 2 s, flip angle = 75° , slice thickness = 3.5 mm, slice gap = 1.05 mm, voxel size $3.75 \times 3.75 \times 4.55 \text{ mm}^3$. Participants were instructed to keep their eyes open during the scan and stare passively at a central fixation cross. Each resting state scan consists of 150 volumes. To eliminate the T1-related signal fluctuations (T1 effect) [171], the first 6 volumes are removed in this study, thus 144

volumes remain for each subject. The fMRI data are realigned with INRIalign algorithm [73], slice-timing correction is applied using the middle slice as the reference frame in the functional data pipeline and spatially normalized to the standard Montreal Neurologic Institute (MNI) space [76] and resampled to $3 \times 3 \times 3 \text{ mm}^3$, resulting in $53 \times 63 \times 46$ voxels. Afterwards, the fMRI data are smoothed using a Gaussian kernel with a full-width at half-maximum of 5 mm.

2.2 Data-driven BSS techniques for a single dataset

There are two major forms of diversity—independence and sparsity—that have been shown useful in fMRI data decomposition using a data-driven BSS method. ICA is a typical data-driven BSS method that estimates the latent source components by assuming that the latent sources are statistically independent to each other. DL is another data-driven BSS method that extracts the latent sources by making use of the sparsity property of the sources. While initially sparsity has been presented as a competitor for ICA in fMRI analysis [63], the claims in this article regarding the roles of sparsity and independence are later clarified [53], and both sparsity and independence have now been recognized as meaningful starting points for use in fMRI analysis. The work in [35, 36] introduces a unified mathematical framework that enables dynamic exploitation of both independence and sparsity, which we refer to as the SparseICA framework. We introduce the three methods in detail in this section.

2.2.1 Independence as type of diversity: ICA

ICA is able to extract latent sources from the observed data, through the assumption of statistical independence and a linear mixing model [4]. Note that the latent sources are assumed to have zero mean and unit variance and all the estimated source components are normalized to have zero mean and unit variance before any post analyses throughout the

work. Suppose the observed fMRI data of a subject is $\tilde{\mathbf{X}} \in \mathbb{R}^{T \times V}$ with T and V denoting the number of time points and voxels separately. To reduce the contamination from noise, principal component analysis (PCA), using an order N suggested by the entropy rate based order selection technique described in [78], is employed to reduce the dimension of an fMRI dataset, *i.e.*, to estimate the signal subspace. The order estimation method proposed in [78] takes sample dependence into consideration without downsampling, which leads to improved estimation of the signal subspace. The dimension of $\tilde{\mathbf{X}}$ is reduced from T to N , computed as $\mathbf{X} = (\mathbf{F})^\dagger \tilde{\mathbf{X}}$, where † represents the pseudoinverse and $(\mathbf{F})^\dagger \in \mathbb{R}^{N \times T}$ is the reduction matrix, whose columns are the eigenvectors of $\tilde{\mathbf{X}}(\tilde{\mathbf{X}})^\top$ and the reduced data is $\mathbf{X} \in \mathbb{R}^{N \times V}$. The reduced data matrix, \mathbf{X} , consists of the first N principal components of $\tilde{\mathbf{X}}$ that represent the informative signals for the subject. The source components $\mathbf{S} \in \mathbb{R}^{N \times V}$ are then estimated by performing ICA on \mathbf{X}

$$\mathbf{X} = \mathbf{A}\mathbf{S}, \quad (2.1)$$

where $\mathbf{A} \in \mathbb{R}^{N \times N}$ is the mixing matrix. ICA seeks to find a demixing matrix, \mathbf{W} , such that the estimated sources are obtained as $\hat{\mathbf{S}} = \mathbf{W}\mathbf{X}$.

ICA algorithm choice The popularity of ICA for BSS problems such as fMRI data analysis has, in part, led to the development of different ICA algorithms that can be derived from the ML principle, each designed to achieve the independent component decomposition through exploiting different forms of diversity, such as HOS, noncircularity, and sample dependence [4,48,66,96]. For example, the Infomax algorithm, which was the first ICA algorithm used for fMRI analysis [147], exploits HOS through the use of a fixed tangent hyperbolic nonlinearity. In contrast to Infomax, entropy bound minimization (EBM) [129] and entropy rate bound minimization (ERBM) [128] are two more recently introduced ICA algorithms and have been shown to provide desirable performance on both simulated and

real fMRI data, see *e.g.*, [4, 67, 128, 138], through the use of a dynamic nonlinearity, and in the case of ERBM, sample dependence of each source as well. The use of a dynamic nonlinearity enables EBM and ERBM to match a wide variety of distributions.

In order to estimate the demixing matrix \mathbf{W} , Infomax and EBM equivalently aim at minimizing the mutual information (MI) between the source estimates $\hat{\mathbf{s}}_1, \dots, \hat{\mathbf{s}}_N$, given by

$$\begin{aligned} \mathcal{I}(\mathbf{W}) &= \sum_{n=1}^N H(\hat{\mathbf{s}}_n) - H(\hat{\mathbf{S}}) \\ &= \sum_{n=1}^N H(\hat{\mathbf{s}}_n) - \log|\det\mathbf{W}| - H(\mathbf{X}) \end{aligned} \quad (2.2)$$

where $H(\cdot) = -\mathbb{E}[\log p(\cdot)]$ refers to (differential) entropy of a random variable, with p referring to the probability density function (PDF) of corresponding variable. The last term $H(\mathbf{X})$ is a constant as it is independent of \mathbf{W} . Expression in (2.2) can be written using ML formulation for the given observations. While ICA is achieved through the estimation of the demixing matrix \mathbf{W} , for the estimator to achieve the desirable large sample properties of the ML principle, the PDF of the sources needs to be modeled or estimated as well [4]. Among different versions of Infomax algorithms [12, 23, 123], the most widely used in fMRI data analysis is the original version proposed in [23]. In this version, the algorithm takes only HOS into consideration, and achieves this by using a fixed sigmoidal nonlinearity to model the source PDF [23], which implies a super-Gaussian PDF, which is a good match for the fMRI source, as well as a soft sparsity for the sources. This means that Infomax is a good match for very focal regions of activation, however, it might significantly bias latent sources relating to broad regions, such as the default mode network (DMN) [66]. In contrast to Infomax, EBM does not assume one specific distribution for the latent sources but instead attempts to upper bound their entropy through the use of several measuring functions [129]. Each of these functions provides bounds on the entropy, with the tightest bound being closest to the true entropy. The use of these measuring functions

makes it possible to match a wide variety of distributions, including those that are sub-Gaussian, super-Gaussian, unimodal, bimodal, symmetric, as well as skewed [129], thus potentially leading to more accurate estimation of the latent sources.

Instead of bounding the entropy of latent sources, ERBM attempts to bound their entropy rate using measuring functions. The cost function, thus, is given by

$$\mathcal{I}_r(\mathbf{W}) = \sum_{n=1}^N H_r(\hat{\mathbf{s}}_n) - \log|\det\mathbf{W}| - H_r(\mathbf{X}) \quad (2.3)$$

where $H_r(\hat{\mathbf{s}}_n) = H[\hat{s}_n(1), \dots, \hat{s}_n(V)]/V$ refers to the entropy rate of $\hat{\mathbf{s}}_n$, thus the goal is now minimizing the MI *rate* among the source estimates. Hence this cost function accounts for two types of diversity—sample dependence and nonstationarity—of the signals. ERBM models the sample dependence of fMRI data and filters the samples using a time-invariant invertible linear filter. Consequently, sample dependence is taken into consideration by ERBM. Since EBM and ERBM relax the assumptions placed on the fMRI sources by assuming flexible source distributions, they are expected to provide improved performance over Infomax. Additionally, ERBM is expected to have superior performance over EBM as well as Infomax, since it takes advantage of multiple underlying properties of fMRI sources, namely, HOS and voxel-wise dependence. All three algorithms can be found in the group ICA of fMRI toolbox (GIFT) (<http://mialab.mrn.org/software/gift/index.html>).

2.2.2 Sparsity as type of diversity: DL

DL is another data-driven method that has been successfully applied to fMRI analysis [1, 121] by making use of the sparsity property of latent sources as the starting point for the decomposition and aiming at balancing the decomposition accuracy and source sparsity through a regularization parameter. DL expresses the observations as sparse combinations of the atoms (columns) in a dictionary $\mathbf{D} \in \mathbb{R}^{T \times N}$, seeking to estimate the latent spatial components $\hat{\mathbf{S}} \in \mathbb{R}^{N \times V}$ that are conveyed in the sparse loadings. The cost of DL procedure

is given by

$$\ell(\mathbf{D}) = \min_{\mathbf{D}, \hat{\mathbf{S}}} \|\tilde{\mathbf{X}} - \mathbf{D}\hat{\mathbf{S}}\|_F^2 + \lambda \|\hat{\mathbf{S}}\|_1 \quad (2.4)$$

where $\hat{\mathbf{S}}$ are the spatial maps, $\|\hat{\mathbf{S}}\|_1 = \sum_{i=1}^N \sum_{j=1}^V |\hat{s}_{ij}|$, and λ is the regularization parameter that controls the level of sparsity of the sources. It is shown that the DL algorithm that achieves the decomposition using an online optimization algorithm is suitable for large datasets [142].

2.2.3 Balancing independence and sparsity: SparseICA

Since both independence and sparsity are natural properties of fMRI sources, a unified mathematical framework is proposed to account for both by incorporating a sparsity term—an ℓ^1 regularization term—of the source components into the cost function of ICA [35, 36]. The cost function of SparseICA-EBM, which is utilized to demonstrate the application of this framework, is constructed using two terms, *i.e.*, an independence term and a sparsity term. The independence refers to (2.2) and the sparsity is written as the sum of the regularization function of all estimates. The final cost function is given by

$$\mathcal{J}(\mathbf{W}) = \sum_{n=1}^N H(\hat{\mathbf{s}}_n) - \log|\det(\mathbf{W})| + \sum_{n=1}^N \lambda_n f(\hat{\mathbf{s}}_n) \quad (2.5)$$

$$f(\hat{\mathbf{s}}_n) = \lim_{\epsilon_n \rightarrow 0} \sum_{v=1}^V \sqrt{\hat{s}_{nv}^2 + \epsilon_n} \quad (2.6)$$

where $f(\hat{\mathbf{s}}_n)$ is the regularization term with respect to the n th source estimate $\hat{\mathbf{s}}_n$, λ_n is the sparsity parameter and ϵ_n is the smoothing parameter. The third term in (2.2) is removed here since it is a constant with respect to \mathbf{W} . By tuning the sparsity and smoothing parameters, SparseICA-EBM enables different decompositions that yield different estimates with different levels of sparsity.

2.3 Data-driven BSS techniques for multiple datasets

Typically the fMRI data is collected from multiple subjects, yielding multiple datasets. This leads to the development of effective algorithms that are able to jointly analyze multiple datasets by making use of the rich information among the datasets. There are a number of methods developed by either extending the methods for a single dataset that are introduced above to multiple datasets such as group ICA and IVA, or starting from another aspect such as MCCA.

2.3.1 Group ICA

The group ICA framework enables the analysis of multiple datasets using ICA and has become popular for the analysis of multi-subject fMRI data [46, 48]. Group ICA assumes a common signal space across datasets due to the fact that the extracted functional network components across different subjects are expected to share some similarity. To form a single dataset that is spanned by the common source components, group ICA adopts two steps of PCA, the subject level PCA and the group level PCA. The subject level PCA helps remove the effect of noise and the group level PCA helps extract the common signal subspace. Finally a single ICA is performed on the common signal matrix.

Suppose the observed fMRI data is collected from K subjects. Let the data from the k th subject be denoted by $\tilde{\mathbf{X}}^{[k]} \in \mathbb{R}^{T \times V}$, $1 \leq k \leq K$, where T denotes the number of time points and V denotes the number of voxels. For each subject, the subject-level PCA reduces the dimension of $\tilde{\mathbf{X}}^{[k]}$ from T to T' , computed as $\mathbf{X}^{[k]} = (\mathbf{F}^{[k]})^\dagger \tilde{\mathbf{X}}^{[k]}$, where \dagger represents the pseudoinverse and $(\mathbf{F}^{[k]})^\dagger \in \mathbb{R}^{T' \times T}$ is the subject level reduction matrix, whose columns are the eigenvectors of $\tilde{\mathbf{X}}^{[k]}(\tilde{\mathbf{X}}^{[k]})^T$ and the reduced data is $\mathbf{X}^{[k]} \in \mathbb{R}^{T' \times V}$. The reduced data matrix, $\mathbf{X}^{[k]}$, consists of the first T' principal components of $\tilde{\mathbf{X}}^{[k]}$ that represent the informative signals from the k th subject. It is assumed that the subjects share a common component

subspace [46]. In order to estimate the common subspace across subjects, the datasets are temporally concatenated to form a single data matrix $\tilde{\mathbf{Z}} \in \mathbb{R}^{KT' \times V}$, which is then reduced to $\mathbf{Z} \in \mathbb{R}^{N \times V}$ by a group level PCA, $\mathbf{Z} = \mathbf{G}^\dagger \tilde{\mathbf{Z}}$, with $\mathbf{G}^\dagger \in \mathbb{R}^{N \times KT'}$ as the group level reduction matrix and N as the order for the common observation subspace. Group components $\mathbf{S} \in \mathbb{R}^{N \times V}$ are then estimated by performing ICA on the common group subspace \mathbf{Z} , which subject to the same linear model in (2.1), to obtain the estimated sources as $\hat{\mathbf{S}} = \mathbf{W}\mathbf{Z}$. The use of a single ICA on the common subspace of all datasets helps to preserve the order of the components across subjects. Following the completion of ICA, back-reconstruction is performed on $\hat{\mathbf{S}}$ to generate the corresponding subject-specific source estimates $\hat{\mathbf{S}}^{[k]} \in \mathbb{R}^{N \times V}$. In order to obtain the back-reconstructed signals, $\hat{\mathbf{S}}^{[k]}$, the group level reduction matrix \mathbf{G}^\dagger is blocked by columns, $\mathbf{G}^\dagger = [(\mathbf{G}^{[1]})^\dagger, (\mathbf{G}^{[2]})^\dagger, \dots, (\mathbf{G}^{[K]})^\dagger]$ with $(\mathbf{G}^{[k]})^\dagger \in \mathbb{R}^{N \times T'}$ and, $\hat{\mathbf{S}}^{[k]}$ is reconstructed using $\hat{\mathbf{S}}^{[k]} = \mathbf{W}(\mathbf{G}^{[k]})^\dagger (\mathbf{F}^{[k]})^\dagger \tilde{\mathbf{X}}^{[k]}$. The corresponding subject-specific time courses are obtained using $\hat{\mathbf{A}}^{[k]} = \mathbf{F}^{[k]} \mathbf{G}^{[k]} \mathbf{W}^{-1}$.

In the group ICA framework, instead of performing an ICA on the common signal subspace $\mathbf{Z} \in \mathbb{R}^{N \times V}$, the other two algorithms, DL and SparseICA, can also be adopted to decompose \mathbf{Z} . Since DL does not require a square dictionary \mathbf{D} , one can also perform DL on the concatenated data $\tilde{\mathbf{Z}} \in \mathbb{R}^{KT' \times V}$ as long as DL is proven effective in separating the signal and noise or other artifacts from the data it is applied to.

2.3.2 IVA

Unlike group ICA, IVA extends ICA to the joint analysis of multiple datasets by effectively taking into account another form of diversity—the dependence across datasets [4, 111, 112]. We use random variable notations throughout the introduction of IVA for convenience. IVA assumes that each dataset is a linear mixture of N independent sources,

$$\mathbf{x}^{[k]}(v) = \mathbf{A}^{[k]} \mathbf{s}^{[k]}(v), \quad 1 \leq k \leq K, \quad 1 \leq v \leq V, \quad (2.7)$$

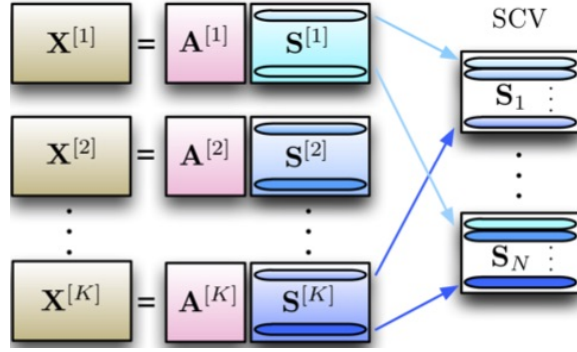


FIG. 2.3. The generative model of IVA

where $\mathbf{X}^{[k]} = [\mathbf{x}^{[k]}(1), \mathbf{x}^{[k]}(2), \dots, \mathbf{x}^{[k]}(V)] \in \mathbb{R}^{N \times V}$, $\mathbf{S}^{[k]} = [\mathbf{s}^{[k]}(1), \mathbf{s}^{[k]}(2), \dots, \mathbf{s}^{[k]}(V)] \in \mathbb{R}^{N \times V}$ and $\mathbf{A}^{[k]} \in \mathbb{R}^{N \times N}$ denote the observed dataset, the set of independent sources, and the invertible mixing matrix respectively. Different from in group ICA framework where the dimension of each observed data $\tilde{\mathbf{X}}^{[k]}$ is reduced to T' using a subject level PCA, the dimension of $\tilde{\mathbf{X}}^{[k]}$ is reduced to the model order N , *i.e.*, the number of sources, before applying an IVA decomposition on all the datasets. A general model of IVA is shown in Fig. 2.3. In addition to the assumption of independence among sources within a dataset, IVA makes effective use of dependence across multiple datasets by defining an SCV as $\mathbf{s}_n(v) = [s_n^{[1]}(v), s_n^{[2]}(v), \dots, s_n^{[K]}(v)]^T \in \mathbb{R}^{K \times 1}$, $1 \leq n \leq N$, by collecting corresponding components, where $\mathbf{s}_n^{[k]} \in \mathbb{R}^{V \times 1}$ is the n th source from the k th dataset. ICA can be achieved by minimizing the MI among the individual latent sources. After extending to multiple datasets, an IVA solution finds K demixing matrices by minimizing the MI among the SCVs, which results in the following cost function

$$\begin{aligned}
 C_{\text{IVA}}(\mathbf{W}) &= \sum_{n=1}^N \mathcal{H}(\mathbf{y}_n) - \sum_{k=1}^K \log|\det \mathbf{W}^{[k]}| \\
 &= - \sum_{n=1}^N \mathbb{E}\{\log p_n(\mathbf{y}_n)\} - \sum_{k=1}^K \log|\det \mathbf{W}^{[k]}| \quad (2.8)
 \end{aligned}$$

such that the estimated sources of each dataset are obtained as $\mathbf{y}^{[k]}(v) = \mathbf{W}^{[k]}\mathbf{x}^{[k]}(v)$ for $k = 1, \dots, K$, where $\mathbf{W} = \{\mathbf{W}^{[1]}, \mathbf{W}^{[2]}, \dots, \mathbf{W}^{[K]}\}$ denotes the demixing matrices, \mathbf{y}_n denotes the estimated SCV, and $\mathcal{H}(\cdot)$ denotes the (differential) entropy. Minimization of (2.8) is equivalent to maximization of likelihood through the general asymptotic equipartition property [4]

$$\mathcal{L}_{\text{IVA}}(\mathbf{W}) = \sum_{n=1}^N \log(p_n(\mathbf{Y}_n)) + V \sum_{k=1}^K \log|\det \mathbf{W}^{[k]}|, \quad (2.9)$$

where $\mathbf{Y}_n = [\mathbf{y}_n(1), \mathbf{y}_n(2), \dots, \mathbf{y}_n(V)]$, and $p_n(\cdot)$ denotes the multivariate probability distribution of n^{th} SCV. In both (2.8) and (2.9) the term that is constant with respect to \mathbf{W} associated with the observed data \mathbf{X} is ignored. For simplicity, throughout the work we consider the simpler independent and identical distribution case for IVA and do not take sample dependence into account.

IVA algorithm choice To maximize the likelihood, besides \mathbf{W} , we need to estimate the multivariate density function of SCV. The selection of the multivariate distribution, $p_n(\mathbf{y}_n)$, determines whether SOS and/or HOS of the data are taken into consideration. IVA-G assumes that the sources in an SCV are multivariate Gaussian distributed and only takes SOS into consideration [14]. This assumption guarantees a positive definite Hessian matrix of the cost at the global optimum hence providing a reliable estimation by using second-order optimization techniques such as using Newton updates. IVA with multivariate Laplacian distribution (IVA-L) assumes each SCV is modeled by the multivariate Laplacian distribution [111, 112]. The assumption is that the correlation matrix of an SCV is identity thus taking only HOS into consideration. IVA with multivariate generalized Gaussian distribution (IVA-MGGD) on the other hand assumes that an SCV is multivariate generalized Gaussian distributed [15, 16, 34]. IVA-MGGD calculates the whole correlation matrix and estimates the shape parameter of the MGGD that models each SCV, making it possible to

take both SOS and HOS into consideration. As a consequence, this algorithm is computationally complex but provides good performance. IVA-L with SOS (IVA-L-SOS) [27] calculates the whole correlation matrix of each SCV as in IVA-MGGD but fixes the shape parameter to 0.5 to model a multivariate Laplacian distribution which is a good match for fMRI sources. Hence it takes both SOS and HOS into consideration and simplifies the computational complexity compared with IVA-MGGD. Both IVA-G and IVA-L-SOS have proven powerful in extracting interpretable source components when applied to medical imaging data analysis [5, 14, 27].

2.3.3 MCCA

Another commonly used BSS algorithm for multiple datasets is MCCA, which starts from a different property—correlation—of the data hence is based on SOS only [110, 133]. MCCA assumes that the latent sources within each dataset are uncorrelated and estimates them by using a multistage deflationary correlation maximization scheme. Only one set of corresponding sources from multiple datasets—equivalent to an SCV in IVA—are estimated at a time by maximizing the correlation between them

$$\begin{aligned} \{\mathbf{w}_n^{[1]}, \mathbf{w}_n^{[2]}, \dots, \mathbf{w}_n^{[K]}\} &= \arg \max_{\mathbf{w}} \left\{ \sum_{i,j=1}^K |r_{i,j}^{(n)}| \right\} \\ \text{s.t. } \mathbf{w}_n^{[k]} &\perp \{\mathbf{w}_1^{[k]}, \dots, \mathbf{w}_{n-1}^{[k]}\} \text{ if } n > 1, \text{ for } k = 1, \dots, K, \end{aligned} \quad (2.10)$$

where $\mathbf{w}_n^{[k]}$ is the n th row of the demxing matrix \mathbf{W} for the k th subject, and $r_{i,j}^{(n)}$ is the element of $\mathbf{R}_n \triangleq \mathbf{E}\{\mathbf{Y}_n \mathbf{Y}_n^T\} \in \mathbb{R}^{K \times K}$ with $\mathbf{Y}_n \in \mathbb{R}^{K \times V}$ denoting the n th corresponding sources from K datasets, *i.e.*, the n th SCV. The magnitude of correlation between each pair of components within the estimated SCVs is in non-decreasing order, *i.e.*, $|r_{i,j}^{(1)}| \geq |r_{i,j}^{(2)}| \geq \dots \geq |r_{i,j}^{(N)}|$.

To measure the overall correlation among the corresponding sources, five objective

functions based on the augmented correlation matrix

$$\mathbf{R} = \begin{bmatrix} \mathbf{R}_1 & 0 & \cdots & 0 \\ 0 & \mathbf{R}_n & \cdots & 0 \\ \vdots & \vdots & \ddots & \vdots \\ 0 & 0 & \cdots & \mathbf{R}_N \end{bmatrix} \quad (2.11)$$

are introduced in [110]. Two objective functions are, respectively, sum and sum of squares of all entries in the correlation matrix, *i.e.*, SUMCOR and SSQCOR. The other three are based on the eigenvalues of the correlation matrix, *i.e.*, MAXVAR that only considers the maximum eigenvalue, MINVAR that only considers the minimum eigenvalue, and GENVAR that takes all the eigenvalues into consideration. Since the correlation among the sources within each SCV is maximized, the goal for each cost—mostly ad-hoc in nature—is trying to make the correlation matrix as ill-conditioned as possible. MCCA with GENVAR cost function (MCCA-GENVAR) can be shown to have the same cost function as IVA-G [14] if the demixing matrices are assumed to be orthogonal [4]. IVA generalizes MCCA due to the fact that IVA is a more flexible model that simultaneously estimates all the demixing matrices.

2.4 Summary

In this chapter, we briefly presented the background for our work. We first introduced the acquisition of fMRI data, the analysis of multi-subject resting-state fMRI data, and the resting-state COBRE data that is used in this work. We emphasized the popularity of data-driven BSS methods in the analysis of fMRI and two major types of diversity— independence and sparsity—that have shown useful in fMRI analysis. We then introduced a number of widely used BSS algorithms such as ICA, DL, IVA, MCCA, and the recently proposed framework SparseICA. For each algorithm, we discussed the diversity it uses

through a detailed introduction of its objective function. We presented the general IVA model and that it provides a flexible framework for the analysis of multi-subject fMRI data and hence generalizing MCCA. We apply these algorithms to the COBRE data with different research goals throughout this work to show their effectiveness and/or limitations and develop new methods by leveraging the strengths of these algorithms especially IVA.

Chapter 3

THE ROLE OF DIVERSITY IN MULTI-SUBJECT FMRI DATA ANALYSIS

ICA and DL are two popular data-driven methods that are based on two different forms of diversity, statistical independence for ICA and sparsity for DL. Despite their popularity, the comparative advantage of emphasizing one property over another in the decomposition of fMRI data is not well understood. Such a comparison is made harder due to the differences in the modeling assumptions between ICA and DL, as well as within different ICA algorithms where each algorithm exploits a different form of diversity as introduced in Chapter 2.2. In this chapter, we demonstrate that the objective global measures, such as time course frequency power ratio, network connection summary and graph-theoretical metrics, are good choices for performance assessment. We gain insight into the role that different types of diversity have on the analysis of fMRI data. Four ICA algorithms that account for different types of diversity and one DL algorithm are studied. We apply these algorithms to multi-subject fMRI data for a thorough comparison of their performance.

3.1 Introduction

The differences in separation performance for separate ICA algorithms, such as Infomax, EBM and ERBM, are related to differences in their assumed latent source models. Most ICA algorithms can be cast under the ML framework and their performance is a

function of the assumed source distribution, or the nonlinearity that is used which implies a specific type of distribution. On the other hand, DL aims at balancing the decomposition accuracy and source sparsity through a regularization parameter and in the estimation of functional networks of interest, there is no implicit or explicit assumption of a source distribution. SparseICA framework enables a joint exploration of independence and sparsity by penalizing the ICA cost function with a sparsity term. Therefore, SparseICA inherits the advantages of ICA with enhanced performance due to the exploitation of sparsity when the sources are sparse. Though the desirable performance of SparseICA has been shown using simulated fMRI data, it has not been tested on real fMRI data.

Both independence and sparsity have demonstrated their utility for the analysis of fMRI data, however there is no study that explores the role of each type of diversity in terms of global metrics for real fMRI datasets. Few studies that have investigated the performance of Infomax, EBM and ERBM [61, 67] used a limited number of subjects and based the evaluation on subjective metrics, such as visual inspection of a few well-matched components [4, 67]. Additionally, there has been no comparison of the performance of these methods with the SparseICA framework and DL. Such an exploration raises the issue of how to determine a metric for comparing the component estimation performance of different data-driven algorithms on real fMRI data without a ground truth. Algorithmic comparison is difficult as decompositions can be quite different depending on the modeling assumptions of a particular algorithm, thus matching of all the estimated components one-to-one is usually not possible. In addition, each method is based on a different cost function. This motivates the identification of objective global metrics that are independent of cost function for algorithmic performance.

In this chapter, we provide insight into the role of different types of diversity on a decomposition of multi-subject fMRI data. For this task, we choose Infomax, EBM, ERBM,

online DL [142], and SparseICA-EBM for comparison because they are good representations of algorithms that use different types of diversity as we detailed in Chapter 2.2. Infomax is one of the most widely used data-driven algorithms for the task. EBM, on the other hand, provides a more flexible estimation of source distribution thus enabling better fulfillment of independence among the sources while ERBM extends EBM to account for sample dependence. DL puts the emphasis on sparsity, and SparseICA-EBM balances the roles of the two types of diversity, independence and sparsity. The relative performance of these algorithms is assessed on the resting COBRE data that consists of 179 subjects, which is a relatively large dataset. Due to the increasing number of large fMRI datasets that include hundreds or even thousands of subjects, understanding the performance of these techniques in this scenario increases our confidence in the generalizability of the results. Note that each algorithm has its own target cost function thus using the cost for performance assessment is not possible. Even if the algorithms had the same cost function, the lowest value of the cost function does not necessarily lead to better separation results depending on the overall goal. In order to be fair to each algorithm, we propose to use objective global measures, *e.g.*, time course frequency power ratio [11, 163], network connection summary [68, 140] and graph-theoretical metrics [39, 178]. Time course frequency power ratio indicates whether a component is describing the BOLD response in fMRI data or not. Network connection summary provides a general idea on how well each algorithm can reconstruct the complex connections in the brain. Graph-theoretical metrics are an efficient tool for studying the heterogeneity between different groups of subjects, such as patients with SZ and HCs [9, 21, 139, 187]. These metrics perform a global comparison of the algorithms based on all the components or the whole brain functional connectivity.

3.2 Global metrics for performance assessment

Following are the three global measures that are used in this work to demonstrate the powerfulness of global metrics in performance assessment.

3.2.1 Frequency analysis

The first global measure is the ratio of time course power spectra in low-frequency band ($< 0.1\text{Hz}$) to the high-frequency band ($> 0.15\text{ Hz}$) for each component. Since the activation in the components is due to the BOLD response, which captures the spontaneous slow fluctuations of correlated activity in the resting brain hence corresponding to low frequencies, higher power ratios imply that the components are more closely associated with true neural function. Conversely, the lower the ratio, the more likely the component is to be describing the cardiac or respiratory noise as opposed to true BOLD activation [11,60].

3.2.2 Network connection summary

Another global measure of the performance is the network connection summary. For each algorithm, N_{post} components out of N that refer to brain functional networks are selected based on their time course power ratio and visual inspection. The two-stage procedure helps us to ensure that components with meaningful functional regions are included in the post analyses. If some of them are removed or some noisy components and components with heavy ventricle effects are included in the post analyses, the results may change. First, all the components are separated into two categories, one containing those with time course power ratio higher than a threshold t_{PR} , and the other set containing the remaining ones. Through visual inspection the components with large edge effects and ventricles are removed from the first category, and those whose power ratios are slightly lower than t_{PR} but with activation in meaningful functional network regions are put back to the first

category, which is finally used for network connection analysis. Using time course power ratio to separate components into two categories in the first step significantly reduces the difficulty of visual inspection in the second step.

The components extracted from data-driven methods generally have some dependence due to their functional relevance. Consequently, after identifying the functional networks that are conveyed in the components, we estimate brain connectivity by calculating the full-order statistical dependence, MI, among them. The functional network connectivity is constructed using normalized MI, $I_{\text{norm}}(\hat{\mathbf{s}}_1, \hat{\mathbf{s}}_2)$, as the measure. The normalized MI is given by

$$e(\hat{\mathbf{s}}_1, \hat{\mathbf{s}}_2) = I_{\text{norm}}(\hat{\mathbf{s}}_1, \hat{\mathbf{s}}_2) = \frac{2I(\hat{\mathbf{s}}_1, \hat{\mathbf{s}}_2)}{I(\hat{\mathbf{s}}_1, \hat{\mathbf{s}}_1) + I(\hat{\mathbf{s}}_2, \hat{\mathbf{s}}_2)} \quad (3.1)$$

where $I(\hat{\mathbf{s}}_1, \hat{\mathbf{s}}_2)$ is the MI between two estimated components $\hat{\mathbf{s}}_1$ and $\hat{\mathbf{s}}_2$. The performance of three Shannon entropy based MI estimation methods, the k-nearest neighborhood [83], the analytical formula corresponding in the chosen exponential family [154] and the Parzen window based method [158] are investigated. The former two methods are from information theoretical estimators toolbox (<https://bitbucket.org/szzoli/ite/>). Our exploration shows that for observations with super-Gaussian distribution, the method proposed in [158] performs the best, and is used in our work. After the normalization, the connectivity between two similar sources becomes close to 1 and that of two dissimilar sources close to 0.

The complete brain network connections are summarized based on the N_{post} identified functional networks with the normalized MI as connectivity measure. Connectivity patterns within the meaningful functional modules, such as the default mode cluster, are expected to be observed [10, 193]. Compact connections within modules improve the results of post analyses, such as clustering, on these estimated networks. To measure the modularity of the functional networks, the ratio of the average intra-module connectivity to the average

Metric	Abbreviation	Description
Nodal metrics (globally calculated)		
Degree	–	Number of links directly connected to node i
Characteristic path length	PL	Average distance of node i to all the others
Global efficiency	–	Communication efficiency of node i with all the others
Centrality		
Betweenness centrality	–	} Prominence of node i in information transfer in network
Closeness centrality	–	
Eigenvector centrality	–	
Global metrics		
Clustering coefficient	CC	Measure of functional segregation of the network
Small-worldness	SW	Quantifying the ability of combining functional integration and segregation

Table 3.1. Description of graph-theoretical metrics in both node and graph level.

inter-module connectivity is defined as:

$$R_m = \frac{\frac{1}{N_{\text{intra}}} \sum_i^Q \sum_u^{N_i} e_u}{\frac{1}{N_{\text{inter}}} \sum_{i,j}^Q \sum_v^{N_{i,j}} e_v} \quad (3.2)$$

where Q is the number of modules, N_i is the number of connections within the i th module, $N_{i,j}$ is the number of connections between the i th and j th modules, e_u and e_v refer to the intra- and inter-module connectivity respectively, and N_{intra} and N_{inter} refer to the total number of intra- and inter-module connectivity, again respectively. The larger the ratio, the more compact the modules are.

3.2.3 Graph-theoretical metrics

We also use graph-theoretical metrics as global measures of performance comparison. For each algorithm and subject, the N_{post} selected components are used to construct the graph. With the N_{post} components of interest as nodes and the normalized MI between them as the edges, a fully connected graph, G , is constructed. Beginning with G , an edge threshold, e_t , is used to retain only the highest P_e percent of the edges, thus generating a new graph G' . We define the percentage of the edges that remain after thresholding as the link density, which increases as the threshold decreases. The weighted graphs are binarized,

with the edges below the threshold e_t having a value of 0 and those above having a value of 1. In order to avoid very sparse graphs with small link densities and those with too high link densities, we limit the link density to range from 20% to 70%.

Graph metrics highlight different topological characteristics of graphs, see *e.g.*, [31,39,40]. The characteristic path length, global efficiency and centrality are measures that can quantify the ability of a node to facilitate functional integration in graphs [164]. These are global measures as all the nodes are taken into consideration in their calculation, and provide measures of how information is transferred in the functional network. The clustering coefficient can capture the segregation of networks by measuring the transfer of information in the immediate neighborhood of each node. We use global graph clustering coefficient that is averaged across all the nodes. The small-worldness (SW) of the network is also calculated to measure the degree of small-world organization in the overall functional network. Table. 3.1 presents the metrics that are used in this work. The formulas of these metrics are described in detail in [32,33,164]. All the implementations are performed using Matlab code from the Brain Connectivity Toolbox (<https://sites.google.com/site/bctnet/>).

3.3 Experimental results

3.3.1 Implementation

Model order One important parameter in the application of an ICA algorithm is the model order, *i.e.*, the order of signal subspace, N . However, for fMRI data, classical order estimation techniques based on information theoretic criteria may overestimate the order due to the inherent sample dependence of fMRI data [130, 132]. A common way to overcome this issue is by using downsampling to obtain effectively independent and identically distributed samples [130, 132]. However, methods based on downsampling suffer from a loss of information associated with it. More recently, two entropy rate (ER)-based order estimation techniques are proposed that account for sample dependence without the use of

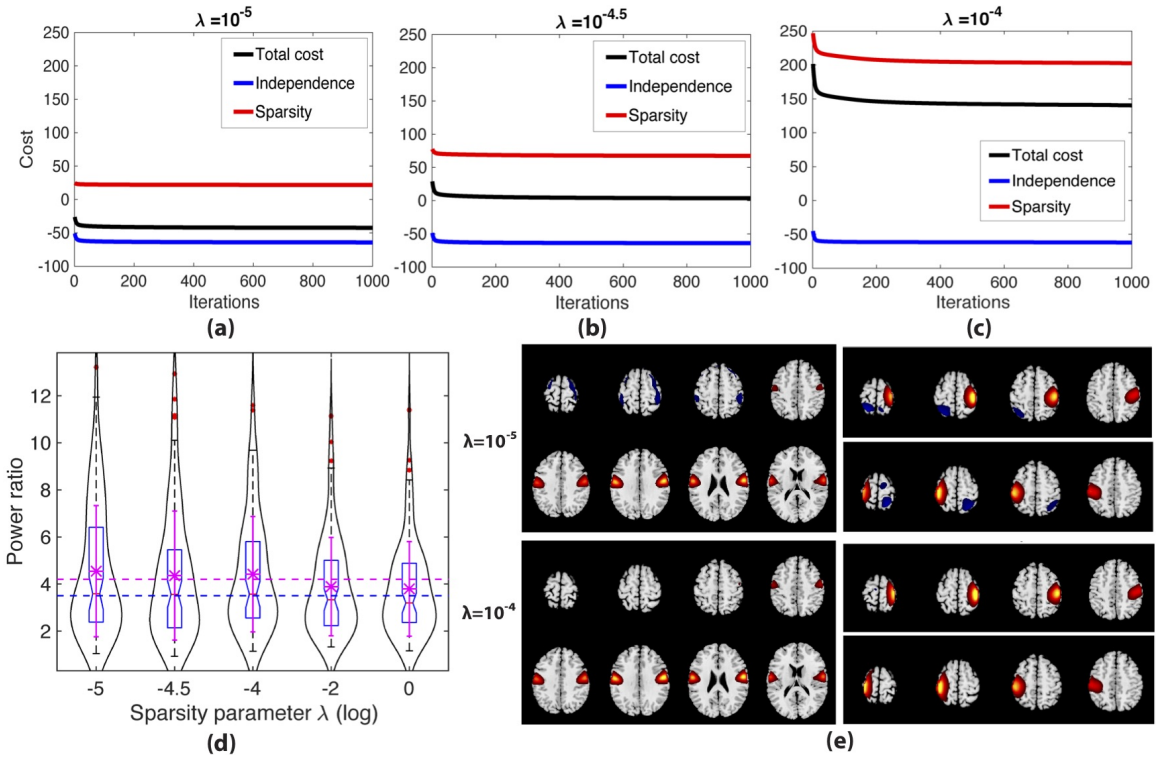


FIG. 3.1. The relative contribution of statistical independence and sparsity (a)–(c) in SparseICA-EBM, the violin plot of the time course power ratio (d) and the spatial maps of motor components estimated by SparseICA-EBM when $\lambda_s = 10^{-5}$ and $\lambda_s = 10^{-4}$ (e). In (a)–(c), the x-axis denotes the number of SparseICA-EBM iterations and y-axis denotes the cost. In (e), Z-maps corresponding to the mean components averaged across all subjects for motor components are shown. The maps are thresholded using a threshold $Z_t = 2$.

downsampling: ER using a finite memory length model (ER-FM) and ER using an autoregressive model (ER-AR) [78]. Since the sample correlation structure in ER-FM is a better match to that in fMRI data due to the finite span of correlation in the point spread function, ER-FM is used to estimate the order of signal subspace. The mean and standard deviation of the order across subjects are 72.86 ± 10.40 . We use an order equal to the mean plus one standard deviation, which is rounded up to 85 to retain a significant level of the signal across multiple subjects while introducing minimal noise. The use of this high model order is also well motivated in the literature for achieving a more useful functional segmentation of the brain, see *e.g.*, [11, 113].

Finally, in group ICA, the order of subject-level PCA is set to $T' = 100$, a little higher than 85, seeking to retain as much variability as possible [71]. In DL, we first try to determine a decomposition without any dimension reduction but this results in very noisy estimates regardless of the parameter values. We thus perform subject-level PCA using the same order, T' , with group ICA, then perform DL on the concatenated data, $\tilde{\mathbf{Y}} \in \mathbb{R}^{KT' \times V}$, and set the number of dictionary atoms to be 85, which is estimated by ER-FM in a data-driven manner.

Back-reconstruction Direct group ICA back-reconstruction (GICA) is used to obtain subject-specific time courses and spatial components for the ICA algorithms [48]. Group ICA estimates the group components after performing two levels of PCA on the original data as introduced in Chapter 2.3.1. GICA provides a clear flow of the back-reconstruction of the subject-specific time courses and spatial components [71] as all the dimension reduction matrices in PCA are known. Indirect back-reconstruction approaches, that is, spatio-temporal regression, or dual regression as used in [22, 52] for fMRI analysis can also recover the subject-specific time courses and spatial components. In this article, we perform spatio-temporal regression, which is the most suitable back-reconstruction ap-

proach for DL to obtain the time courses and spatial maps. Because only the dictionary \mathbf{D} is given by the online DL and regression is suggested for the recovery of the spatial maps given a dictionary \mathbf{D} [142]. To make the DL estimates comparable with those from ICA, GICA1, a GICA back-reconstruction method that partitions the group-level PCA reducing matrix \mathbf{G}^\dagger as described in Chapter 2.3.1, is used to perform back-reconstruction for ICA, since it has been shown to have similar performance to dual regression [71].

Random initialization is used for each algorithm. For DL, the dictionary \mathbf{D} is randomly initialized from the input data. The most stable run is selected using minimum spanning tree method [66] for EBM from 10 runs and for ERBM and SparseICA-EBM from 25 runs. We use fewer number of runs for EBM because compared with ERBM and SparseICA-EBM, EBM takes only HOS as type of diversity into consideration, resulting in less variability across solutions. Hence using smaller number of runs is sufficient for EBM to provide a robust solution compared with ERBM and SparseICA-EBM. For Infomax, multiple runs are performed and the result shows that the spatial maps and time course power ratio statistics are very similar across different runs. Multiple runs are not performed for DL due to the consistency of its decompositions. Using back-reconstruction, the 85 components are estimated for individual subjects associated with their time courses. All the post analyses in this chapter are performed on the mean components that are generated by averaging the back-reconstructed components across all subjects.

SparseICA-EBM As introduced above, SparseICA-EBM seeks to achieve the decomposition by balancing the roles of independence and sparsity using a sparsity parameter λ_n , which enables the sparse solution for the n th source, $\hat{\mathbf{s}}_n$. The balance between independence and sparsity can be adjusted by tuning λ_n . Smaller λ_n in (2.5) emphasizes statistical independence while larger λ_n places greater weight on the sparsity of the sources. Another parameter for SparseICA-EBM is the smoothing parameter ϵ_n . Since in (2.5), the regular-

ization term, $f(\hat{\mathbf{s}}_n) = \|\hat{\mathbf{s}}_n\|$, is non-differentiable, it is replaced by the sum of multi-quadratic functions [122], as given by (2.6). A higher smoothing parameter ϵ_n will produce smoother sources [36]. However, the effect of this parameter with application to the analysis of real fMRI data has not been explored. For this reason, in this work, different values of λ_n and ϵ_n are considered. We use the same regularization and smoothing parameters for all estimates, thus the index n is dropped, resulting in λ_s and ϵ . As noted in [36], higher values of ϵ yield consistent results across different levels of noise and sparsity and lead to decompositions that are better than those of lower values. While for λ_s , the performance varies based on the sparsity levels of the sources. Hence, we first try to find a suitable value of λ_s for our dataset by fixing $\epsilon = 10$, a relatively high value. Further, with the selected λ_s , different values of ϵ are used. The final values of each parameter are selected by investigating the cost function, spatial maps and time course power ratio.

In order to select λ_s , a wide range of values from 10^{-8} to 10^4 are used to study the contribution of independence and sparsity in the sparse ICA cost function. As shown in Fig. 3.1(a) and (c), when $\lambda_s = 10^{-5}$, the independence term is larger which means that independence contributes more and when $\lambda_s = 10^{-4}$, sparsity contributes more. For $10^{-4.5}$, the contribution of independence and sparsity is balanced as seen in Fig. 3.1(b). The spatial components are visually inspected for different values of λ_s . We notice that the decomposition fails to estimate all possible latent sources when λ_s is too large (*e.g.*, $\geq 10^2$). The estimated sources are very focal, which means that the activated area of this estimate is compact with little noise and similar components are estimated multiple times. This comes at the cost of not estimating sources whose activated area is expected to be larger or dispersive, such as the DMN and frontoparietal, which are of interest in resting-state fMRI data [11, 84]. When λ_s is small (*e.g.*, $\leq 10^{-6}$), the decomposition becomes very similar to that of EBM, *i.e.*, sparsity scarcely contributes in these cases.

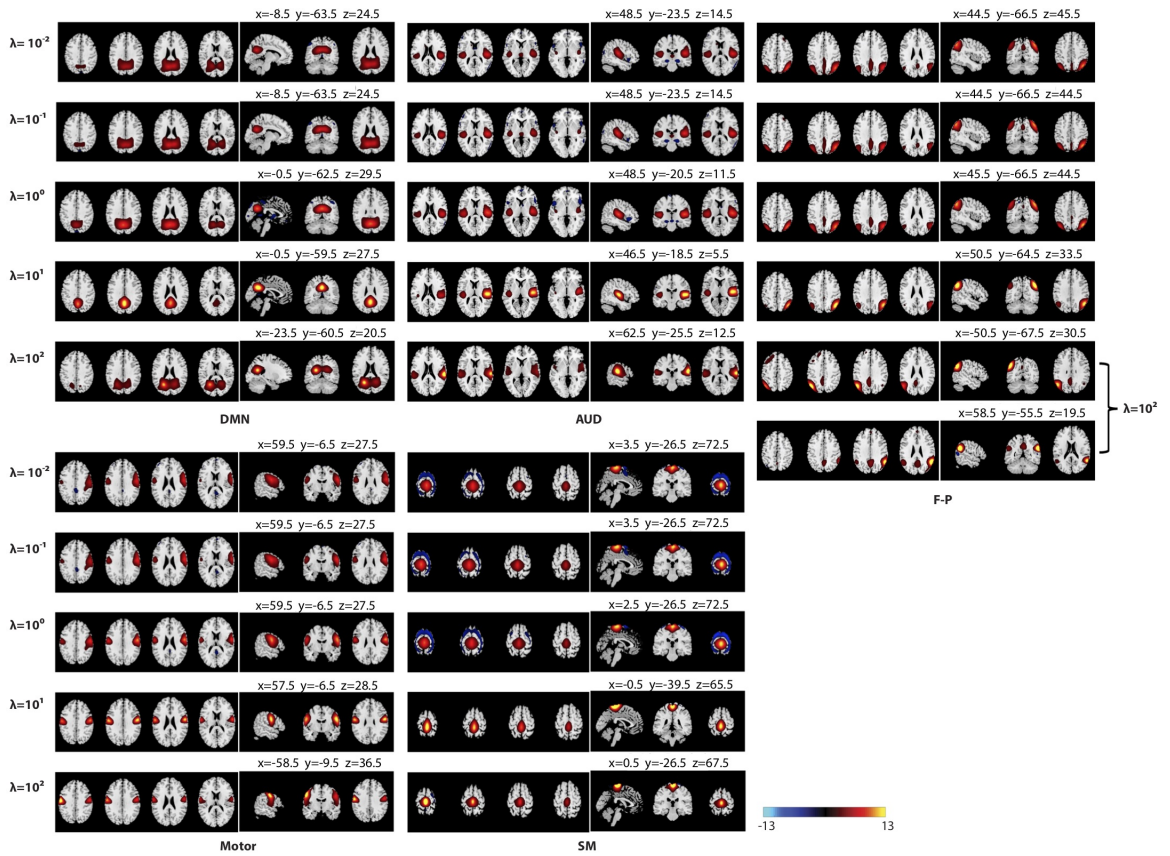


FIG. 3.2. Comparison of several components from DL using different values of λ . Z-maps corresponding to the mean components averaged across all subjects for DMN, auditory (AUD), motor, sensorimotor (SM) and frontoparietal (F-P) component are shown. The maps are thresholded using a threshold $Z_t = 2$. The peak coordinates in mm are shown to the right. Note that for $\lambda = 10^2$, there are two FP components that are estimated.

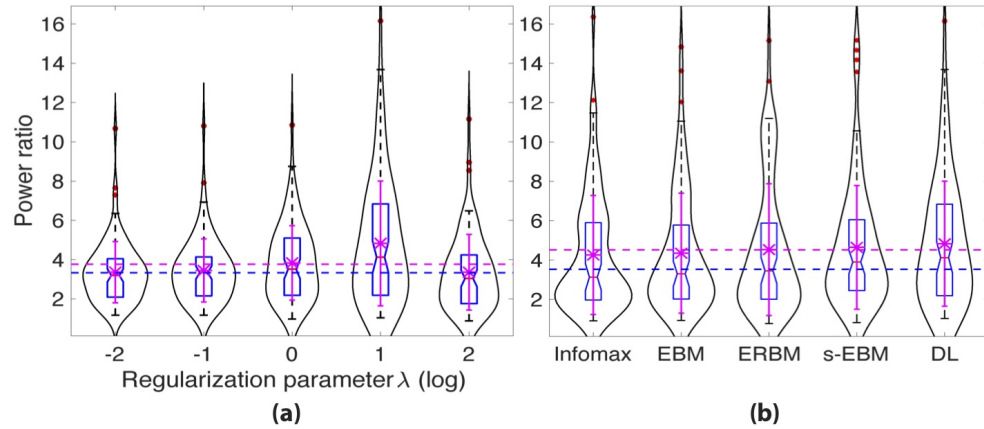


FIG. 3.3. The violin plot of the time course power ratio for all 85 mean components of (a) DL using different values of λ and (b) five algorithms. Note that s-EBM refers to SparseICA-EBM.

The frequency power ratio of time courses for different values of λ_s is shown in Fig. 3.1(d). Only those values of λ_s that between 10^{-5} and 0 are investigated. The black curve is the smoothed density histogram of power ratios of all subjects. The box plot displays the median, the 25th and 75th percentiles of the time course power ratio with whiskers extending to the 99.3% confidence interval and some outliers in red asterisks beyond whisker. The mean and standard deviation are shown in magenta. Horizontal magenta and blue lines refer to the global average, 4.20, and median power ratio, 3.50, across components from all decompositions, respectively. From Fig. 3.1(d), we can see that when $\lambda_s = 10^{-4.5}$, the independence and sparsity is balanced, the decomposition does not give the best statistics for power ratio summary. The mean, 25th and 75th percentiles are lower for $\lambda_s = 10^{-4.5}$ as compared with $\lambda_s = 10^{-5}$ and $\lambda_s = 10^{-4}$. Even though when $\lambda_s = 10^{-5}$ (with mean as 4.55 and median as 3.58), the decomposition gives slightly better power ratio summary than when $\lambda_s = 10^{-4}$ (with mean as 4.42 and median as 3.57). The components when $\lambda_s = 10^{-4}$ look more focal compared with those when $\lambda_s = 10^{-5}$, *e.g.*, in Fig. 3.1(e), the motor components when $\lambda_s = 10^{-4}$ are cleaner than that when $\lambda_s = 10^{-5}$. Therefore, we decide to use

$\lambda_s = 10^{-4}$, in which case that sparsity contributes slightly more than independence.

To explore the influence of ϵ , we fix $\lambda_s = 10^{-4}$ and change the value of ϵ from 10^{-2} to 10^4 . By visual inspection, we notice that with small ϵ (*e.g.*, ≤ 1), certain components are estimated repeatedly. Most of the repeated components are the ventricle components whose activated regions are focal and localized. Usually, the time course power ratio of ventricle component is low. But when they are estimated repeatedly, some of the repeated ones have power ratios as high as 10. Though this leads to slightly better power ratio, they are not reliable. For larger ϵ (*e.g.*, ≥ 10), the spatial maps are not estimated repeatedly. The power ratio statistics are higher when $\epsilon = 10^2$ (with mean as 4.65 and median as 3.90) than when $\epsilon = 10$ (with mean as 4.42 and median as 3.57), $\epsilon = 10^3$ (with mean as 4.57 and median as 3.47) and $\epsilon = 10^4$ (with mean as 4.37 and median as 3.69). Therefore, we use $\lambda_s = 10^{-4}$ and $\epsilon = 10^2$ for SparseICA-EBM.

DL There is only one regularization parameter λ for DL. The performance of DL is highly dependent on the selection of λ to achieve a desirable tradeoff between accuracy and level of sparsity. Different values, from 10^{-2} to 10^2 , are explored to study its effect on the performance for our relatively large real fMRI data. Another parameter to be determined is the number of atoms in dictionary, and in this work, we set the number of atoms to be $N = 85$, the order of signal subspace estimated by the data-driven order selection method ER-FM. For each λ , we check both the spatial components and the time course frequency power ratio. Components estimated from smaller λ are much noisier than those from larger λ , which can be seen from the examples in Fig. 3.2. The activated area of the spatial maps from $\lambda = 10^2$ is a little smaller than that from $\lambda = 10$. Additionally, components from $\lambda = 10^2$ are not well-aligned with those from the other values of λ , and some of them seem to split, such as the frontoparietal component as shown in Fig. 3.2. Power ratio distributions obtained for each λ are shown in Fig. 3.3(a). Notice that when $\lambda = 10$, both the mean, 4.83,

and median, 4.12, are much higher than the global mean, 3.76, and median, 3.33. When $\lambda = 10$, the decomposition appears to provide the best performance, and hence we use this value for DL in our further experiments.

3.3.2 Power ratio comparison

Spatial maps of a set of mean components from each algorithm are shown in Fig. 3.4. These are selected among the components that can be easily matched. For those functional networks that only contain one single relevant area, all five algorithms produce a good decomposition. However, for the DMN component, EBM and ERBM estimate more relevant activated areas since they use a more flexible density estimation model. Infomax only uses a fixed unimodal super-Gaussian density model which can hurt the quality of its decomposition if the data does not correspond to this model. Consequently, the components estimated by Infomax all have very focal activated areas and have similar PDFs. SparseICA-EBM and DL emphasize the sparsity of the sources, which makes the estimated components have fewer activated voxels outside the regions of interest. However, the amplitude levels in the parietal regions marked by the cyan circles in Fig. 3.4 for the DMN component from Infomax, SparseICA-EBM and DL are significantly lower than that from EBM and ERBM.

The time course power ratio comparison of the 85 mean components among the five algorithms is shown in a violin plot in Fig. 3.3(b). Horizontal magenta and blue lines refer to the global average, 4.52, and median power ratio, 3.53, across components from all five algorithms, respectively. The results indicate that Infomax yields the lowest mean, 4.26, and median, 3.13, of the power ratio and DL yields both the highest mean, 4.83, and median, 4.12. This implies that emphasizing sparsity results in components that are more likely to be related to BOLD signal on average.

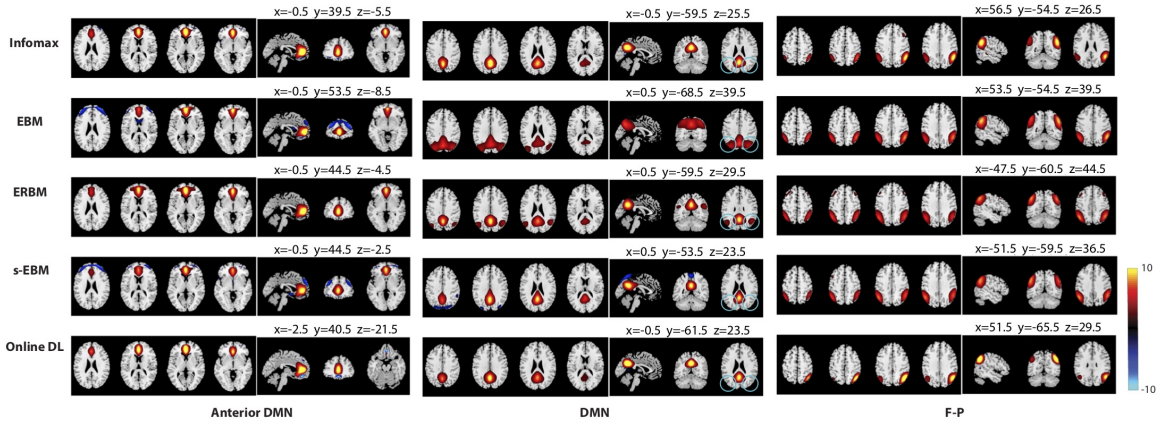


FIG. 3.4. Comparison of several components from five algorithms. Z-maps corresponding to the mean components averaged across all subjects for the anterior DMN, DMN and frontoparietal (F-P) component are shown. The maps are thresholded using a threshold $Z_t = 2$. The peak coordinates in mm are shown to the right. Note that s-EBM refers to SparseICA-EBM.

3.3.3 Network connection summary

In order to find N_{post} functionally relevant components to construct the network connection, a threshold of t_{PR} is selected by rounding off the global median value (3.53) across all components from all five algorithms to the closest integer less than this value, which is selected as $t_{\text{PR}} = 3$ experimentally. Finally, $N_{\text{post}} = 50$ components corresponding to known networks are selected for each algorithm. The network connection summary of the 50 mean components is created for each algorithm using the normalized MI as a measure. We group these components into six domains, motor, cognitive control (COG), default mode (DM), auditory (AUD), visual (VIS) and cerebellum (CB), according to their anatomical and presumed functional properties as in [11]. Fig. 3.5 shows the composited spatial maps for each cluster, the functional network connectivity matrix and the network connection summary for EBM. The functional network connectivity matrix exhibits some patterns of the brain network connection, for example, the modular organization within motor, DM and so on. These patterns are consistent with the observations in prior literature [10, 193]. The

connection summary visually illustrates these patterns. The intra- and inter-module connectivity ratio R_m is 2.4, 3.2, 1.9, 3.1 and 1.7 for Infomax, EBM, ERBM, SparseICA-EBM and DL, respectively. This reveals that EBM and SparseICA-EBM yield better clustering within each functional network cluster rather than across.

3.3.4 Graph-theoretical analysis

A graph-theoretical analysis is performed on the selected 50 components for each subject. The graph, G , is formed, where the retained components are nodes and pairwise normalized MI between the spatial components forms the edges. For each binarized graph, G' , both the nodal and global metrics are calculated. Permutation testing [41, 194] is performed on nodal metrics to obtain the corrected p -value to detect the significance level ($p < 0.05$) of difference between SZ and HC groups. For each nodal graph metric, 10,000 random permutations are generated independently. We first perform two-sample t -test on the graph metric based on the SZ and HC groups, and record the test statistic, t_0 . To implement the permutation test, all the subjects are randomly divided into two groups. A two-sample t -test is performed between the two groups in each division and all the test statistics are stored. Finally, the p -value is calculated by counting the number of permutations for which the test statistic is greater than t_0 and normalizing by 10,000. In order to prevent nodes from being declared significant by chance, only those nodes that show significant differences in at least three successive graphs are declared to be truly significant.

Our results reveal that for the globally calculated nodal graph metrics, *i.e.*, degree, characteristic path length, global efficiency and three versions of centrality, more components from ERBM show consistent significance in graphs for the majority of link density values, which gives us a greater ability to explore the differences between the patient and control groups. Fig. 3.6 shows the plot for the number of significant components at each link density for path length and betweenness centrality, and the plots for the other nodal

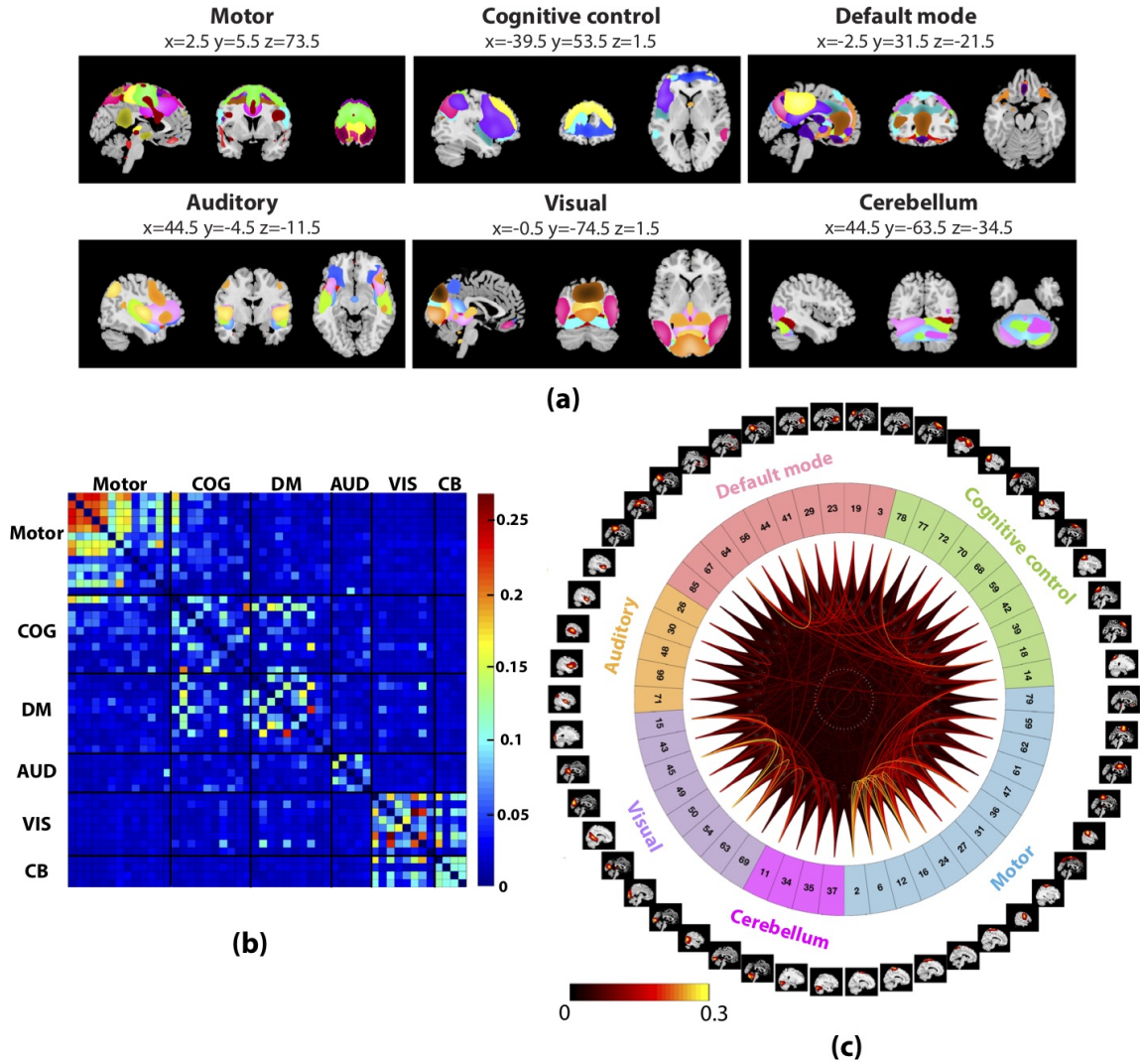


FIG. 3.5. Network connection summary of components from EBM. (a) Spatial maps of 50 functional networks. Functional networks are divided into groups based on their anatomical and functional properties. COG: Cognitive control; DM: default mode; AUD: auditory; VIS: visual; CB: cerebellum. (b) The functional connectivity matrix. Connectivity is measured using normalized MI. (c) Network connectivity visualization. The outermost circle demonstrates one slice of the spatial map of individual mean component. The colored circle indicates the index corresponding to each component and different colors refer to different functional network clusters. Curves in the center carry the exact connectivity among these components.

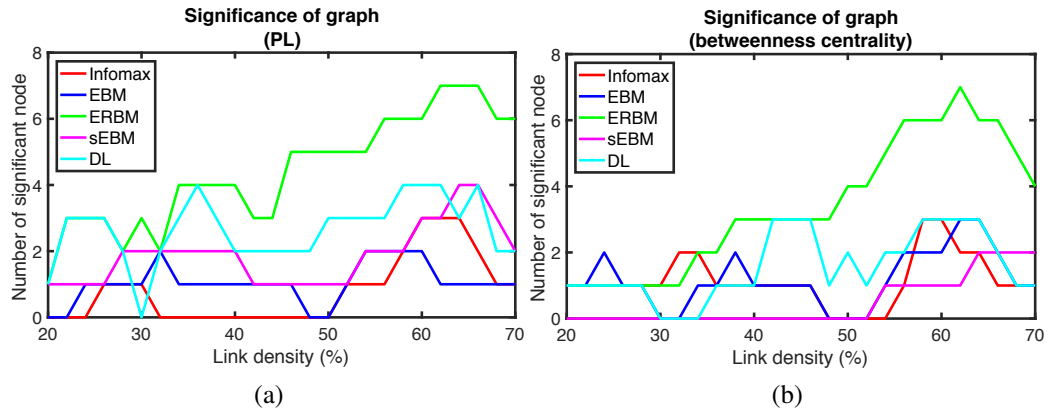


FIG. 3.6. Number of nodes showing significant group difference in each graph as a function of link density for (a) characteristic path length (PL) and (b) betweenness centrality. Note that s-EBM refers to SparseICA-EBM.

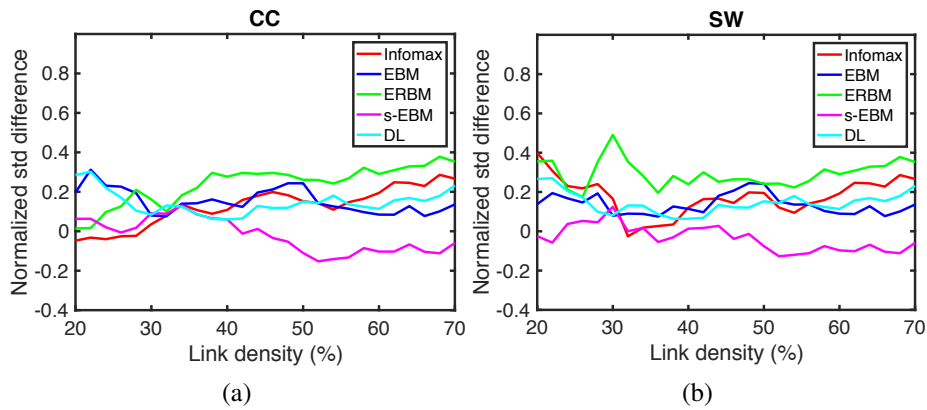


FIG. 3.7. Comparison of the normalized STD of (a) clustering coefficient (CC) and (b) small-worldness (SW) in SZs and HCs. Note that s-EBM refers to SparseICA-EBM.

graph metrics are similar with these two (not shown here due to the space limitation).

Fig. 3.7 compares the standard deviation (STD) of clustering coefficient and SW between SZs and HCs. Usually, higher variability is expected for SZs than for HCs in fMRI analysis [64]. The normalized STD difference is calculated by first subtracting the STD of HCs from that of SZs then normalizing it by the STD of HCs. The result reveals that ERBM yields the highest contrast between SZs and HCs using both clustering coefficient

and SW.

3.3.5 Discussion

We consider two key classes of data-driven algorithms used for multi-subject fMRI data analysis, those that are based on independence and sparsity and compare their performances by fully taking the properties of the task, fMRI analysis, into account. We also include a promising new method SparseICA in the comparison that balances the contribution of the two objectives and demonstrate its first application to real fMRI data. An important goal of this article has been providing feedback to practitioners who are mainly focused on using the methods without the need to perform full performance evaluations. We address issues in two categories in that respect in this section.

Parameter selection Parameter choice for optimized performance is always an important issue, and for practitioners, this might not always be an easy task, especially for approaches that aim to include the right amount of sparsity through regularization parameters into the decomposition such as DL and SparseICA. We investigate the influence of parameters in SparseICA-EBM and DL, and rather than using cross-validation that focuses on prediction performance [115, 190], we consider the ultimate goal in fMRI analysis and use suitable metrics for the task. For different values of λ_s and ϵ in SparseICA-EBM, we use cost, time course power ratio and visual inspection to determine the suitable values. Our experimental results from real fMRI data show that when λ_s is too large, components are estimated repeatedly by SparseICA-EBM. Some important components, such as DMN and frontoparietal, are missed. Large ϵ appears to produce good performance, which is consistent with the results in [36]. For different values of λ in DL, time course power ratio and visual inspection are performed to determine its suitable value. The experimental results suggest that $\lambda = 10$ yields the best estimation. Even though different values of

sparsity parameters are selected, *i.e.*, $\lambda_s = 10^{-4}$ for SparseICA-EBM and $\lambda = 10$ for DL, the sparsity level imposed by them are similar. The Gini index is computed to measure the sparsity level of a source. It is a normalized quantity with 1 corresponding to very sparse sources while 0 to dense ones [92]. The results show that the distribution of Gini indices of all 85 components estimated from DL is close to that from SparseICA-EBM. The Kullback-Leibler divergence from the distribution of DL to that of SparseICA-EBM is estimated as 0.0393.

For ICA, the main parameter of choice is the signal subspace order that determines the total number of components to estimate. In this work, the model order is set as 85. Recently, many fMRI studies that use data-driven techniques such as ICA favor a higher model order, typically within the range [70, 100] since this yields a more detailed decomposition of the RSNs which are also more repeatable [2, 11, 62, 113]. Small orders such as those in the range [20, 40] are not favored in newer studies since they most often include overlapping or combined estimates of RSNs. However, model orders that are greater than 100 decrease the stability of ICA which is as expected in other data-driven techniques as well [2]. There are a number of methods for performing order selection in a data-driven manner, and ER-FM provides a desirable match to fMRI data characteristics as the span of sample correlation is modeled as finite in this model, and is what we have used in this analysis. Thus for parameter-free algorithms like Infomax and EBM, the fMRI analysis can be totally data driven, which might also explain the popularity ICA has enjoyed from the point of view of practitioners. For DL, one advantage that has been noted is that dimensionality reduction stage can be bypassed [3, 186], however our study using global metrics demonstrate that estimates tend to be noisy without dimensionality reduction regardless of the parameter values including dictionary size. Hence the observation of our experiment suggests that DL is not able to separate signal components from noise components effectively without

dimensionality reduction when applied to the COBRE data used in this article. Thus it is advisable to incorporate dimension reduction into DL as well either directly using PCA or by imposing low rank structure. Therefore, subject-level PCA with the same order as in ICA is performed before applying DL.

Component estimation From the comparison results using time course power ratio, network connection summary and graph-theoretical analysis, we can see that different algorithms stand out in different cases. This can be explained by the intrinsic variance of these decompositions which depend on dissimilar modeling assumptions.

DL provides better identification of the components that describe the BOLD response. As observed in Fig. 3.3(b), the power ratio mean and median of the components from DL are higher than those from the other algorithms, which illustrates that on average, DL has the capability to estimate components that are more likely to describe the BOLD response. Fig. 3.4 shows that the activated area in components that are estimated from Infomax, SparseICA-EBM and DL are very focal and localized. However, components, such as DMN and frontoparietal, that have multiple relevant regions are not completely estimated by these three algorithms. It is known that DMN contains multiple areas, the ventral anterior cingulate cortex (vACC), posterior cingulate cortex (PCC), left and right inferior parietal cortex (IPC). Usually, PCC is estimated together with the left and right IPC, and vACC is estimated in another individual component called anterior DMN. The DMN components from Infomax, SparseICA-EBM and DL are only activated in PCC. Similar observations are noted for frontoparietal network where ERBM yields a frontoparietal component with both the frontal and parietal region activated. Consequently, EBM and ERBM provide better estimation of functionally relevant components.

Fig. 3.5 shows the network connection summary of EBM and it illustrates that components from EBM can help to reconstruct a good functional connectivity of brain. The

reconstructed connection from EBM shows dense connectivity within functional networks and also demonstrates reasonable inter-connectivity among different functional networks. The close-packed connectivity within functional networks may provide valuable clues for the development of those automatic clustering algorithms for the estimated components.

Though DL provides better identification of the components that describe the BOLD response, it yields the lowest intra- and inter-module connectivity ratio R_m . To account for higher-order dependence, we use mutual information between pairwise spatial maps to measure connectivity. Time course power ratio is a metric for time course comparison, while R_m is used to summarize the spatial dependence. Therefore, there is no expectation of higher R_m for DL. This is also an evidence that it is to study higher-order dependence rather than only concentrating on second order dependence, *i.e.*, correlation.

In the event that one is analyzing data from two groups and seeking to find group differences, ERBM appears to be more preferable as ERBM can produce components with more relevant regions activated thus leading to more effective discrimination in a graph-theoretical analysis. From the graph-theoretical analysis results shown in Fig. 3.6, ERBM estimates more components that show significant group difference when using globally calculated nodal graph metrics, such as degree, path length, global efficiency and centrality. Usually, dysconnectivity is observed for individuals with SZ [38, 173]. Therefore, higher variance is expected in connectivity analysis for patients compared to HCs. In Fig. 3.7, ERBM demonstrates improved ability to capture the contrast of the variability of SZs and HCs using the global graph metrics, clustering coefficient and SW. We also note that there is no scenario where widely-used Infomax algorithm provides the best performance, demonstrating the cost of exploiting fewer forms of diversity. This suggests that different algorithms can be chosen for different purposes.

3.4 Summary

In this chapter, we conducted a comparative study to investigate the performance of different BSS algorithms when applied to multi-subject fMRI data. For this task, we chose Infomax, EBM, ERBM, online DL and SparseICA-EBM as they are good representative set of algorithms that make use of different types of diversity. We proposed the use of global metrics to assess the performance of data-driven algorithms, namely, time course spectra power ratio, network connection summary and graph-theoretical metrics. With the use of time course spectra power ratio, DL yielded components that are most likely to describe the BOLD response. By using network connection summary, EBM illustrated a better ability to reconstruct the brain connectivity with normalized mutual information as the measure. When graph-theoretical analysis is applied, ERBM demonstrated a better capability to capture the group differences between SZs and HCs, especially the higher variance in SZs as expected.

Our results suggested that no one particular method had the best performance using all metrics, implying that the optimal method will change depending on the goal of the analysis. In general, exploiting more forms of diversity yields better performance. Additionally, we should note that there is no scenario where the widely used Infomax has shown the best performance, which demonstrates that incorporating multiple types of diversity is more desirable. This successful application motivates the use of additional global metrics to assess the performance for unbiased algorithmic comparison on real fMRI data analysis, or even on other real data analysis such as electroencephalograph data.

Chapter 4

IVA FOR SUBSPACE ANALYSIS OF MULTI-SUBJECT FMRI DATA

The extraction of common and distinct biomedical signatures among different populations allows for a more detailed study of the common, group-specific as well as distinct information across populations. A number of subspace analysis algorithms have been developed and successfully applied to data fusion, however they are limited to joint analysis of only a couple of datasets. Since subspace analysis is very promising for analysis of multi-subject medical imaging data as well, we focus on this problem and propose a new method IVA-CS for multi-subject data analysis. IVA-CS leverages the strength of IVA in identification of a complete subspace structure across multiple datasets along with an efficient solution that uses only SOS. We propose a subset analysis approach within IVA-CS to mitigate issues in estimation in IVA due to high dimensionality, both in terms of the number of components and datasets. We introduce a scheme to determine a desirable size for the subset that is high enough to exploit the dependence across datasets and is not affected by the high dimensionality issue. We demonstrate the success of IVA-CS in extracting complex subset structures and apply the method to analysis of multi-subject fMRI data. More importantly, IVA-CS helps identify subgroups of SZs that show significant differences in terms of their brain networks and clinical symptoms.

4.1 Introduction

The study of multi-subject fMRI data using data-driven techniques is prevalent in the neuroimaging field with a goal to identify differences in the brain function of different populations such as the SZ and HC groups [1, 87, 141, 156, 170]. Identification of common and distinct subspaces from multiple datasets transforms the high dimensional datasets into lower dimensional joint and disjoint subspaces, and allows for a more detailed analysis of the common, group-specific as well as distinct information. In these models, the assumption is that each observed dataset is explained by a sum of linearly mixed latent variable models. The common subspace is defined as a subset of latent variables that are highly correlated across the given datasets. The distinct subspace is a subset of latent variables that have very low correlation to each other. The joint subspaces bring the datasets to a common ground, thus allowing for a fair and reliable comparison among different population groups. Meanwhile the distinct components can be used to study individual differences such as the unique connection pattern of a patient with a mental disease.

Clinical heterogeneity of patients with mental disorders, especially in SZ has been recognized [69, 101, 102], and there has been significant interest in studying their subtypes [82, 89, 150]. The study of subtypes can be made possible by identifying subgroups of patients that share specific common information and can help better understand the uncertainty in the need of precision medicine [167] during clinical diagnosis and treatment. Subtypes of SZ have been well studied using genetic information [89, 150] but not yet using other neuroimaging modalities such as fMRI data, which has been successfully used in the study of SZ [45, 82, 140]. The common subspace analysis motivates us to find a way to identify subgroups of patients with potential subtypes of SZ by summarizing their shared information. Therefore, along with identifying a common subspace comprised of components correlated across all subjects, the extraction of common components across a

subgroup of subjects is also of interest.

Given the importance of common and distinct subspace analysis in medical image analysis, a number of recent studies had a focus on this aspect, in particular for fusion of different modalities such as fMRI, structural MRI and electroencephalograph, or of fMRI data from different tasks [5, 65, 114, 126, 135, 161, 176, 184]. However these cases have only been demonstrated for joint decomposition of a small number of datasets. As we have discussed, distinct and common subspace analysis also promises to be attractive for multi-subject analyses. The models used for identification of common and distinct subspaces in fusion study have not been well-studied in the context of the joint analysis of more than a couple of datasets. Multi-subject data analysis involves joint analysis of at least tens, or more typically hundreds of subjects. A recently proposed method Shared and Subject-Specific Dictionary Learning (ShSSDL) [97] targets multi-subject task fMRI analysis and identifies shared components across subjects as well as subject-specific components. However, ShSSDL assumes common time courses across datasets and is not able to identify components that are common across subgroups of subjects. Another ICA-based algorithm, hierarchical ICA [86], simultaneously estimates the population-level and subject-specific sources. However, the complexity of the density model used in hierarchical ICA grows when the number of datasets increases and it does not account for the dependence structure of these sources.

In this chapter, we propose a new method IVA-CS to extract subspaces from large-scale datasets and demonstrate its successful application to the analysis of fMRI data collected from 179 subjects. We first use simulation studies to investigate the strengths and challenges of IVA when applied to multi-subject fMRI data analysis. The proposed IVA-CS method takes advantage of the strengths and addresses the challenge of IVA. We show that IVA-CS using IVA-G (IVA-G-CS) that takes only SOS into consideration is powerful

in discovering the subspace structure and estimating the subspaces through a careful study of the correlation structure of SCVs. We also demonstrate that IVA-CS enables the study of the heterogeneity of mental disease such as SZ by identifying subgroups of subjects with potential subtypes of SZ.

4.2 Strengths and challenges of IVA

IVA has been successfully used for multi-subject fMRI data to effectively capture subject variability hence preserving subspace structure which provides a good starting point for subspace analysis [119, 148]. We investigate the strengths and challenges of IVA in this section to take advantage of the strengths for subspace analysis and address the challenges.

4.2.1 Identification condition for IVA

Identification condition of IVA is studied by analyzing the Fisher information matrix of the objective function (2.9) with respect to the demixing matrices \mathbf{W} [4, 16]. Compared with the identification condition of ICA that is associated with two individual sources, the identification condition of IVA is introduced for two SCVs. It is shown that the identification condition of IVA depends on the SOS of subsets of sources in an SCV. If the SOS defined through covariance matrices provide the required diversity across SCVs, the SCVs are separable even when they are multivariate Gaussian distributed since their SOS can be accurately captured by any type of multivariate distribution prior. We define an α -SCV as an SCV with a particular subset of source components that are K_α -dimensional multivariate distributed and independent from the complementing subset in the same SCV. Note that all sources are assumed to have unit variance and zero mean for simplicity. Let $\alpha \in \mathbb{N}^{K_\alpha}$ be a subset of source indices within an SCV, where $0 \leq K_\alpha \leq K$. The complementing subset of α in $1, 2, \dots, K$ is denoted as $\alpha^c \in \mathbb{N}^{K-K_\alpha}$. In two arbitrary α -SCVs, the subsets of sources, $\mathbf{S}_{n,\alpha} \in \mathbb{R}^{K_\alpha \times V}$ and $\mathbf{S}_{m,\alpha} \in \mathbb{R}^{K_\alpha \times V}$, cannot be identified if and only if there exists a full rank

diagonal matrix $\mathbf{D} \in \mathbb{R}^{K_\alpha \times K_\alpha}$ such that

$$\mathbf{R}_{m,\alpha} = \mathbf{D}\mathbf{R}_{n,\alpha}\mathbf{D}, \quad (4.1)$$

where $\mathbf{R}_{n,\alpha} \triangleq \mathbb{E}\{\mathbf{S}_{n,\alpha}\mathbf{S}_{n,\alpha}^T\} \in \mathbb{R}^{K_\alpha \times K_\alpha}$ refers to the correlation matrix of the subset of sources [16]. This suggests that the correlation matrices of the subsets of sources in two unseparable α -SCVs have the same structure but different scaling. If an IVA algorithm only takes SOS into consideration, any subset of sources within an SCV that possess this property will not be separated into individual ones. An example of two unseparable α -SCVs is shown in Fig. 2.3. The change in value of K_α indicates that two SCVs can be unseparable either in whole or in subsets of components. However, this is no longer a problem when other types of diversity, such as HOS and sample dependence, of the data are taken into consideration.

MCCA is another data-driven algorithm for the joint analysis of multiple datasets which is based on SOS only and achieves the decomposition in a deflationary manner. MCCA-GENVAR is shown to have equivalent cost function with IVA-G. The identification condition for MCCA is given by pairwise correlation values

$$\forall k, l \in \{1, 2, \dots, K\}, |r_{k,l}^{[m]}| \neq |r_{k,l}^{[n]}|, 1 \leq m < n \leq N, \quad (4.2)$$

where $r_{k,l}^{[n]}$ is the element of \mathbf{R}_n [133]. Hence MCCA cannot preserve the structure of SCVs. In contrast, IVA-G has a more general identification condition given in (4.1) that is synchronized for all SCVs, which enables one to discover subspace structures as we demonstrate by simulation results in next section.

Simulation study To study the ability of IVA to maintain the structure of SCVs to effectively identify the subspaces, we design a set of simulations. Our application is fMRI data analysis and the latent fMRI sources are likely to be super-Gaussian distributed [44]. Therefore, all the SCVs are generated from an MGGD with the shape parameter β

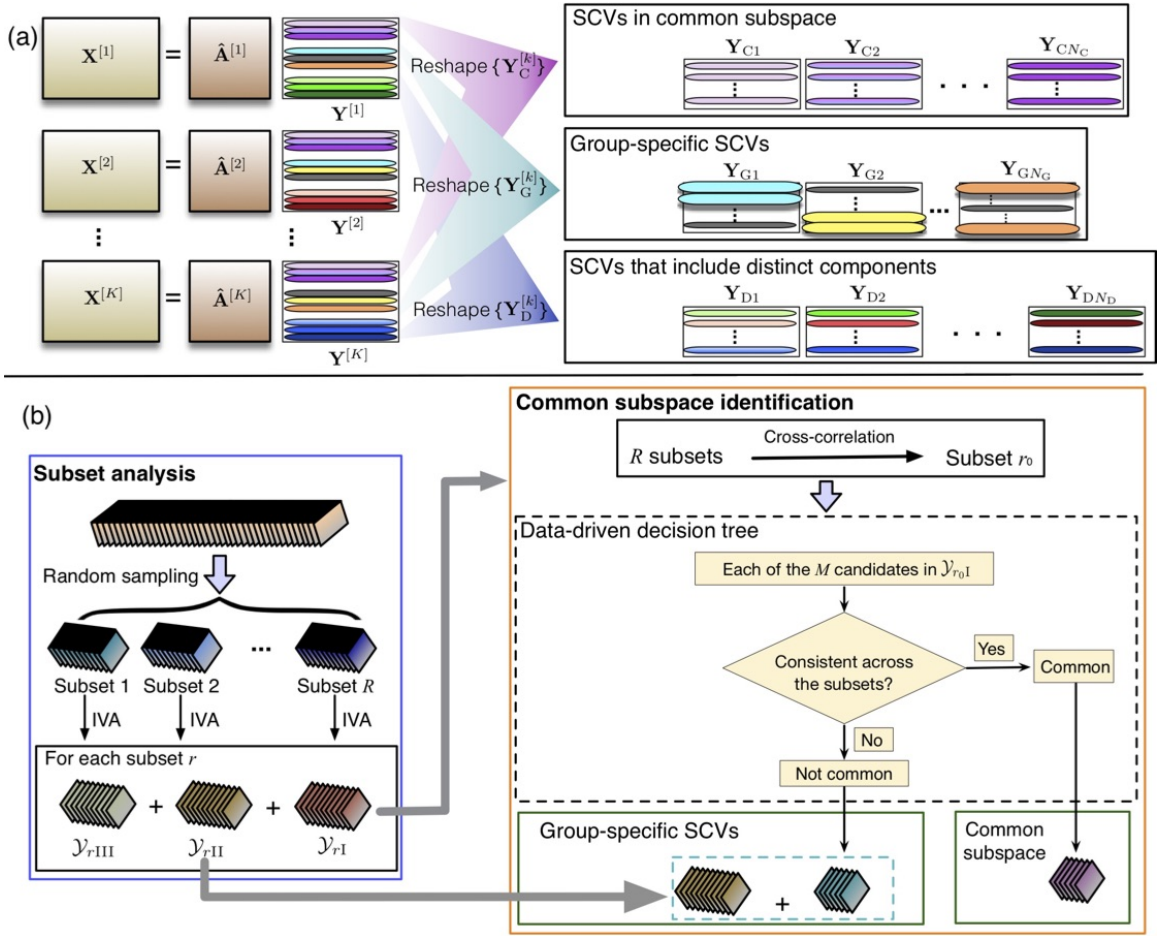


FIG. 4.1. The definition of common subspace and other two sets of SCVs in signal space (a) and the subset analysis and common subspace identification of IVA-CS (b). The number of SCVs in each of the three sets in (a) are denoted by N_C , N_G and N_D separately.

randomly selected from the interval $[0.1, 0.8]$, which generates super-Gaussian marginals. The SCVs are mixed by randomly generated mixing matrices, $\mathbf{A}^{[k]}$, from a standard uniform distribution to form the datasets using (2.7). A total of $N = 30$ SCVs are generated with $V = 10000$ voxels and $K = 20$ datasets. Note that all the MGGD sources are normalized to zero mean and unit variance hence the covariance values and correlation (coefficients) coincide. These SCVs are grouped to imitate three subspaces and the details are as follows:

- The first group of 14 SCVs are simulated as common sources with high correlation

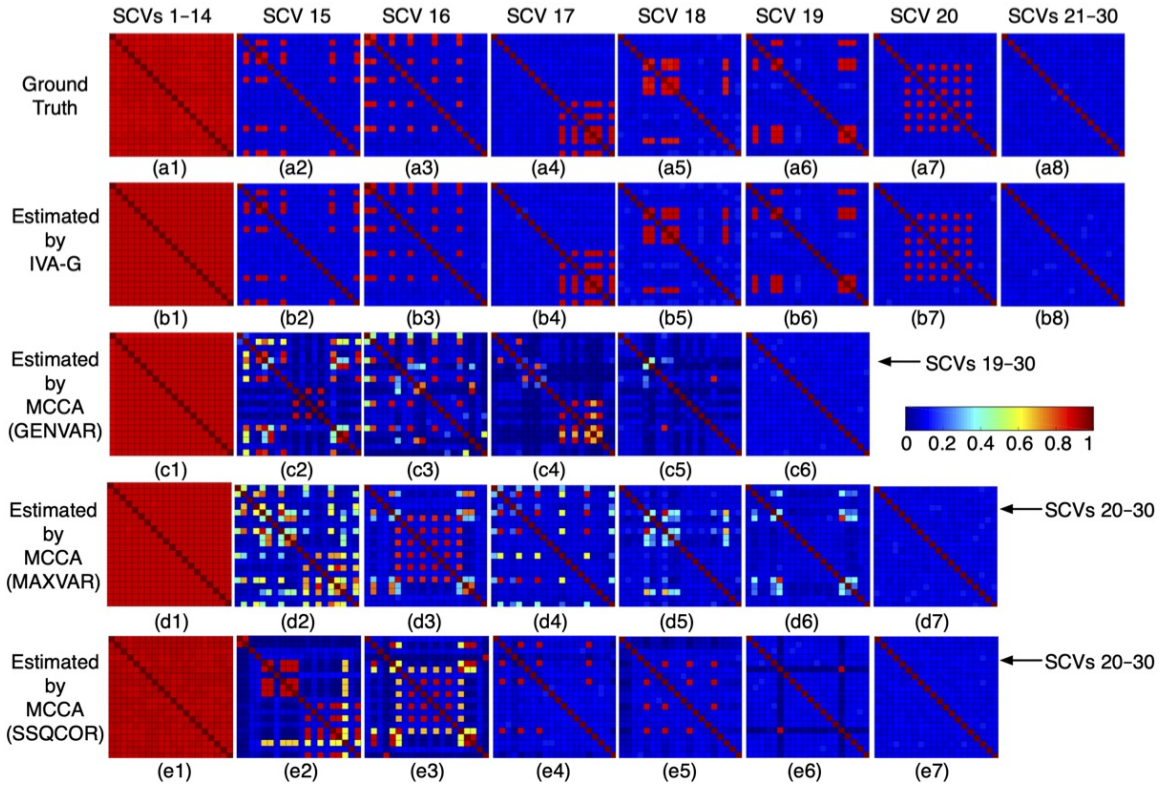


FIG. 4.2. Correlation matrices of true SCVs (a), the estimated ones from IVA-G (b), MCCA-GENVAR (c), MCCA-MAXVAR (d), and MCCA-SSQCOR (e) in simulation.

value ρ_c . The correlation matrix of a common SCV is shown in Fig. 4.2(a1).

- The second group of 6 SCVs have structured correlation matrices with some higher value of ρ_c and some lower value of ρ_d . This indicates that the sources with higher correlation values are common within a subgroup of datasets. The structured correlation matrices are shown in Fig. 4.2(a2)–(a7).
- The last group of 10 SCVs are simulated as distinct sources with low correlation value ρ_d . Fig. 4.2(a8) shows the correlation matrix of a distinct SCV.

Different cases are studied in the simulation with different values of ρ_c and ρ_d : Case 1, $\rho_c = 0.9, \rho_d = 0.1$, Case 2, $\rho_c = 0.8, \rho_d = 0.2$, Case 3, $\rho_c = 0.7, \rho_d = 0.3$, and Case 4, $\rho_c = 0.6, \rho_d = 0.4$.

Fig. 4.2 shows the correlation matrices of the true SCVs and the estimated SCVs for a random run for Case 1. To demonstrate that IVA identification condition enables preserving the structure of SCVs compared to MCCA due to its identification condition, we perform IVA-G and three versions of MCCA, *i.e.*, MCCA-GENVAR, MCCA with MAXVAR cost function (MCCA-MAXVAR), and MCCA with SSQCOR cost function (MCCA-SSQCOR), on the mixtures of sources, \mathbf{X} . MCCA-MAXVAR and MCCA-SSQCOR behave similar to MCCA-GENVAR and Fig. 4.2 shows the results of IVA-G and the three MCCA algorithms. Both IVA-G and MCCA-GENVAR successfully extract the common subspace spanned by SCVs 1–14. But for the SCVs 15–20, as we can see there are only a subset of components highly correlated with each other. It is possible for some components in one SCV to have a certain level of correlation with the components in another SCV. MCCA-GENVAR estimates one SCV by maximizing the correlation among the sources across datasets. MCCA tends to group as many correlated sources as possible in the SCVs that are estimated first, due to its deflationary nature. Hence we observe some SCVs that are merged together, as shown in Fig. 4.2(c2)–(c5), and that the SCV15 and SCV16 contain more correlated sources than SCV17 and SCV18. This breaks the structure of true SCVs and makes it impossible to identify the subgroups of sources within an SCV, *i.e.*, to identify subspaces. As a result, MCCA yields fewer SCVs with structured correlation matrix and more distinct SCVs compared with the ground truth. In contrast, IVA-G successfully preserves the structure of all SCVs. Note that these SCVs are estimated subject to permutation ambiguity due to the nature of all BSS algorithms. This illustrates the desirable use of IVA-G to extract subspaces to identify subgroups.

IVA-G and IVA-L-SOS Identification condition of IVA-G implies that IVA-G is not able to separate α -SCVs that have proportional correlation matrices no matter which distribution the latent sources are drawn from. The unseparable sources can be the whole

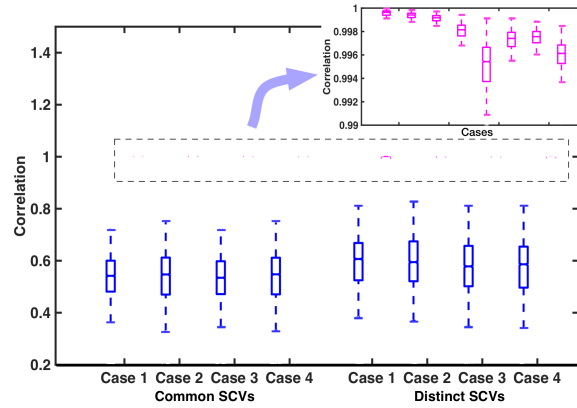


FIG. 4.3. Boxplots of the correlation values between the estimates and the ground truth for IVA-G in blue and IVA-L-SOS in magenta for the four cases. Statistics are calculated from 100 independent runs with different initialization. The box plot displays the median, the 25th and 75th percentiles of the correlation values with whiskers extending to the 99.3% confidence interval using the default settings.

SCVs or a subset of sources in the SCVs since $0 \leq K_\alpha \leq K$. In our simulation SCVs 1–14 have the same correlation matrix hence IVA-G identifies the whole subspace successfully while not the individual SCVs. The same situation for SCVs 21–30. As noted in Chapter 4.2.1, an IVA algorithm that takes both SOS and HOS into consideration like IVA-L-SOS can solve this problem. We can either perform IVA-L-SOS on the original datasets or perform a secondary IVA-L-SOS decomposition on the subspace identified by IVA-G. Reliably identifying subspaces of interest by IVA-G followed by a secondary decomposition of an IVA algorithm that takes both SOS and HOS (and hence is computationally more complex) into consideration on the subspaces helps save considerable computation time. This two-step procedure guarantees better performance by first identifying a desirable starting point. This strategy is favorable in the applications of BSS problems and is the core in the common practice of performing PCA first to provide an orthogonal initialization for an ICA decomposition.

The correlation between the estimates and the ground truth is calculated to evaluate the performance. IVA-G yields good estimation of SCV15-20 and their average correlation

is 0.996 ± 0.014 across all four cases. To explore the ability of IVA-L-SOS to separate α -SCVs with proportional correlation matrices, a secondary IVA-L-SOS decomposition is performed on the common and distinct subspace separately. The common and distinct subspaces are constructed separately by multiplying the common and distinct SCVs from IVA-G with their associated mixing matrices calculated as the inverse of the estimated demixing matrices. Fig. 4.3 shows that IVA-G yields common components that are not highly correlated with the ground truth. However, these components are very reliably estimated by the secondary IVA-L-SOS with correlation values close to 1. This verifies that the identification issue of IVA is not a problem anymore when HOS is taken into consideration.

4.2.2 Dimensionality issue of IVA

The curse of dimensionality of IVA notes that the performance of IVA degrades with increase in the number of sources and datasets for a fixed number of samples. Hence for a high model order and relatively large number of datasets, IVA requires a proportionally large number of data samples for efficient estimation of the demixing matrices. However, the number of samples is fixed in many real-world applications such as fMRI data analysis since the resolution of the data is predetermined. On the other hand, the dependent information across datasets is not sufficient for IVA to exploit in the case with a relatively small number of datasets.

To achieve a reliable IVA decomposition, we need sufficient number of samples per estimated parameter so that IVA can effectively take dataset dependence into account. The performance of IVA degrades as the number of datasets, K , or the number of sources, N , increases beyond a certain point, when number of samples, V , is fixed. The estimation of the source covariance matrix that determines the multivariate Gaussian distribution of each SCV is required in IVA-G for each update of demixing matrices \mathbf{W} , which in turn is used to estimate the SCVs. The total number of samples in a dataset is $NV \times K$. The number of free

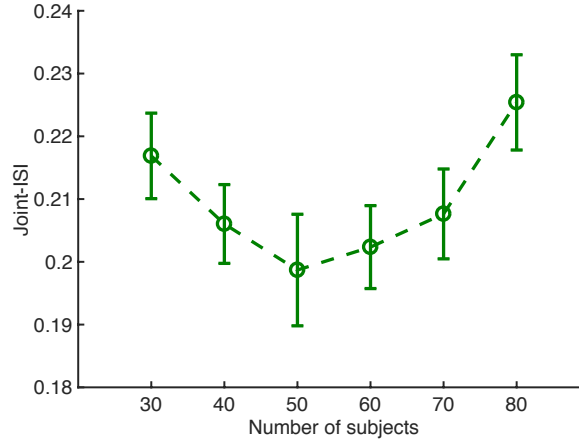


FIG. 4.4. Plot of joint-ISI as a function of the number of subjects when performing IVA-G on the hybrid data. The mean and standard deviation calculated from the results of 20 runs are shown.

parameters to be estimated in the covariance matrix for each of K SCVs is $\frac{K(K-1)}{2}$. Hence the number of samples per free parameter is $\frac{NV \times K}{N \times \frac{K(K-1)}{2}} = \frac{2V}{K-1}$, which is inversely proportional to K . When updating the demixing matrices \mathbf{W}_k , there are KN^2 free parameters hence the number of samples per free parameter is $\frac{NV \times K}{KN^2} = \frac{V}{N}$, which is inversely proportional to N . To explore the optimal value of K that balances the effect of high dimensionality and maximal subject information when the N is fixed—*i.e.*, determined using a data-driven approach—we design a hybrid simulation. The estimated 85 COBRE sources as presented in our previous study [137] are used as the sources and mixed by the randomly generated mixing matrices to produce the hybrid data. With a fixed model order and a fixed number of voxels, the number of subjects K is changed from 30 to 80 with increments of 10. The performance is measured by joint-ISI which is defined as

$$\text{ISI}_{\text{JNT}}(\mathbf{G}^{[1]}, \mathbf{G}^{[2]}, \dots, \mathbf{G}^{[K]}) \triangleq \text{ISI} \left(\frac{1}{K} \sum_{k=1}^K |\mathbf{G}^{[k]}| \right), \quad (4.3)$$

where

$$\begin{aligned} \text{ISI}(\mathbf{G}) &= \frac{1}{2N(N-1)} \cdot \sum_{n=1}^N \left(\frac{\sum_{m=1}^N \|g_{nm}\|}{\max_p \|g_{np}\|} - 1 \right) \\ &+ \frac{1}{2N(N-1)} \cdot \sum_{m=1}^N \left(\frac{\sum_{n=1}^N \|g_{nm}\|}{\max_p \|g_{pm}\|} - 1 \right) \end{aligned} \quad (4.4)$$

and $\mathbf{G}^{[k]} = \mathbf{W}^{[k]} \mathbf{A}^{[k]}$ with elements denoted as g_{nm} [13]. $\mathbf{A}^{[k]}$ is the true mixing matrix and $\mathbf{W}^{[k]}$ is the estimated demixing matrix. If $\mathbf{W}^{[k]}$ is perfectly estimated, $\mathbf{G}^{[k]}$ is identity subject to permutation and scaling ambiguities, thus yielding zero ISI that indicates a perfect separation. Therefore, the smaller the joint-ISI, the closer the estimates are to the ground truth.

From Fig. 4.4 we see that the performance of IVA-G improves with increase in the number of datasets until a certain value of K , after which the performance degrades. This illustrates that when the number of datasets used in an IVA decomposition is too small, the interaction information across datasets is not sufficient for an accurate estimation of the sources. Hence the performance improves with more number of datasets. However, for a larger number of datasets, IVA suffers from the curse of dimensionality. Thus, the performance degrades. The experimental results show that there indeed exists an optimal value of the number of datasets for an IVA decomposition that balances the requirement of interaction information and the dimensionality issue. The optimal number of subjects in this application is determined as $K = 50$, where IVA yields the best performance, *i.e.*, the lowest joint-ISI as shown in Fig. 4.4. This value is then used as the subset size in subset analysis of IVA-G-CS. We randomly selected five subsets of subjects for each group to ensure that each subject is included at least once in the decompositions. Note that in this work the values of all dimension parameters are determined in a data-driven manner.

4.3 IVA for common subspace analysis

Common and distinct subspace analysis has proven useful in identifying distinct biomedical signatures of different populations in order to better understand the unique features of different brain disorders. Most subspace analysis algorithms introduced to date that have shown superior performance are designed specially for fusion study where only a few datasets are analyzed [5, 114, 135, 161, 176, 184]. However, these models become extraordinarily complex as the data size increases to tens or even hundreds of datasets. Most medical imaging data like fMRI data is collected from tens or hundreds of subjects and a joint analysis of the multiset data enables one to leverage its rich information especially across the datasets. This motivates the exploration of an algorithm which can identify common and distinct subspaces from relatively large-scale datasets.

We assume that the source space of the observed data consists of three sets of SCVs. The first set of SCVs, $\{\mathbf{Y}_{Cn} = [\mathbf{y}_{Cn}^{[1]}, \dots, \mathbf{y}_{Cn}^{[K]}]^T\}$, $1 \leq n \leq N_C$, define the common subspace where the sources within each SCV are highly correlated (across all datasets) and the third set of SCVs, $\{\mathbf{Y}_{Dn} = [\mathbf{y}_{Dn}^{[1]}, \dots, \mathbf{y}_{Dn}^{[K]}]^T\}$, $1 \leq n \leq N_D$, consist of low correlated sources (correlation values less than σ_t^2) as shown in Fig. 4.1(a). Another set of group-specific SCVs, $\{\mathbf{Y}_{Gn} = [\mathbf{y}_{Gn}^{[1]}, \dots, \mathbf{y}_{Gn}^{[K]}]^T\}$, $1 \leq n \leq N_G$, can be used to determine subgroups of subjects that have more highly correlated RSNs in an unsupervised manner. Therefore, the observed dataset for the k th subject is a mixture of three types of sources:

$$\begin{aligned}
 \mathbf{X}^{[k]} &= \hat{\mathbf{A}}^{[k]} \mathbf{Y}^{[k]} \\
 &= \hat{\mathbf{A}}_C^{[k]} \mathbf{Y}_C^{[k]} + \hat{\mathbf{A}}_G^{[k]} \mathbf{Y}_G^{[k]} + \hat{\mathbf{A}}_D^{[k]} \mathbf{Y}_D^{[k]} \\
 &= [\hat{\mathbf{A}}_C^{[k]} \quad \hat{\mathbf{A}}_G^{[k]} \quad \hat{\mathbf{A}}_D^{[k]}] \begin{bmatrix} \mathbf{Y}_C^{[k]} \\ \mathbf{Y}_G^{[k]} \\ \mathbf{Y}_D^{[k]} \end{bmatrix}, \quad k = 1, 2, \dots, K,
 \end{aligned} \tag{4.5}$$

where $\hat{\mathbf{A}}_C^{[k]}$, $\hat{\mathbf{A}}_G^{[k]}$, and $\hat{\mathbf{A}}_D^{[k]}$ are corresponding estimated mixing matrices of the common sources $\mathbf{Y}_C^{[k]} = [\mathbf{y}_{C1}^{[k]}, \dots, \mathbf{y}_{CN_C}^{[k]}]^T$, the sources $\mathbf{Y}_G^{[k]} = [\mathbf{y}_{G1}^{[k]}, \dots, \mathbf{y}_{GN_G}^{[k]}]^T$ that compose the group-specific SCVs, and the distinct sources $\mathbf{Y}_D^{[k]} = [\mathbf{y}_{D1}^{[k]}, \dots, \mathbf{y}_{DN_D}^{[k]}]^T$, respectively.

We propose a new method called IVA-CS that is able to extract subspaces from at least couple of hundreds of datasets. IVA-CS leverages the strength of IVA that its identification condition enables successful preservation of the SCV structure, which makes it highly effective for subspace analysis. However, IVA suffers from the curse of dimensionality when applied to real-world applications with a high number, *e.g.*, hundreds, of datasets such as in multi-subject fMRI data analysis. In this scenario since the number of samples (voxels) is fixed, as the number of datasets and the number of sources increases, it does not guarantee an accurate estimation of the demixing matrices \mathcal{W} and calculation of SCV correlation matrices any more. Therefore, our IVA-CS method is composed of two stages, (i) subset analysis and (ii) common subspace identification. The subset analysis stage overcomes the challenge of dimensionality issue by first performing multiple individual IVA decompositions on subsets of subjects that are randomly sampled from the population. The exploration of subset size, K , is introduced in detail in Chapter 4.2.2. The common subspace identification stage determines a consistent common subspace for the whole population as well as a set of the group-specific SCVs. The details of IVA-CS method are given next.

4.3.1 IVA-CS: Subset analysis

The flowchart of IVA-CS is shown in Fig. 4.1(b). In subset analysis, R subsets of K subjects are randomly selected from all subjects of a group. IVA is performed on each subset yielding N SCVs. We define the whole signal space as \mathcal{Y} that includes all N estimated sources, where $\mathbf{y}_n^{[k]}$ denotes the n th source of the k th dataset. For each subset, its signal space is denoted as \mathcal{Y}_r , $1 \leq r \leq R$. Note that all source components are normalized to have

unit variance and zero mean hence their covariance values and correlation values coincide. For each SCV we compute a $K \times K$ correlation matrix with $K \times (K - 1) / 2$ distinct correlation values. Using these correlation values, we can study how close these components are to each other and determine whether the corresponding source component is common across all the datasets or not. For an SCV corresponding to the common component, we expect that all the correlation values are significantly high. We measure the ‘‘commonality’’ of an SCV by computing the ratio of the number of correlation values that are greater than σ_t^2 , an empirically determined threshold, to the total number of correlation values for each SCV as follows,

$$q = \frac{N_{\sigma_t^2}}{K(K - 1) / 2}, \quad (4.6)$$

where $N_{\sigma_t^2}$ denotes the number of correlation values that are greater than σ_t^2 in the correlation matrix of an SCV. An SCV corresponding to a common component is expected to have high commonality hence the value of q is close to 1. Another relevant metric is ‘‘dissimilarity’’ which is defined as the ratio of the number of low correlation values to the number of high correlation values

$$\tilde{q} = \frac{K(K - 1) / 2 - N_{\sigma_t^2}}{N_{\sigma_t^2}}. \quad (4.7)$$

The dissimilarity, the value of \tilde{q} , for a common SCV is expected to be close to 0.

For each subset $r, r = 1, \dots, R$, N SCVs are sorted in descending order by the mean value of the correlation, which roughly arranges the SCVs from those with high source correlation to those with low source correlation. The number of common SCVs in each subset, M_r , is determined as the largest number that allows for most of the first M_r SCVs having $q \geq \delta_1$ and $\tilde{q} \leq \delta_2$. Here not all the M_r SCVs are required to satisfy the criteria, seeking to allow flexibility for a further examination of the commonness of these components. After determining the first subspace \mathcal{Y}_{r1} that is spanned by the M_r common SCVs for each subset, P percent of the remaining SCVs that have a mix of both high and low correlation values

forms the second subspace $\mathcal{Y}_{r\text{II}}$. The other SCVs form the third subspace $\mathcal{Y}_{r\text{III}}$, which is the distinct subspace.

4.3.2 IVA-CS: Common subspace identification

The second stage, common subspace identification has the goal to find a consistent common subspace \mathcal{Y}_C for all subjects of a group. To enable a comprehensive comparison across R subsets, we adjust the number of components in the subspace $\mathcal{Y}_{r\text{I}}$ to be common as M across all subsets. The M SCVs are candidates for the common subspace identification. The value of M is determined as the largest value of M_r , seeking to select as many candidates as possible. The mean component, \mathbf{y}_{mr} , $m = 1, \dots, M$, $r = 1, \dots, R$, is calculated by averaging the K components in the m th SCV for each subset r . The cross-correlation of each mean component is defined as the average correlation with its corresponding components in the other $R - 1$ subsets:

$$\rho_{mr} = \frac{1}{R-1} \sum_{l \neq r} |\rho_{mrl}|, \quad (4.8)$$

where ρ_{mrl} , $1 \leq l \leq R$, $l \neq r$ is the Pearson correlation coefficient between the mean components \mathbf{y}_{mr} and \mathbf{y}_{ml} . For each subset, its cross-correlation is defined as the average cross-correlation of its M mean components

$$\rho_r = \frac{1}{M} \sum_m \rho_{mr}. \quad (4.9)$$

The subset r_0 with the most consistent components is selected as the one with the largest cross-correlation ρ_r and is used to identify the common subspace for all the subjects. The identified common components should be not only common across the subjects within subset r_0 but also consistent across all subsets. To achieve this goal, we use a data-driven decision tree to determine whether a component is common or not as shown in Fig. 4.1(b). A threshold t is determined from the $M(R - 1)$ cross-correlation values. For each candi-

date, if more than a given percentage of its cross-correlation values are higher than t , it is determined to be a common component. First, the determined common component comes from the first subspace of subset r_0 which means it is common across all the subjects within subset r_0 . Second, this decision tree ensures that this component is correlated with its corresponding components from most of all the subsets hence it is consistent across subsets. The identified common subspace of all subjects therefore consists of all the determined common components. The components that are filtered out as not common are merged with subspace \mathcal{Y}_{II} to form a new set of SCVs to identify subgroups of datasets that have more highly interfered components through an unsupervised analysis.

4.4 Experimental results

We apply IVA-G-CS with a block Newton update that provides desirable convergence properties [14] to the resting COBRE data and show that IVA-CS extracts interpretable common RSN components for the SZ and HC groups separately.

4.4.1 Common subspace identification using IVA-G-CS

IVA-G-CS is applied to SZ group and HC group separately to identify their subspaces. Five subsets of 50 subjects are randomly selected for each group and 85 SCVs are estimated from each subset. The value at each voxel of the estimated source is transformed into Z-scores before any calculation of metrics hence the covariance and correlation coincide. For each SCV, there are $50 \times (50 - 1)/2 = 1225$ distinct correlation values. The smoothed distribution of correlation values is plotted as a function of the index of SCVs for the five subset of SZs and the five subsets of HCs as shown in Fig. 4.5–4.8. The similar plots of the other subsets are provided as supplementary materials. The SCVs are sorted by the mean value of correlation to roughly order them from high correlation to low correlation. From Fig. 4.6(e), the plot for the fifth subset of SZs, we can see there is a group of SCVs with

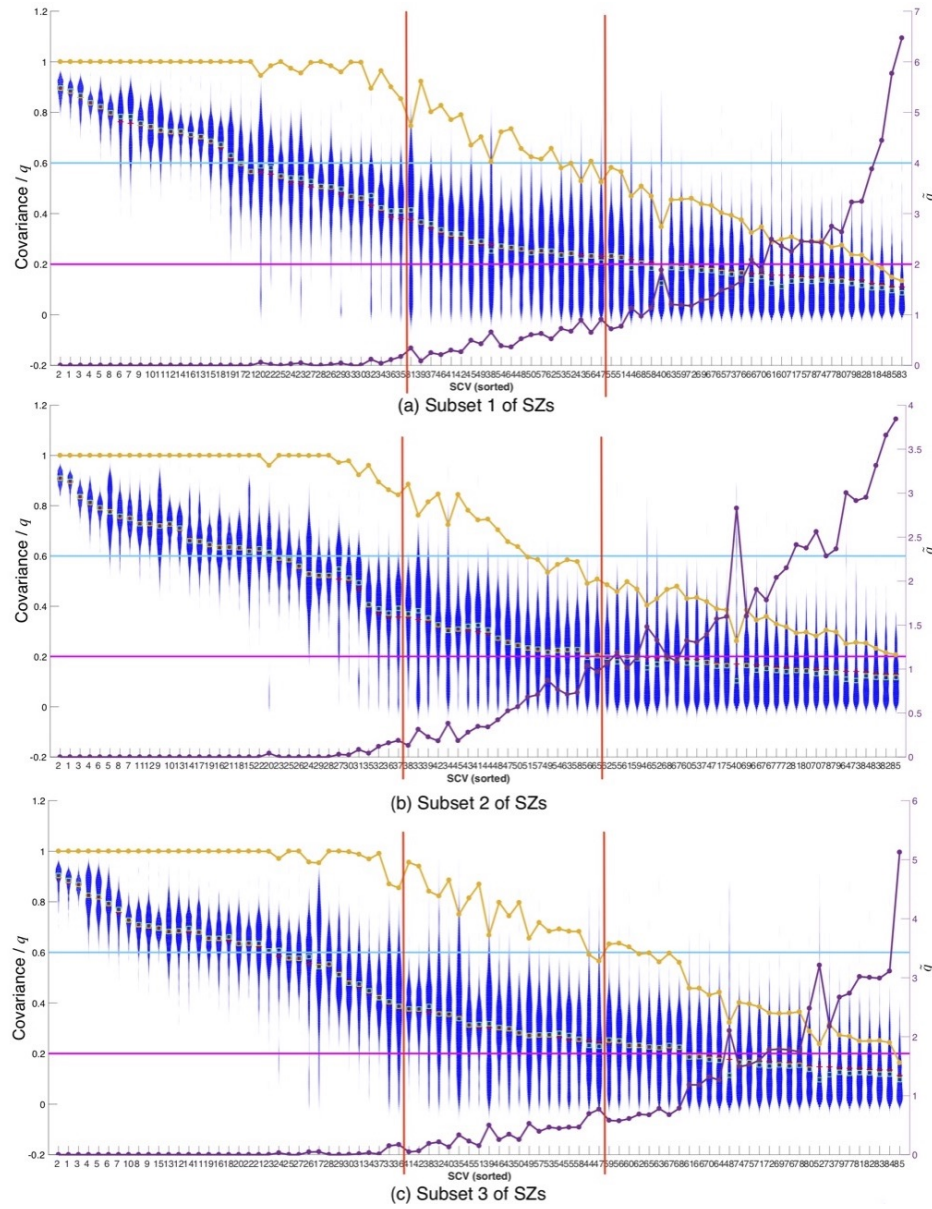


FIG. 4.5. (Part 1) Smoothed distribution of the correlation values of the five subsets of SZ group. The red crosses and the green squares denote the mean and median. Two ratios q and \tilde{q} are plotted in yellow and purple. Two vertical red lines denotes the margins between different groups of SCVs. Blue and magenta horizontal lines denotes 0.6 and 0.2 which are used for a comparison of the three groups of SCVs.

all their correlation values higher than 0.2. Using $\sigma_t^2 = 0.2$, the commonality q and dissimilarity \tilde{q} are calculated and plotted in yellow and purple, respectively. In the application

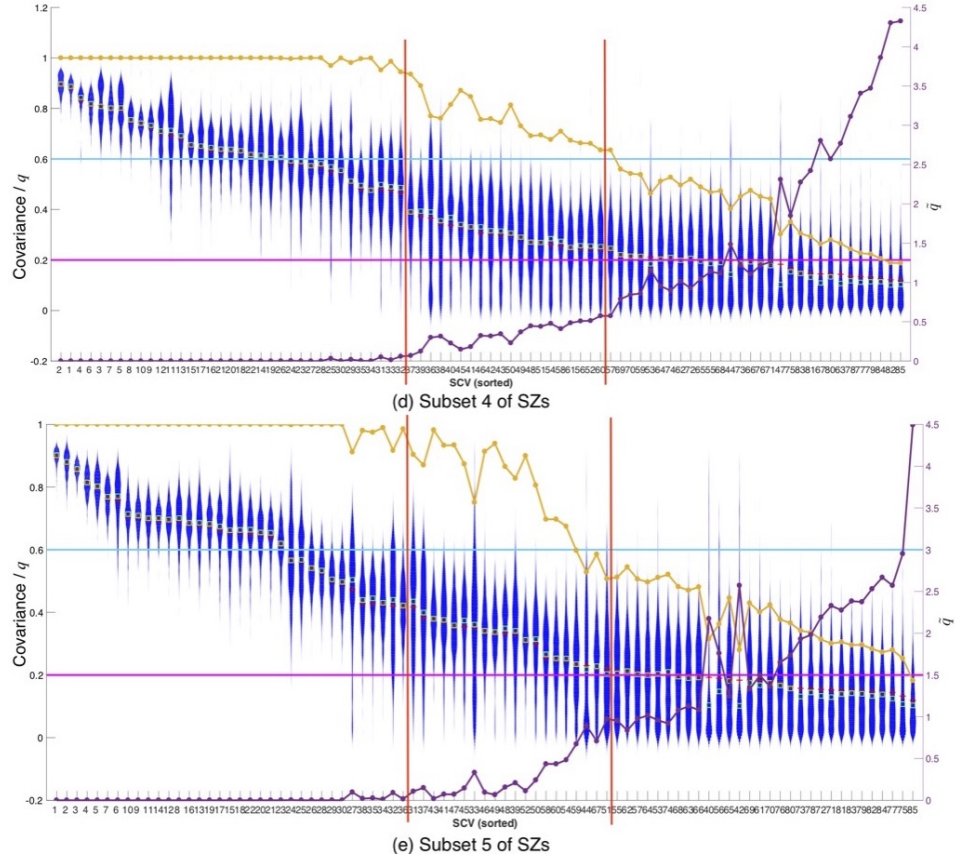


FIG. 4.6. (Part 2) Smoothed distribution of the correlation values of the five subsets of SZ group. The red crosses and the green squares denote the mean and median. Two ratios q and \tilde{q} are plotted in yellow and purple. Two vertical red lines denotes the margins between different groups of SCVs. Blue and magenta horizontal lines denotes 0.6 and 0.2 which are used for a comparison of the three groups of SCVs.

to this dataset, we chose $\delta_1 = 0.98$ and $\delta_2 = 0.02$. More than 90% of the first 28 SCVs have $q \geq 0.98$ and $\tilde{q} \leq 0.02$ in the fifth subset of SZs. This suggests that the first 28 SCVs are common across the subjects in this subset. Finally, the numbers of common SCVs M_r for all five subsets of SZ group are determined as 23, 30, 33, 35, 28, respectively. For HC group, the numbers are 31, 32, 28, 34, 34, respectively. The number of candidates, M , in the subspace \mathcal{Y}_r is determined as 35, which is the largest one among the ten values. The 25th percentile of the cross-correlation values of the M candidates is used as threshold t for the identification of common components. Each identified common component is consis-

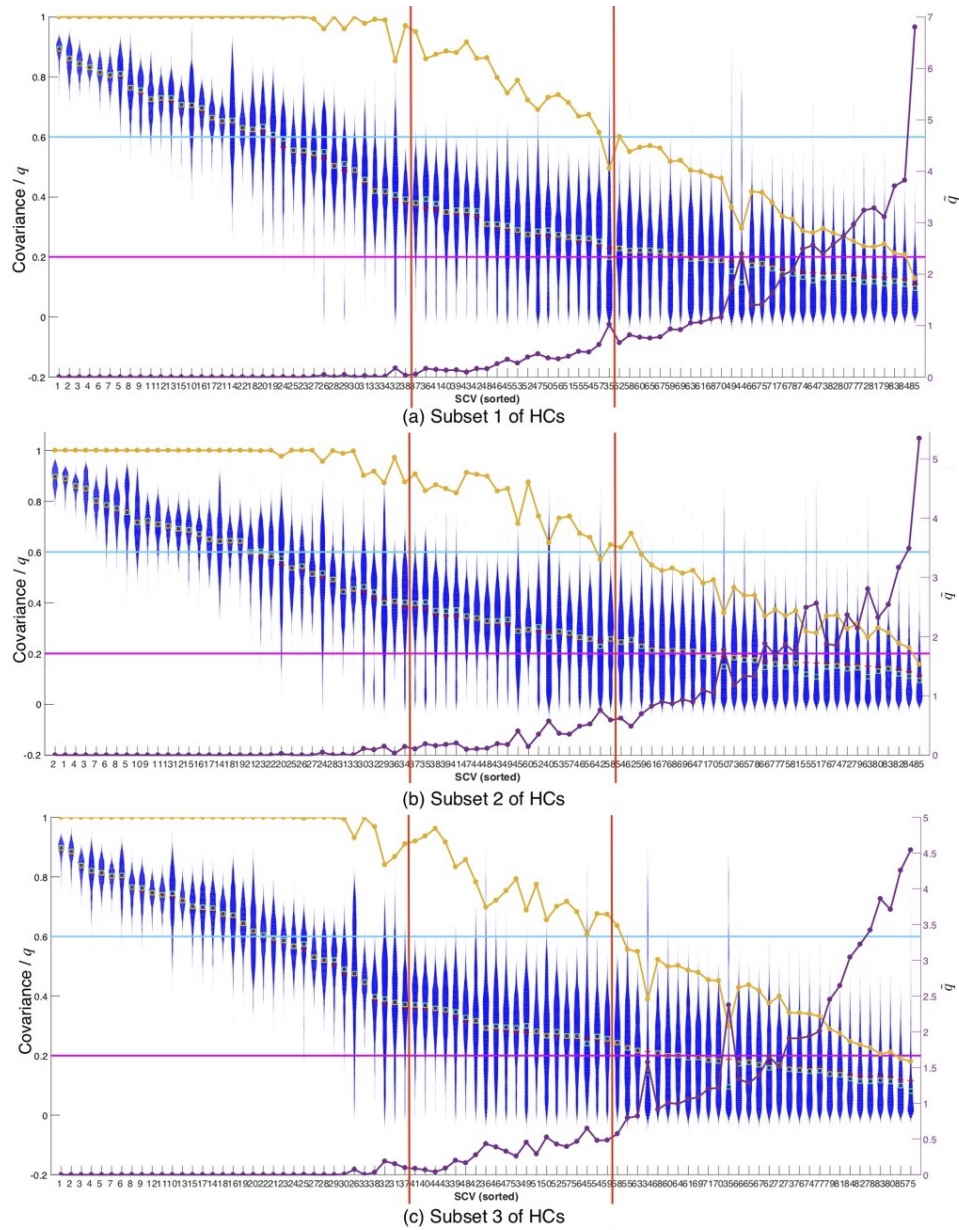


FIG. 4.7. (Part 1) Smoothed distribution of the correlation values of the five subsets of HC group. The red crosses and the green squares denote the mean and median. Two ratios q and \tilde{q} are plotted in yellow and purple. Two vertical red lines denotes the margins between different groups of SCVs. Blue and magenta horizontal lines denotes 0.6 and 0.2 which are used for a comparison of the three groups of SCVs.

tently estimated in at least 80% of the subsets. Note that the values of σ_t^2 , δ_1 , and δ_2 are selected such that the average correlation values in the subspaces are as different as pos-

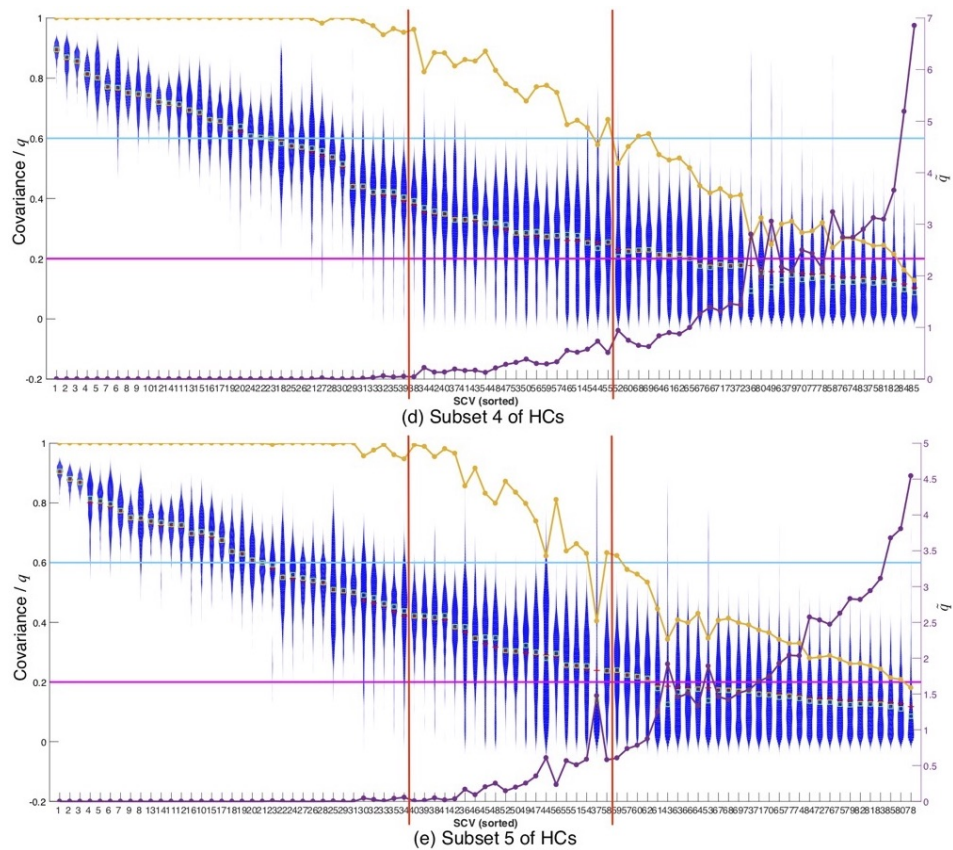


FIG. 4.8. (Part 2) Smoothed distribution of the correlation values of the five subsets of HC group. The red crosses and the green squares denote the mean and median. Two ratios q and \tilde{q} are plotted in yellow and purple. Two vertical red lines denotes the margins between different groups of SCVs. Blue and magenta horizontal lines denotes 0.6 and 0.2 which are used for a comparison of the three groups of SCVs.

sible. Determining the value of M as the largest one across multiple subsets mitigates the sensitivity of the choice of parameters by allowing more candidates available for common component identification.

Artifact removal Using the common component identification method presented in Chapter 4.3.2, 25 and 24 common components are determined for SZ and HC groups separately. Among the determined common components, some of them have high ventricle

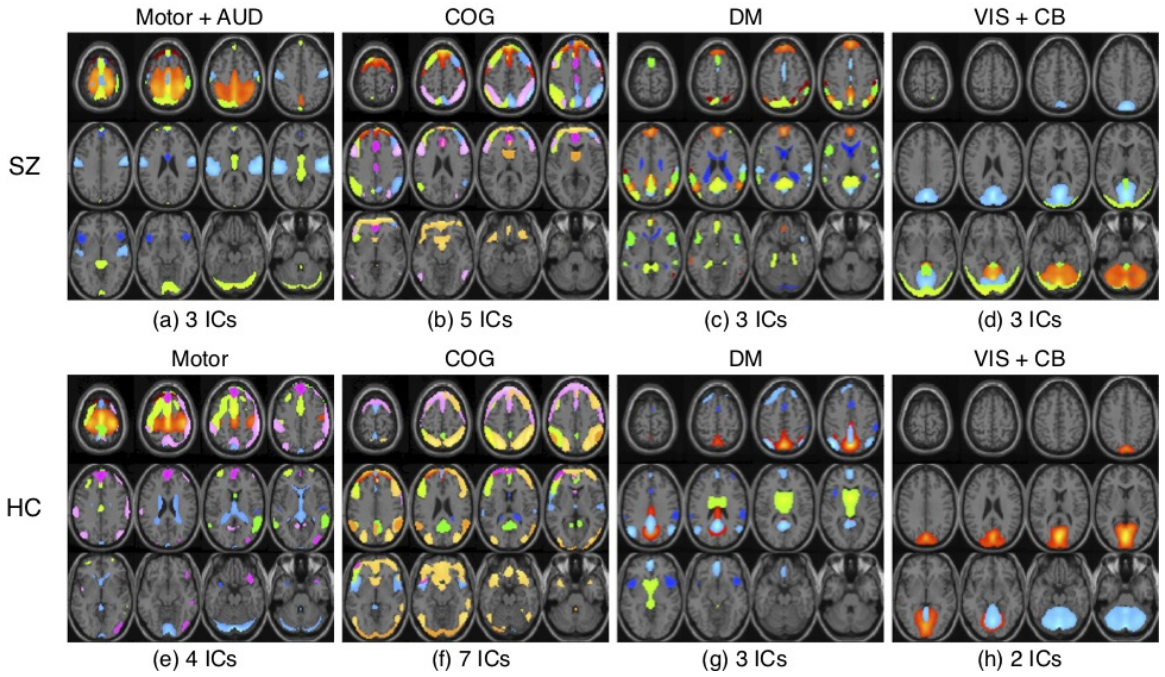


FIG. 4.9. Spatial maps of the common components in six categories: Motor; COG, cognitive control; DM, default mode; AUD, auditory, VIS, visual; CB, cerebellum. (a)-(d) for SZ group and (e)-(h) for HC group. The number of independent components (ICs) that are composited in each subfigure is listed and different colors refer to the spatial maps of individual components.

effects and hence should be removed from further analysis. We utilize the grey matter and cerebrospinal fluid MNI templates included in SPM 12 to distinguish the components [24, 175]. The correlation between the common components and the two templates, C_{GM} and C_{CSF} , are calculated. Each component is normalized to Z-score and thresholded by $Z = 2$ which means that the voxels with $Z < 2$ are set to zero. The components are divided into two groups with respect to the median value of $C_{GM} - C_{CSF}$. The components in the first group are with $C_{GM} - C_{CSF}$ higher than the median hence they are more likely to be RSNs and those in the second group are more likely to be ventricle effects. To ensure all the RSNs are retained and the ventricle effects are removed, we further do a visual check. The grouping by the correlation reduces the burden of a visual check. The median value of $C_{GM} - C_{CSF}$ is 0.18 for SZs and 0.22 for HCs. Finally, 14 common RSNs are obtained for

SZs and 16 for HCs after artifact removal. The average correlation values of the 14 common RSNs of SZs is 0.66 ± 0.15 and that of the 16 common RSNs of HCs is 0.68 ± 0.10 .

The identified common components of each group are typical RSN components like those found in previous studies [11, 113]. They are grouped into six domains, motor, cognitive control (COG), default mode (DM), auditory (AUD), visual (VIS) and cerebellum (CB), according to their anatomical and presumed functional properties as in [11]. Fig. 4.9 shows the composite spatial maps for each cluster. The results show that two common components of SZs include two different interesting RSNs, the first one merges the motor cortex (precentral and postcentral gyrus) and the auditory cortex (superior temporal gyrus) and the other one merges the precuneus gyrus and the right frontoparietal network. The merging of two different RSNs into a single source component does not occur in the HC group. This observation suggests a high correlation between these RSN pairs might result from decreases in connectivity in the brain of individuals with SZ [38, 74, 173] hence more networks are involved in its functioning.

4.4.2 Analysis of group-specific SCVs

From the violin plots in Fig. 4.6(e), we can identify two more subspaces, \mathcal{Y}_{II} and \mathcal{Y}_{III} (distinct subspace). The subspace \mathcal{Y}_{II} has a mix of both high and low correlation values and \mathcal{Y}_{III} has very low correlation values. The value of P that is used to determine the subspace \mathcal{Y}_{II} is set as 40. Further analysis of these two groups is of interest as well. The SCVs in subspace \mathcal{Y}_{II} are called group-specific SCVs since they suggest that the components from some subgroups of subjects have higher correlation hence can be used to identify those subgroups. As we know that the brain functions differently in patients of SZ compared with HCs. Using the group-specific SCVs, we seek to identify subgroups of patients that have RSNs with significant correlation which may result from similar functional patterns.

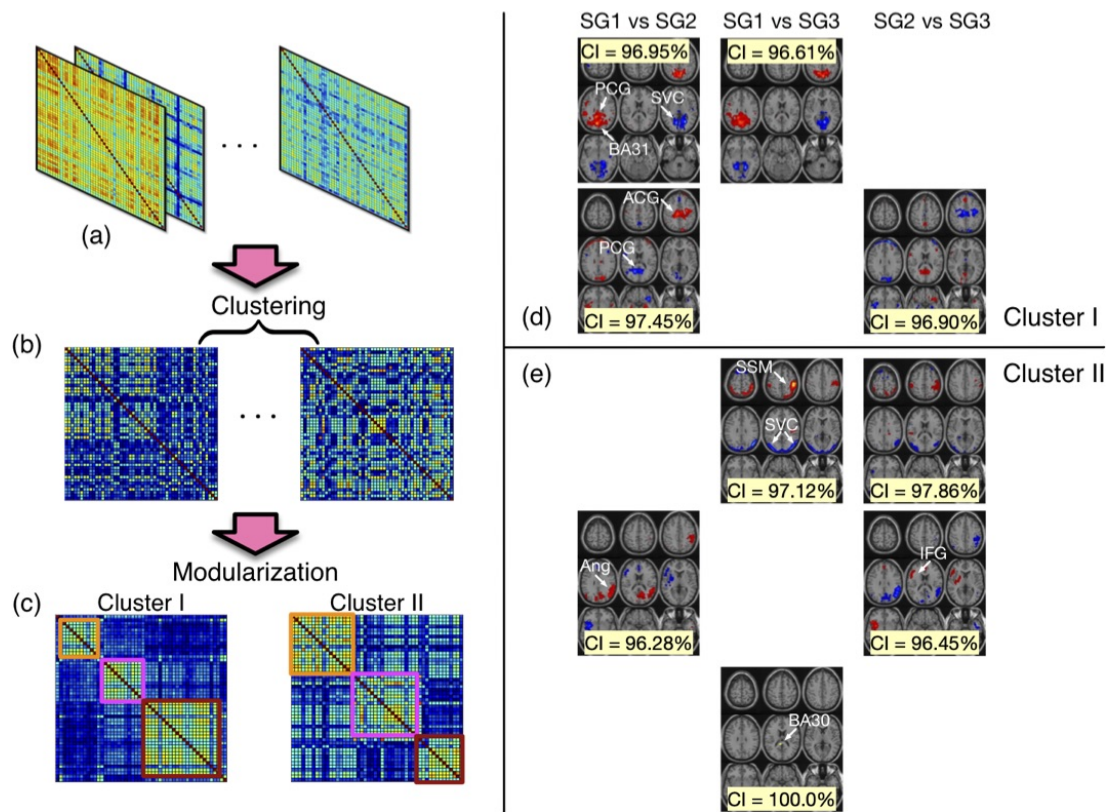


FIG. 4.10. The clustering and modularization processes of the correlation matrices of group-specific SCVs and the two clusters that yield clear subgroups of patients (a-c). Subgroup 1, 2, and 3 are labeled by orange, magenta, and red squares separately. The differences of spatial activation patterns across subgroups in Cluster I (d) and Cluster II (e) are represented by the t -statistic from a two sample t -test with FDR (≤ 0.05) control and the associated confidence interval (CI) is reported. The brain regions that show significant subgroup (SG) differences including: posterior cingulate gyrus (PCG), BA31, secondary visual cortex (SVC), anterior cingulate gyrus (ACG), primary somatosensory and motor cortex (SSM), angular gyrus (Ang), inferior frontal gyrus (IFG), and BA30.

The results indeed show that the subgroups identified using group-specific SCVs reflect similarity within each subgroup and significant differences across subgroups in terms of the spatial activation patterns of their RSNs. We also conduct statistic test on their clinical symptoms that are scored by PANSS and discover differences with certain significance level.

From the distribution plots of correlation values shown in Fig. 4.6(e), the subspace \mathcal{Y}_{II} is determined as that located within two vertical red lines. Meanwhile, those SCVs that are filtered out by common subspace identification are treated as group-specific SCVs as well. Consequently, $N_G = 30$ group-specific SCVs are identified for SZs. A k-means clustering is performed on the correlation matrices of the group-specific SCVs to find out clusters that have similar correlation matrices to help identify source components that are common within the same subgroup of subjects. The mean correlation matrix of a cluster is used to identify the subgroups of subjects. As shown in Fig. 4.10(c) and (d), the mean correlation matrix is rearranged to assemble the subgroup modules by maximizing the modularity of the matrix, which is called modularization. Modularity is a measure that quantifies the community structure of a network that is summarized in a matrix [153]. As shown in Fig. 4.10(c), two clusters with higher modularity, 0.39 and 0.21, each yields three separate clear subgroups. There is no significant difference associated with age among the subgroups ($p \geq 0.1541$).

To compare the spatial activation patterns of the RSNs across subgroups in each cluster, we perform a two-sample t -test on the activation value at each voxel of the spatial map across the subjects within each subgroup. False discovery rate (FDR) correction is conducted throughout all comparisons and the associated confidence interval after FDR correction is reported. Cluster I includes three components and two of them show significant differences in spatial activation patterns, as shown in Fig. 4.10(d). Subgroup 1 yields higher activation in the posterior cingulate gyrus and Brodmann area (BA) 31, and lower activation in the secondary visual cortex compared with subgroups 2 and 3. Subgroup 2 has lower activation than the other two subgroups in the anterior and posterior cingulate gyrus. Cluster II includes five components and three of them show significant differences in spatial activation patterns, as shown in Fig. 4.10(e). Subgroup 3 has lower activation

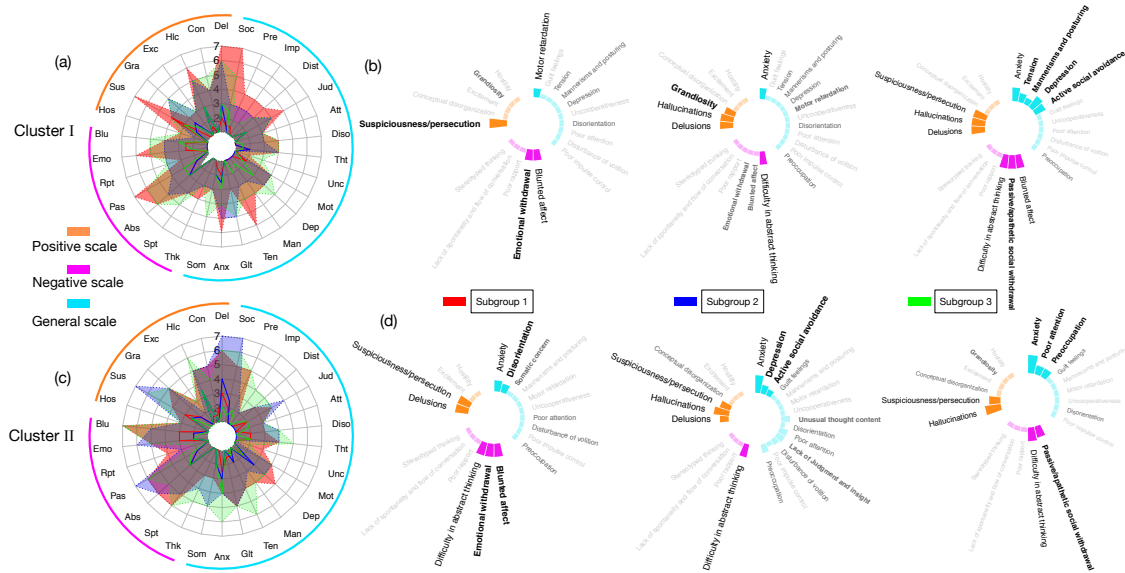


FIG. 4.11. The median (connected by solid lines), minimum, and maximum (connected by dash lines) values of each PANSS score of subgroups in Cluster I (a) and Cluster II (c), and the dominant (bright orange, magenta, and cyan) and absent (fade orange, magenta, and cyan) symptoms of each subgroup in Cluster I (b) and Cluster II (d). In (b) and (d), the bold symptoms refer to those that are unique for a subgroup and the translucent symptoms refer to those that are absent from all three subgroups.

in the primary somatosensory and motor cortex, and higher activation in the secondary visual cortex. Subgroup 2 has lower activation in angular gyrus and higher activation in the inferior frontal gyrus. A particular case is the very small area of activation in BA30 that shows significant differences with 100% confidence interval after FDR correction between subgroups 1 and 3.

A multivariate analysis of variance (MANOVA) is conducted on five statistics—mean, standard deviation, median, minimum, and maximum—of all the thirty PANSS scores [108], including seven positive, seven negative, and sixteen general scales. The MANOVA yields in $F\text{-score}=3.978$ ($p = 6.816 \times 10^{-5}$) that demonstrates significant differences across the three subgroups in Cluster I (Cluster II was not significant). Fig. 4.11 summarizes the

dominant and absent symptoms of each subgroup. The dominant symptoms of a subgroup refer to those that have median value greater than 2 or the median value is 2 for one subgroup while is 1 (which means absent) for the other two subgroups. In Cluster I, as shown in Fig. 4.11(b), subgroup 3 has more dominant symptoms, subgroup 2 has more absent symptoms, and subgroup 1 has obvious broader range for a number of symptoms such as delusions, tension, lack of judgment and insight, and active social avoidance. In Cluster II, as shown in Fig. 4.11(d), all three subgroups have several dominant symptoms. Subgroup 2 has more absent symptoms and subgroup 3 has broader range for symptoms such as stereotyped thinking, anxiety, and tension. All subgroups possess their unique dominant and absent symptoms. We also conduct a MANOVA on the symptoms present in all three subgroups. The MANOVA detects significant differences among the subgroups in Cluster I with F-score=4.1367 ($p = 8.302 \times 10^{-5}$). In Cluster II, only the standard deviation demonstrates significant differences among subgroups with F-score=3.3846 ($p = 0.0404$).

4.4.3 Discussion

Through the investigation of spatial activation patterns of the networks across subgroups, we find several interesting networks that show significant subgroup differences. Most of the networks such as the cingulate gyrus [152], somatosensory and motor cortex [17], angular gyrus, inferior frontal gyrus [107], and secondary visual cortex [172] are reported to be related to SZ [177, 191]. One particular case is the third component in Cluster II because the activated region that shows significant differences between two subgroups is very small yet very interesting. This network is BA30 which does not have a specific name and only the function of its left part, where the activation pattern shows significant subgroup differences, is reported in [157, 188]. Its function is related to attending to speech and listening to sentences. Hearing voices is the most common type of hallucination—one of the typical symptoms—in people with SZ.

In addition to studying the differences across the identified subgroups using the spatial maps of the networks extracted from fMRI data, we also investigate the differences in terms of their clinical data—PANSS scores. PANSS scores—1 means absent and 7 means extreme—are medical scales used for measuring symptom severity of patients with SZ [108]. The self-reported symptom scores are, in general, subjective and noisy, and hence not effective in terms of categorization of disease. Focusing the analysis on individual PANSS scores is not sufficient to describe the subgroups. By investigating the PANSS scores via a MANOVA, we find significant differences across the subgroups and identify unique dominant and absent symptoms for each subgroup. The high significance level provides more confidence in the identified subgroups in Cluster I. Extracting reliable information of the subgroups of SZ from both the neuroimaging data and clinically diagnostic data can potentially lead to a better understanding of the underlying heterogeneity of the disorder and in the future may lead to improved categorization and treatment strategies.

4.5 Summary

Given the importance of common and distinct subspace analysis in medical imaging data analysis, a number of recent studies had a focus on this aspect, in particular for fusion of different modalities or tasks where only a couple of datasets are jointly analyzed. However, joint analysis of large-scale medical imaging data such as multi-subject fMRI data collected from tens, or typically hundreds of subjects enables one to leverage the rich information across the datasets. In this chapter, we introduced a new method called IVA-CS to extract subspaces from at least a hundred of datasets by leveraging the strength of IVA in identification through successful preservation of the complete SCV structure. This allows for efficient identification and estimation of subspaces by carefully studying the dependence structure of SCVs. IVA-CS also mitigates the high dimensionality issue of IVA

by introducing subset analysis to determine a desirable number of datasets that is high enough to exploit the dependence across datasets and is not affected by issues regarding high dimensionality. The simulation study verified the ability of IVA to preserve subspace structure and its application to real fMRI data demonstrated its effectiveness. The identified common components with two linked networks provided evidence of the functional dysconnectivity in the brain of SZs. A subspace of group-specific SCVs was identified by IVA-CS for the SZ group as well. The subgroups of SZ recognized using the group-specific SCVs exhibited significant differences in terms of their brain networks as well as their clinical symptoms that are measured by PANSS. These findings emphasize the importance of interpreting subtypes of SZ in terms of both the neuroimaging data analysis and the clinically diagnostic data. A better understanding of the underlying heterogeneity of the disorder may lead to improved categorization and treatment strategies.

Chapter 5

QUANTITATIVE STUDY OF RESTING-STATE DFNC

The study of the dynamics of human brain using fMRI data emerged due to evidence that the brain exhibits changes in functional patterns, in terms of BOLD activation over the scanning period [95]. Studies of the dynamics of the brain enabled the identification of unique functional network connectivity states and provided new insights into mental disorders [18, 30, 72, 125, 141, 162, 181]. DFNC summarizes the association among functional networks and is widely used for the study of dynamics. However, most of previous studies extracted dFNC information using the temporal variabilities of networks though spatial variability is gaining increasing attention recently. In this chapter, we propose the use of a recent method, acIVA, to simultaneously capture the temporal and spatial variabilities of brain networks. Through a graph-theoretical analysis, we demonstrate that the rich dynamic information captured in the spatial domain enables the identification of more distinguishable features compared with that in the temporal domain. We also propose a goal-driven scheme for the determination of the number of transient states in a dynamic study. We apply the proposed methods to the resting-state COBRE data to demonstrate their effectiveness.

5.1 Introduction

There is evidence that shows that the intrinsic functional patterns in the human brain change over time, and those time-varying—dynamic—patterns are studied using resting-state fMRI data [58,90,94,95]. The dFNC information that measures the association among the BOLD activation patterns of RSNs has been the most commonly used feature for the dynamic study of human brain [10, 30, 51, 62, 79, 103, 155, 189]. Unique FNC patterns are identified in studies to gain a better understanding of mental disorders such as SZ either when compared with an HC group or in a longitudinal study [125, 141, 162, 189].

However, previous studies conducted a dFNC analysis using the time courses of BOLD activity by assuming the spatial domain is static [10, 51, 103, 189]. Spatial variation of BOLD activity is observed as changes in the volume of a functional network or variations in the activated regions within a functional network and has started to attract attention because they enrich the dynamic study of brain function [98–100]. Previous studies have shown that simultaneously considering temporal and spatial changes yields more distinguishable RSNs between subject groups [100, 105, 116]. Studies that compute dFNC using the spatial maps of brain networks also have emphasized the importance of the assumption of spatial variability in a dynamic study by detecting significant differences between the patients with mental disorders such as between those with SZ and the HCs [25, 27, 141]. The rich samples in the spatial domain of the RSNs guarantee a more reliable computation of dFNC using spatial maps compared with using time courses. Therefore, it is desirable to propose the use of an algorithm that can accurately capture the spatial variabilities of RSNs and make effective use of the spatial variability for dynamic study such as the dFNC analysis.

Identifying discrete transient states that are characterized by FNC patterns is a common strategy in studying the dynamic evolution of brain function [141, 196]. The determi-

nation of the number of states is essential while there is no effective method for its selection. People either select the value that yields the lowest error or cost regarding the clustering methods they use to identify the states, or use multiple values and conduct a comparison. In the study of brain functions of patients with mental disorders, a key point is to find biomedical patterns that are unique for the patients and hence are distinguishable between patients and HCs. A scenario where a specific number of states with different distinguishable features are identified is preferable. We propose to determine the number of states through a comprehensive study with the research goal, *i.e.*, a goal-driven scheme.

Graph-theoretical analysis has been widely used in the study of brain FNC and there are a variety of metrics being defined to characterize FNC [39, 178]. After the identification of transient states by clustering dFNC, conducting a graph-theoretical analysis enables one to quantitatively compare dFNC across states [124, 197]. The graph-theoretical metrics that demonstrate significant group differences are of special interest. In this work, we demonstrate that a comprehensive study of the graph-theoretical metrics is a good practice of the proposed goal-driven scheme for the selection of the number of states in dynamic study. Through a comprehensive study of the graph-theoretical metrics, we are able to identify a scenario where all states have unique characteristics in terms of the summary of graph-theoretical metrics that are distinguishable between subject groups.

To ensure a successful graph-theoretical analysis that yields distinguishable graph-theoretical metrics between groups, it is important to extract RSNs that preserve as much individual subject variability as possible. Both temporal and spatial variabilities of BOLD activity are important in order to gain a better understanding of brain dynamics. However, existing methods such as group ICA [48] and joint ICA [47] can only effectively capture either temporal variability or spatial variability by making relatively strong assumptions. The recent method, acIVA, inherits the ability of IVA to capture the variability of RSNs in both

temporal and spatial domains and enables a more efficient decomposition by making use of reference signals such as the spatial maps of RSNs. acIVA is able to precisely preserve spatial variability by adaptively tuning the constraint parameter that controls the spatial association between reference signals and the source estimates. This makes it desirable to compute FNC matrices using spatial maps that have rich samples, hence leading to successful graph-theoretical analysis of sdFNC. The acIVA method also reduces the undesirable effects of high dimensionality that frequently arise during a dynamic study. We describe the issue of high dimensionality and its relation to the dynamic study in Chapter 5.2.2. In addition, acIVA eliminates the tough alignment process across multiple decompositions due to the use of reference signals [27].

Therefore, in this chapter, we apply acIVA using the IVA-L-SOS algorithm to the resting COBRE data to effectively capture both temporal and spatial variabilities of RSNs for dynamic study. We compute tdFNC and sdFNC and perform k-means clustering on dFNC matrices to identify transient states. A graph-theoretical analysis is conducted on FNC to characterize each state by summarizing the global graph-theoretical metrics that show significant group differences. We propose a goal-driven scheme for the determination of an optimal number of states, which is a comprehensive study of the graph-theoretical metrics in this case. A following analysis of nodal graph-theoretical metrics is conducted.

5.2 Methods

In this section, we present the framework of using acIVA for dynamic analysis of fMRI data, including data formation by adopting the sliding window approach, a detailed introduction of acIVA algorithm, the extraction of reference signal, the graph-theoretical analysis that is used for a quantitative study of dFNC, and the proposed goal-driven scheme for the determination of the number of states N_s .

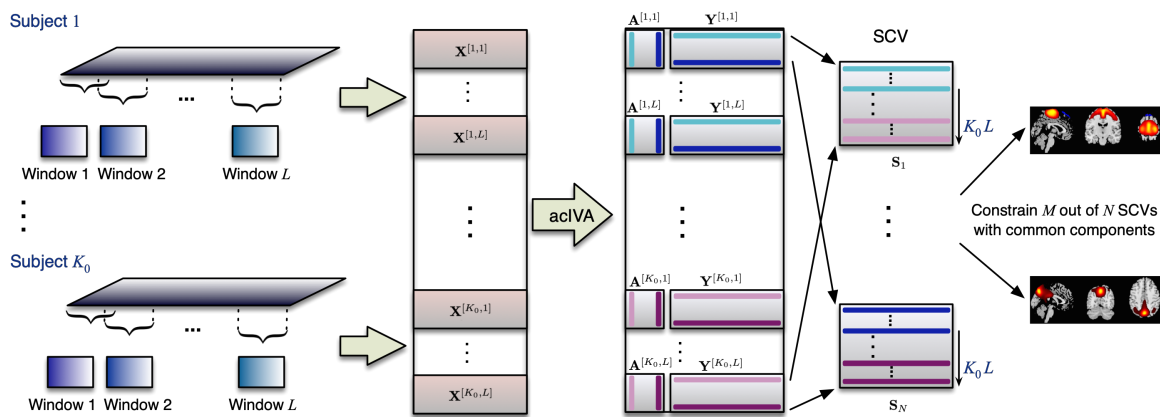


FIG. 5.1. Dynamic study using acIVA with windowing strategy

5.2.1 Data formation for dynamic analysis

The sliding window approach facilitates dynamic study of fMRI data that is acquired within a certain duration [141]. In a sliding window approach, the entire scanning period is divided into overlapping windows of length T_w , yielding L windows for each subject, as shown in Fig. 5.1. In our case, this results in $L \times 179$ datasets. Joint analysis of a large number of datasets typically involves estimation of a large number of parameters with a limited number of samples, which degrades the estimation of the spatio-temporal dynamic features. This motivates the use of an algorithm that effectively captures the variability in both the spatial and temporal domains from a large number of datasets.

IVA is a data-driven technique that extends ICA to multiple datasets and makes effective use of the dependence across datasets [4]. IVA also relaxes the assumptions made in other joint blind source separation solutions, such as group ICA [48] which assumes a common spatial signal space, and joint ICA [47] which assumes a common temporal signal space. IVA simultaneously estimates the demixing matrices of all datasets in order to obtain dataset-specific time courses and spatial maps, effectively capturing both the temporal and spatial variability of functional networks across datasets [25, 27, 118, 141]. However,

this flexibility comes at a cost. With a limited number of samples the performance of IVA degrades as the number of datasets and/or the model order—the number of sources—increases [27, 136]. This issue is referred to as the curse of high dimensionality in IVA and is addressed by using a novel algorithm, acIVA, that incorporates reference information into the IVA decomposition.

5.2.2 Adaptively constrained IVA

The acIVA algorithm is a semi-blind source separation technique that incorporates reference information regarding the time courses or spatial maps into the IVA decomposition. This reference information guides the decomposition towards a desirable solution in high-dimensional scenarios thereby addressing the issue of high dimensionality [27]. In this section, we introduce the general IVA model followed by a description of the acIVA technique.

As we introduced in Chapter 2.3.2, given K datasets each containing V samples, IVA finds K demixing matrices by minimizing the mutual information among the SCVs, which results in the following cost function

$$\begin{aligned} \mathcal{J}(\mathbf{W}) &= \sum_{n=1}^N \mathcal{H}(\mathbf{y}_n) - \sum_{k=1}^K \log|\det \mathbf{W}^{[k]}| \\ &= \sum_{n=1}^N \mathcal{H}(\mathbf{y}_n) - \sum_{k=1}^K \sum_{n=1}^N \log \left| (\mathbf{h}_n^{[k]})^\top \mathbf{w}_n^{[k]} \right| \end{aligned} \quad (5.1)$$

such that the estimated sources of each dataset are obtained as $\mathbf{y}^{[k]}(v) = \mathbf{W}^{[k]} \mathbf{x}^{[k]}(v)$ for $k = 1, \dots, K$, where $\mathbf{W} = \{\mathbf{W}^{[1]}, \mathbf{W}^{[2]}, \dots, \mathbf{W}^{[K]}\}$ denotes the demixing matrices, \mathbf{y}_n denotes the estimated SCV, $\mathcal{H}(\cdot)$ denotes the (differential) entropy, and $\mathbf{h}_n^{[k]}$ is a unit vector resulting from the decoupling process that is perpendicular to all rows of $\mathbf{W}^{[k]}$ except $\mathbf{w}_n^{[k]}$ [26, 131].

The acIVA algorithm guides the decomposition with prior information such as properly selected reference signals for the source components. The IVA decomposition is

hence achieved by minimizing the cost function in (5.1) subject to an inequality constraint $g_n(\mathbf{y}_n^{[k]}, \mathbf{d}_n) = \rho_n - |\text{corr}((\mathbf{y}_n^{[k]})^T \mathbf{d}_n)| \leq 0$, where $0 \leq \rho_n \leq 1$ is the constraint parameter that provides the lower bound for the similarity between the estimate $\mathbf{y}_n^{[k]}$ and the reference signal \mathbf{d}_n that is measured using Pearson correlation. The cost function of acIVA is defined by incorporating an inequality constraint in the IVA cost function, yielding

$$\mathcal{J}^c(\mathbf{W}) = \mathcal{J}(\mathbf{W}) - \sum_{k=1}^K \frac{1}{2\gamma_k} \sum_{m=1}^M \left\{ \left[\max\{0, \mu_m^{[k]} + \gamma_m g_m(\mathbf{y}_m^{[k]}, \mathbf{d}_m)\} \right]^2 - (\mu_m^{[k]})^2 \right\}, \quad (5.2)$$

where $\mathcal{J}(\mathbf{W})$ is the IVA cost function as defined in (5.1), M ($0 \leq M \leq N$) is the number of source estimates to be constrained, $\mu_m^{[k]}$ is the regularization parameter, and $\gamma_m > 0$ is the penalty parameter [27]. Through an adaptive parameter-tuning process, acIVA yields different values of the lower bound $\hat{\rho}$ for the similarity, which allows the estimate to vary across datasets.

The use of reference signals also effectively reduces the effect of high dimensionality, providing a more robust estimation. Additionally, it eliminates the alignment problem across multiple decompositions. When applied to the dynamic study of resting-state COBRE fMRI data, it is possible to divide the 179 subjects into multiple subsets of K_0 subjects (yielding $K = L \times K_0$ datasets) and perform multiple individual IVA decompositions without considering the challenging issue of component alignment. We use the IVA-L-SOS algorithm that uses a multivariate Laplacian distribution model for the sources, like IVA-L [111], and additionally considers the SOS [27], since the Laplacian distribution is a good match for fMRI data and the adding of SOS enables a full statistical characterization of a Laplacian multivariate random vector.

5.2.3 Reference signal extraction

In the implementation of acIVA for extracting dynamics from multi-subject resting-state fMRI data, we use the spatial maps of exemplar RSN components as reference signals. Possible choices for the exemplar RSNs include the pre-defined RSN templates [11] or the group-level RSN components extracted from the same dataset using group decomposition algorithms such as group ICA [25]. In this work, we apply acIVA to the resting COBRE data collected from a SZ group and a HC group, seeking to gain a better understanding of SZ through a fair comparative study of dFNC. Therefore, instead of using arbitrarily pre-defined or estimated RSNs, it is desirable to use common static RSNs that are shared across the subjects of two groups as the reference signals. We extract common RSNs from the data of all 179 subjects using a common subspace analysis method [136] and use their spatial maps as reference signals. All the spatial maps are normalized to have zero mean and unit variance.

5.2.4 Graph-theoretical analysis

The dFNC matrices are computed for each subject by measuring the association among the components of interest—the constrained estimates in acIVA. We perform a graph-theoretical analysis by treating each dFNC matrix as a graph, \mathbf{G} , with the components as nodes and the association among them as edges. Beginning with \mathbf{G} , we compute the graph-theoretical metrics on a sequence of graphs with the link density changes from 20% to 70%, as described in Chapter 3.2.3. In addition to the nodal graph-theoretical metrics introduced in Chapter 3.2.3, we also compute local efficiency for each graph. Local efficiency is computed by taking only the neighbors of a node into consideration and measures the efficiency of information transfer within the neighborhood of each node. The corresponding graph-level global graph-theoretical metric is computed by averaging the values

of each nodal graph-theoretical metric across all the nodes in a graph. The formulas of these metrics are described in detail in [32,33,164]. All the implementations are performed using Matlab code from the Brain Connectivity Toolbox (<https://sites.google.com/site/bctnet/>).

5.2.5 A goal-driven scheme

In an analysis of fMRI data collected from subjects of different populations, such as a group of subjects with SZ and a group of HCs, the goal is to identify distinguishable biomedical patterns between groups. These distinguishable patterns help us understand the functional differences in the brain between them hence enabling a better interpretation of a disorder. In the dFNC analysis, we perform a k-means clustering on the dFNC matrices to identify several transient states and use N_s to denote the number of states, which is a crucial parameter to be decided. In order to determine distinguishable graph-theoretical metrics that are computed for the dFNC matrices, we perform a two-sample t -test on these metrics between SZs and HCs in each state. The detected significance is reported with FDR control. Along with the goal of identifying distinguishable biomedical features, we propose the use of a goal-driven scheme—a comprehensive study of graph-theoretical metrics in this work—to investigate the influence of N_s . The comprehensive study of graph-theoretical metrics can tell which metrics are distinguishable between groups and how the distinguishable metrics change across states. It would be desirable if in the scenario of the optimal N_s , all the identified states yield distinguishable graph-theoretical metrics that are different in terms of the number and types of metrics.

5.3 Application to multi-subject resting-state fMRI data

We apply acIVA using the IVA-L-SOS algorithm to the resting-state COBRE data. We obtain $L = 16$ datasets for each subject using a sliding window of length $T_w = 24$ with a 50% overlap, yielding 2864 datasets in total. Instead of performing a single acIVA

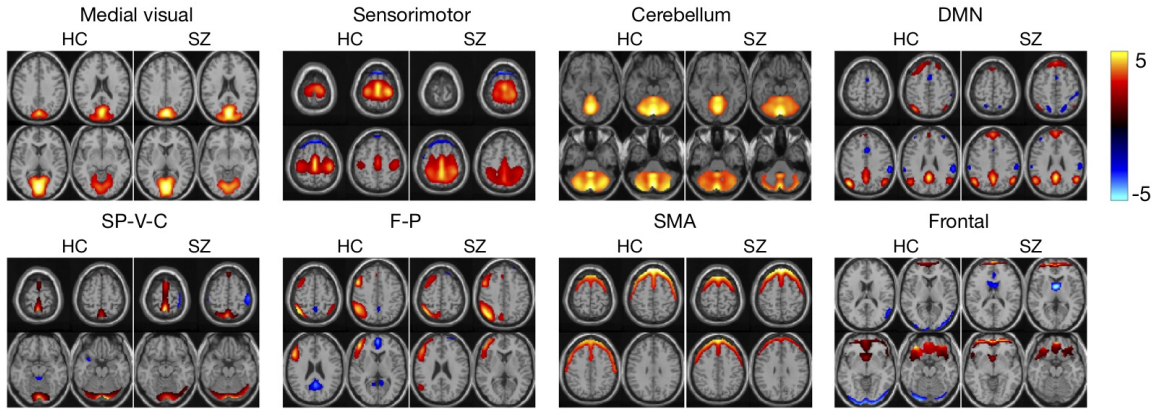


FIG. 5.2. Spatial maps of the eight common components of HC and SZ groups. SP-V-C: super parietal-visual-cerebellum, F-P: frontoparietal, SMA: supplementary motor area.

on the whole data, we divide the subjects into 45 subsets of $K_0 = 4$ subjects and perform acIVA decomposition on each subset. Each subset has $K = L \times K_0 = 64$ datasets, a value that is higher than the optimal value of the number of datasets that allows a reliable regular IVA decomposition [136]. Note that the last subset of HC only has three subjects hence 48 datasets. The model order used for each acIVA decomposition is 20 and the dimension of each dataset is reduced from 24 to 20 using principal component analysis. Using the common subspace extraction method, we obtain eight components that are shared across all 179 subjects. The spatial maps of $M = 8$ common components are used as reference signals to constrain eight out of 20 components that are estimated. The use of reference signals help avoid the component alignment problem across multiple decompositions. The eight common components include medial visual (RSN1), sensorimotor (RSN2), cerebellum (RSN3), DMN (RSN4), super parietal-visual-cerebellum (SP-V-C, RSN5), frontoparietal (F-P, RSN6), supplementary motor area (SMA, RSN7), and frontal (RSN8) components as shown in Fig. 5.2.

We compute two types of dFNC for the estimated RSNs. the first type of dFNC is tdFNC by measuring the correlation among the time courses, and the second type is

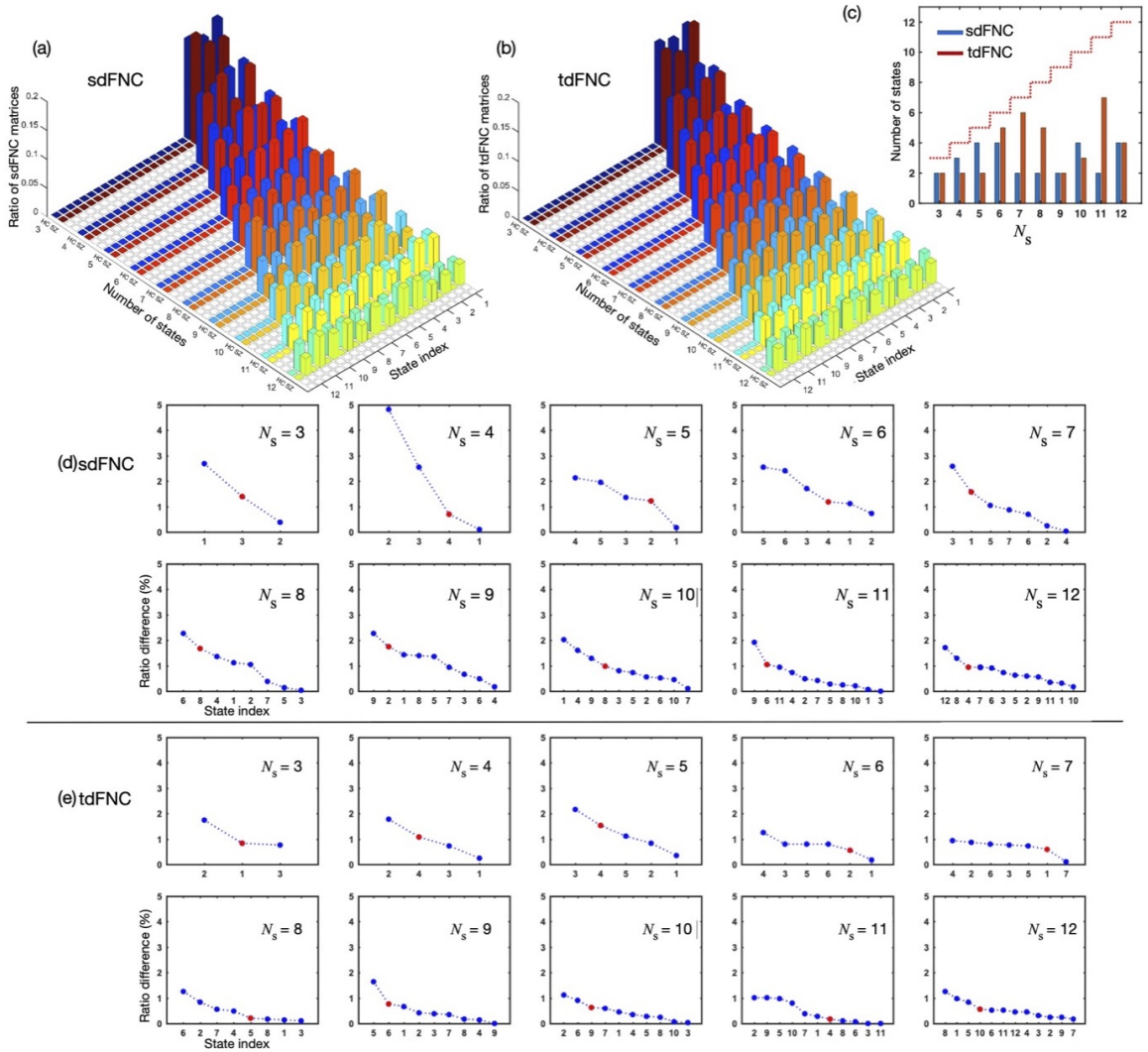


FIG. 5.3. Ratio of the number of dFNC matrices in each state for SZ and HC groups as the value of N_s changes when using sdFNC (a) and tdFNC (b). The number of states with different ratios between the two groups is summarized in (c). The detailed results of the knee point detection that determines the number of states with different SZ and HC subjects are shown in (d).

sdFNC that is computed as the normalized MI among the spatial maps. For each type of dFNC, a k-means clustering is performed to identify the transient states with different values as the number of states, $N_s = 3, 4, 5, 6, 7, 8, 9, 10, 11, 12$, to enable an investigation of the influence of N_s . Each dFNC matrix is a graph and the graph-theoretical metrics are

calculated for the graph with different levels of link density as described in Chapter 3.2.3. A two-sample t -test is performed on each graph-theoretical metric between the SZs and HCs in each state and the detected significance is reported with FDR control.

5.3.1 Graph-theoretical analysis based quantitative study of dFNC

The ratio of the number of dFNC matrices in each state for the SZ and HC groups as a function of N_s is shown in Figure 5.3(a) and (b) for the cases when using sdfNC and tdfNC separately. Figure 5.3(d) and (e) show the ratio difference between SZ and HC groups in each state for the two cases. The elbow criterion that is calculated as the ratio of within-cluster distance to between-cluster distance [10, 196] is used to find the knee point before which the ratio difference is large, indicating the number of dFNC matrices are obviously different between SZ and HC groups in a state. The summary of the number of states with a large ratio difference is shown in Figure 5.3(c). When using tdfNC, the number of states with a large ratio difference is the largest 7 when $N_s = 11$. While when using sdfNC, the number of states with a large ratio difference is bounded between 2 and 4. The results indicate that the identified states using sdfNC are more balanced between SZ and HC groups regarding the number of dFNC matrices.

The statistical test results show that when using tdfNC, in most cases only a few graph-theoretical metrics demonstrate significant group difference. The clustering coefficient and SW always yield significant differences hence whenever the value of N_s is, there are more than one state that have the same characterization in terms of the summary of the distinguishable global graph-theoretical metrics. In contrast, when using sdfNC, more graph-theoretical metrics yield significant group differences, making it possible to uniquely characterize the states by using a comprehensive study of the distinguishable metrics. Moreover, this suggests that the rich spatial variabilities provide more chances to identify unique biomedical patterns of the subjects with SZ. Next, we will introduce the

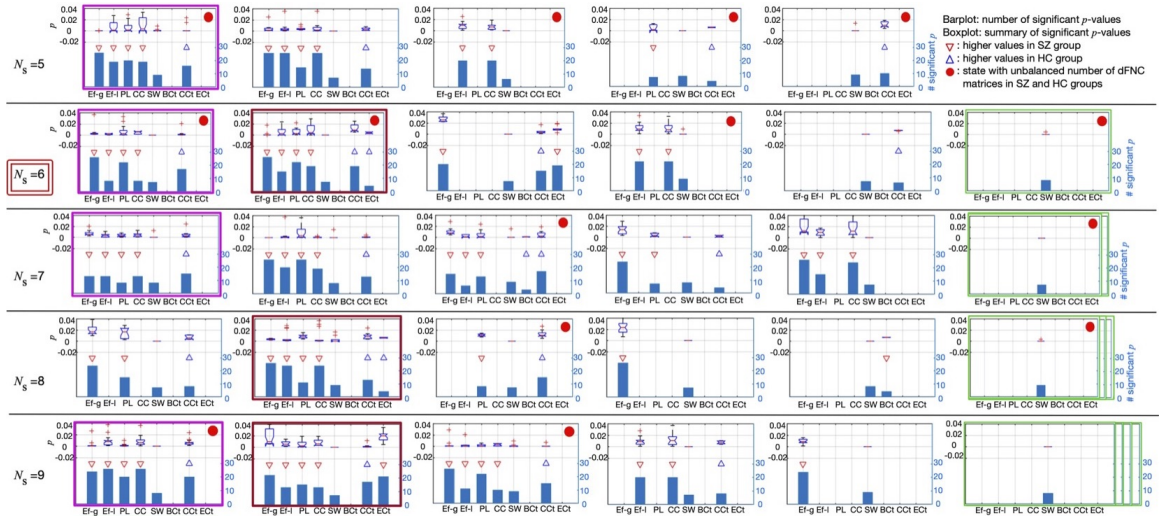


FIG. 5.4. Summary of the statistical test results of global graph-theoretical metrics for the cases with $N_s = 5, 6, 7, 8,$ and 9 . In each plot, the boxplot on the top summarizes the p -values with FDR control, the barplot gives the number of graphs with different link density that has a p -value survives the FDR correction, and the triangular over a bar means the test results show the graph-theoretical metric has higher value in SZs (red) or HCs (blue). The red dot in the upper right corner indicates the number of SZ and HC subjects are different in a state. Ef-g: global efficiency, Ef-l: local efficiency, PL: path length, CC: clustering coefficient, SW: small-worldness, BCt: betweenness centrality, CCt: closeness centrality, ECt: eigenvector centrality

results of a comprehensive quantitative study of sdFNC using graph-theoretical analysis.

The two-sample t -test results of the global graph-theoretical metrics when using sdFNC is summarized in Fig. 5.4. There are ten cases with different values of $N_s \in \{3, 4, 5, 6, 7, 8, 9, 10, 11, 12\}$ but only five cases, $N_s = 5, 6, 7, 8, 9$, are shown as examples. In each plot, the boxplot on the top summarizes the p -values with the FDR control, the barplot gives the number of graphs with different link density that yield graph-theoretical metrics with significant group difference, and the triangular over a bar means the graph-theoretical metric has higher values in SZs (red) or HCs (blue). If there is no triangular over a bar, it means among the graphs some have higher metric values in the SZ group while the others have higher metric values in the HC group. The red dot in the upper right

corner indicates the number of sDFNC matrices are not balanced in SZ and HC groups in a state. There are three states, as labeled in magenta, red, and green rectangular separately, that are robustly estimated. When $N_s \leq 5$, there are missing states compared with the cases where $N_s \geq 6$. The cases with $N_s \geq 7$ yield multiple states that are not distinguishable through the characterization using a summary of global graph-theoretical metrics. Therefore, $N_s = 6$ is the optimal case where all six states are unique regarding the summary of global graph-theoretical metrics. The results illustrates that the comprehensive study of the global graph-theoretical metrics as an example of the goal-driven scheme effectively determines of the optimal number of states N_s . We also use the elbow approach to estimate the optimal value of N_s . The mean value and standard deviation of 100 runs are 6.0200 ± 0.9426 , coinciding with the value suggested by a comprehensive study of graph-theoretical metrics. However, the goal-driven scheme determines the optimal value of N_s in a more interpretable way, which is the distinguishable graph-theoretical features that help us compare between groups.

We take a close look at the nodal graph-theoretical metrics in the case when $N_s = 6$ in order to find interesting individual RSNs. There are two states, states 5 and 6 as shown in Figure 5.5, where all eight components have at least one graph-theoretical metric that demonstrates significant group difference. In state 5, only the complex component (RSN5) that merges multiple brain regions and the component (RSN7)—the supplementary motor area—that consists of superior and middle frontal cortex yield higher values of centrality in SZ while the other components yield higher values of centrality in HC. This high centrality of RSN5 infers that the SZ subjects tend to have more brain regions involved for a certain intrinsic brain function, which may illustrate the dysconnectivity in the brain of SZ. In state 6, RSN6 and RSN8 that are parts of the cognitive control network yield higher values of centrality in HC compared with SZ, potentially suggesting a more efficient cognitive

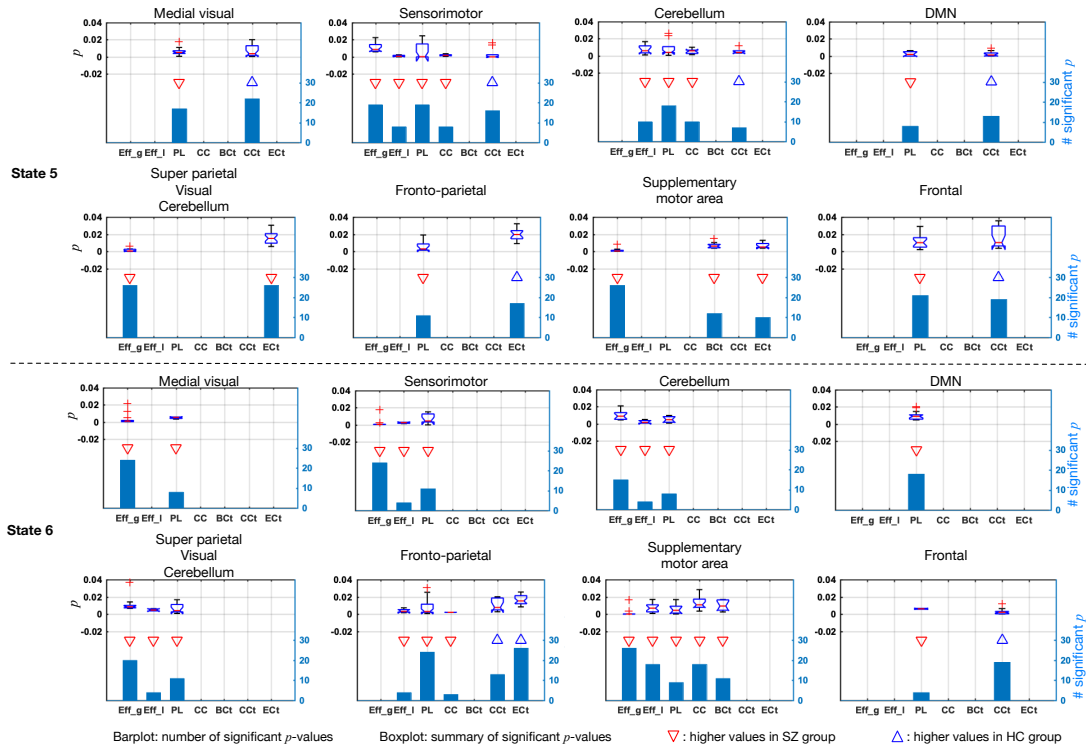


FIG. 5.5. Summary of the statistical test results of nodal graph-theoretical metrics for states 5 and 6 when $N_s = 6$. In each plot, the boxplot on the top summarizes the p -values with FDR control, the barplot gives the number of graphs with different link density that has a p -value survives the FDR correction, and the triangular over a bar means the test results show the graph-theoretical metric has higher value in SZs (red) or HCs (blue). Ef-g: global efficiency, Ef-l: local efficiency, PL: path length, CC: clustering coefficient, BCt: betweenness centrality, CCt: closeness centrality, ECt: eigenvector centrality

control system in the brain of HCs.

The two components RSN5 and RSN7 even yield graph-theoretical metrics with significant group differences in all six states, as shown in Fig. 5.6. Except for the closeness centrality in state 2 for RSN5, the values of all the other graph-theoretical metrics are higher in SZ group than in HC group, indicating the increased involvement of the two components in the brain function of SZs. The increased involvement of RSN5 that merges multiple brain regions once more suggests the dysconnectivity in the brain of SZ. The other component RSN7 that consists of superior and middle frontal cortex has been reported in

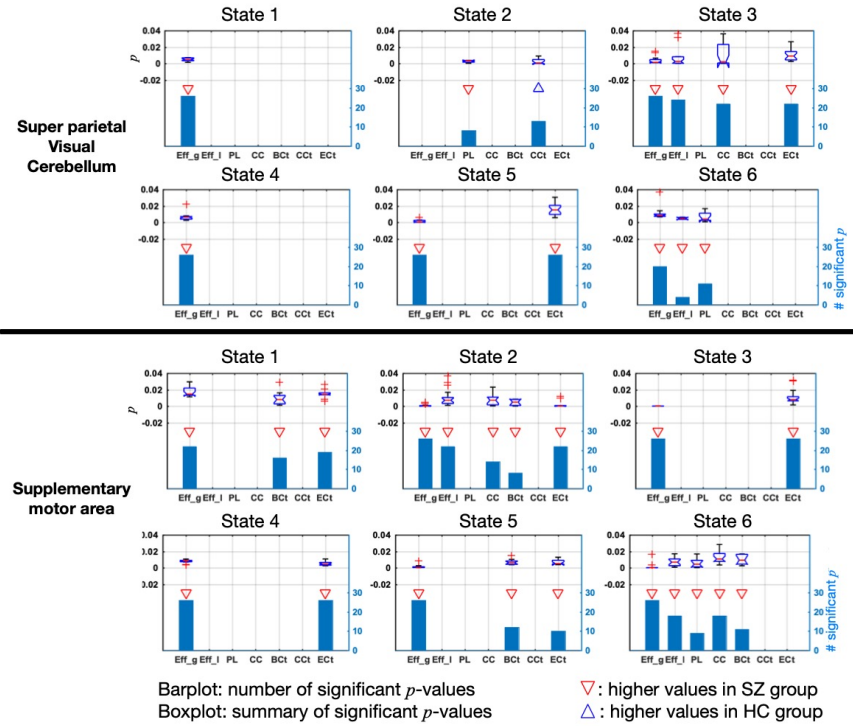


FIG. 5.6. Summary of the statistical test results of nodal GT metrics for the complex component (IC5) and the supplementary motor area component (IC7) when $N_s = 6$. In each plot, the boxplot on the top summarizes the p -values with the false discovery rate (FDR) control, the barplot gives the number of graphs with different link density that has a p -value survives the FDR correction, and the triangular over a bar means the test results show the GT metric has higher value in SZs (red) or HCs (blue). Ef-g: global efficiency, Ef-l: local efficiency, PL: path length, CC: clustering coefficient, BCt: betweenness centrality, CCt: closeness centrality, ECt: eigenvector centrality

many studies to have different level of activation in SZ compared with HC. The other two interesting components, RSN6, the frontoparietal component, and RSN8, the frontal component, yield graph-theoretical metrics with significant group differences in five and four states separately, as shown in Fig. 5.7. All the values of centrality are higher in HCs in these states. The high involvement of RSN6 and RSN8 again supports the conclusion that HCs may have a more efficient cognitive control system.

From the analysis of nodal graph-theoretical metrics, we find that the most interesting

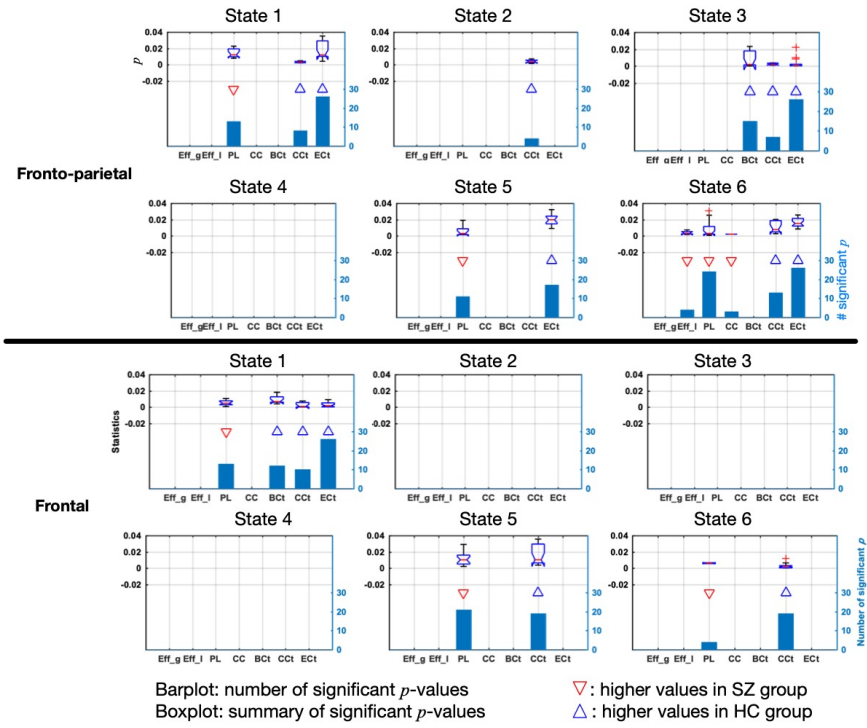


FIG. 5.7. Summary of the statistical test results of nodal GT metrics for the fronto-parietal component (IC6) and the supplementary motor area component (IC7) when $N_s = 6$. In each plot, the boxplot on the top summarizes the p -values with the false discovery rate (FDR) control, the barplot gives the number of graphs with different link density that has a p -value survives the FDR correction, and the triangular over a bar means the test results show the GT metric has higher value in SZs (red) or HCs (blue). Ef-g: global efficiency, Ef-l: local efficiency, PL: path length, CC: clustering coefficient, BCt: betweenness centrality, CCt: closeness centrality, ECt: eigenvector centrality

graph-theoretical metric is centrality. An analysis of the centrality yield differences among individual components in terms of their role on the brain function. Four interesting components that yield interpretable graph-theoretical analysis results include RSN5 that merges multiple brain regions, RSN7 that relates to movement control, and RSN6 and RSN8 that are parts of the cognitive network. A study of these four components helps get a better understanding of the differences in the brain function between SZs and HCs, *i.e.*, a less efficient brain for SZs and a better cognitive control system for HCs.

5.4 Summary

In this chapter, we applied acIVA to the resting-state COBRE data to capture both the temporal and spatial variation of RSNs in order to enable a thorough dynamic study. We emphasized the importance of taking spatial variabilities into consideration in the study of brain dynamics using fMRI data by comparing the graph-theoretical analysis results using tdFNC and sdFNC separately. The results showed that the analysis of spatial variabilities yields more distinguishable features that are potential unique biomedical patterns of SZ. We proposed the use of a goal-driven scheme to determine the optimal value for the number of states N_s when conducting a dFNC analysis and used the systematic study of graph-theoretical metrics as an example to investigate the effectiveness of the goal-driven scheme in this work. The results illustrated that the goal-driven scheme successfully finds a case where the value of N_s is optimal in a more interpretable way compared with using an arbitrary statistical method such as the elbow approach that is independent from the analysis goal. In the case with the optimal N_s , all states were uniquely characterized by graph-theoretical analysis results. The study of nodal graph-theoretical metrics in these states demonstrated that the centrality was the most interesting graph-theoretical metric in this application. Four interesting components that yielded interpretable graph-theoretical analysis results include one component that merges multiple brain regions, one component that relates to movement control, and two components that are parts of the cognitive network. The component that merges multiple brain regions demonstrated increased involvement in the brain function of SZs compared with HCs, illustrating the dysconnectivity of SZ brain. The two components that are parts of the cognitive network had higher values of centrality in HC group, potentially suggesting a more efficient cognitive control system in the brain of HCs.

Chapter 6

STUDY THE ACTIVITY-CONNECTIVITY CO-EVOLUTION OF DBA AND dFNC

In last chapter, we conducted a quantitative study of dFNC. However, the temporal and spatial dynamic properties of BOLD activity itself have not been well studied yet. In this chapter, we investigate the dynamic characteristics of BOLD activity as well as the activity-connectivity co-evolution in the brain. Furthermore, we investigate the possibility of using dynamic information extracted from fMRI data for the study of heterogeneity of SZ since we show the potential of using neuroimaging for studying subtypes of SZ in Chapter 4.

6.1 Introduction

There is rich work showing that both BOLD activity and F(N)C are related to mental and cognitive processes, see e.g., [37, 93, 145, 146]. Differences in BOLD activity and FNC have been separately reported in multiple mental disorders especially in SZ, such as reduced amplitude of low-frequency fluctuation (ALFF) in cuneus [91, 180], reduced BOLD activation in anterior cingulate gyrus [19, 165], dysconnectivity in default mode network [183, 198], and dysconnectivity between thalamus and sensory regions [49, 117, 143, 149, 198]. However, the association between dBA and dFNC is not well studied and it would be desirable to incorporate dBA to gain insight into the activity-connectivity co-evolution by identifying highly correlated patterns between dBA and dFNC.

In [80], the authors investigate the associations between dBA and dFNC in temporal domain, *i.e.*, they measure dBA and dFNC using the temporal variabilities of functional networks. They observe that dBA and dFNC are significantly correlated in time in some cases and not in others and SZ patients show lower or nonexistent associations between dBA and dFNC compared with the HCs. However, like in [80], most previous studies conduct a dFNC analysis using the time courses of BOLD activity by assuming the spatial domain is static [10, 51, 103, 189]. Spatial variation of BOLD activity is observed as changes in the volume of a functional network or variations in the activated regions within a functional network and has started to attract attention, since they enrich the dynamic study of brain function [98–100]. Previous studies have shown that simultaneously considering temporal and spatial changes yields more distinguishable RSNs between subject groups [100, 105, 116]. Studies that compute dFNC using the spatial maps of brain networks also have emphasized the importance of the assumption of spatial variability in a dynamic study, by detecting significant differences between the patients with mental disorder such as between those with SZ and the HCs [25, 27, 141]. However, the spatial activation patterns of dBA themselves are not well explored primarily due to the lack of effective quantification strategies of the spatial property of dBA. An efficient quantification of sdBA does not only enable the investigation of the spatial activation patterns of dBA but also leads to a study of activity-connectivity co-evolution using sdBA and sdFNC of functional networks.

The extraction and efficient quantification of the dynamic features captured through temporal and spatial variation leads one to analyze their importance in studying a mental disorder such as SZ. In Chapter 4, we introduced the significant interest in studying the subtypes of SZ and show that fMRI alone can identify subgroups of SZ that demonstrated significant differences in terms of clinical symptoms and helps understand the heterogeneity of SZ. However, these subgroups were identified through static imaging features. This

motivates an investigation of the effectiveness of dynamic neuroimaging features for identifying and studying the heterogeneity of mental disorders such as SZ.

In this chapter, we propose the novel use of acIVA that enables us to simultaneously capture the dFNC and dBA in the spatial and temporal domains, and also provides an effective quantification of sdBA, as part of the algorithm. We demonstrate that measuring the association between reference signals and the source estimates as part of the acIVA algorithm provides an efficient quantification of sdBA. In order to study the novel use of acIVA to capture the dynamic features, we propose a simulation study and demonstrate that acIVA yields a desirable performance in capturing spatial dynamics by accurately recovering the association between reference signals and the targeted estimates. We then apply acIVA to the resting-state COBRE fMRI data to investigate the association between tdba and sdBA and study the activity-connectivity co-evolution of sdBA and sdFNC.

6.2 Efficient quantification of sdBA

In the application of acIVA to real fMRI data, we use the spatial maps of RSNs as reference signals in order to emphasize the importance of spatial variabilities and the efficient metric of sdBOLD that is provided by acIVA. As was introduced in Chapter 5.2.2, through an adaptive parameter-tuning process, acIVA yields different values of the lower bound $\hat{\rho}$ for the similarity, which allows the estimate to vary across datasets. Consequently, acIVA is able to effectively capture the variability across datasets that describes sdBA. The use of reference signals in acIVA also provides us with a useful metric for quantifying spatial variation. In this work, we propose a novel use of acIVA to efficiently quantify the spatial variability using the similarity between the estimates and corresponding reference signals.

We first use a simulation study to demonstrate that acIVA is able to accurately recover the spatial variabilities due to the adaptive parameter-tuning process. When applied to real

fMRI data, we investigate the association between the temporal and spatial properties of dBA.

6.2.1 Simulation study

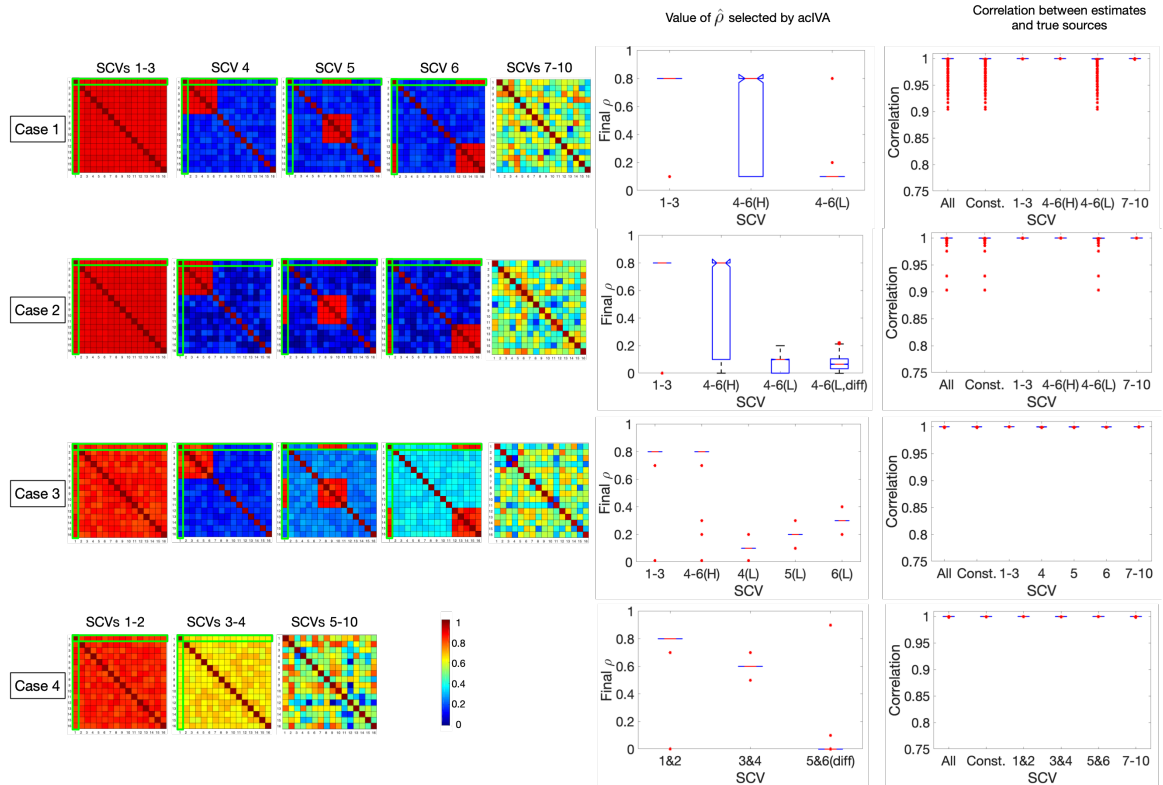


FIG. 6.1. Visualization of the correlation matrices and the decomposition results of acIVA in the four cases of simulation. In the ticklabels of x -axis in the boxplots, “H” refers to the results of components that are highly correlated (c_1) with the reference signal, “L” refers to the results of components that are not highly correlated (c_2), and “diff” refers to the cases where we summarize the differences between the tuned values of $\hat{\rho}$ and the ground truth. The boxplot displays the median, the 25th and 75th percentiles of the values with whiskers extending to the 99.3% confidence interval and some outliers in red asterisks beyond whisker.

The acIVA implementation enables the quantification of sdBA by adaptively tuning the amount of correspondence between the estimated functional networks and the reference

signals. We use simulated data to demonstrate the ability of acIVA to accurately capture the underlying spatial variability of dBA. In order to simulate fMRI-like sources that are super-Gaussian distributed, we generate $N = 10$ SCVs that are multivariate generalized Gaussian distributed with randomly selected shape parameter $\beta \sim \mathcal{U}(0.1, 0.8)$ that forms a super-Gaussian distribution, and different correlation matrices $\mathbf{R}_n \in \mathbb{R}^{16 \times 16}, n = 1, \dots, 10$, as described below in the four cases and shown in Fig. 6.1. Out of the ten SCVs, we constrain six SCVs, where the first component in each of the first six SCVs is used as the reference signal, and the other fifteen components are used to generate $K = 15$ datasets. The sources for the k th dataset are obtained by concatenating the k th row from all SCVs. Each dataset, \mathbf{X} , is computed by mixing the ten sources using a mixing matrix, whose elements are randomly drawn from a uniform distribution $\mathcal{U}(0, 1)$. We apply acIVA using the IVA-L-SOS algorithm on the K datasets with the first $M = 6$ components are constrained using the reference signals. The value of constraint parameter ρ in acIVA is tuned from a default set $\mathcal{P} = \{0.1, 0.2, 0.3, 0.4, 0.5, 0.6, 0.7, 0.8, 0.9\}$. The details of four cases where the SCVs are generated to have different correlation matrices are as follows and the visualization of correlation matrices is illustrated in Fig. 6.1. If the components within an SCV are highly correlated with the reference signal, it means the spatial activation of the component is relatively stationary and does not vary much across datasets. If the components are barely correlated with the reference signal, it means the component varies a lot across datasets in terms of its spatial activation.

- Case 1: SCVs 1-3 are generated to have a uniform correlation structure with correlation value $c = 0.9$, which means all the components are highly correlated with the reference signal. SCVs 4-6 are generated to have a subset of components that are highly correlated with the reference signal and have high correlation values $c_1 = 0.9$. Those components that are not highly correlated with the reference sig-

nal have correlation values that are randomly selected from a uniform distribution $c_2 \sim \mathcal{U}(0.1, 0.2)$. SCVs 7-10 are generated to have a correlation matrix with random entries, $\mathbf{C} = \mathbf{Q}\mathbf{Q}^\top$, $\mathbf{Q} \sim \mathcal{U}(-0.2, 0.8)$, that allow the components to have different correlation values with the reference signal.

- Case 2: SCVs are generated using the same parameters as in Case 1 except that the low correlation values in SCVs 4-6 are randomly selected from a uniform distribution $c_2 \sim \mathcal{U}(r, \infty, r, \epsilon)$. The default set is updated to be $\mathcal{P} = \{0.001, 0.1, 0.2, 0.3, 0.4, 0.5, 0.6, 0.7, 0.8, 0.9\}$.
- Case 3: SCVs 1-3 are generated to have correlation values $c \sim \mathcal{U}(0.8, 0.9)$. The high correlation values in SCVs 4-6 are $c_1 \sim \mathcal{U}(0.8, 0.9)$ and the low correlation values are $c_2 \sim \mathcal{U}(0.1, 0.2)$ for SCV 4, $c_2 \sim \mathcal{U}(0.2, 0.3)$ for SCV 5, $c_2 \sim \mathcal{U}(0.3, 0.4)$ for SCV 6. The correlation values are set to be in a specific range to investigate the sensitivity of the adaptive parameter-tuning process to varying values in acIVA. SCVs 7-10 are generated in the same way as in Case 1 and 2.
- Case 4: SCVs 1 and 2 are generated to have correlation values $c \sim \mathcal{U}(0.8, 0.9)$. SCVs 3 and 4 have correlation values $c \sim \mathcal{U}(0.6, 0.7)$. SCVs 5-10 are generated to have a correlation matrix $\mathbf{C} = \mathbf{Q}\mathbf{Q}^\top$, $\mathbf{Q} \sim \mathcal{U}(-0.2, 0.8)$. The components in SCVs 5 and 6 have random correlation with the reference signal.

We quantify sdba using correlation between the spatial maps of the estimates and the reference signals. This metric is reflected in the tuned value of $\hat{\rho}$, which we use for measuring the performance of the algorithm. The ground truth of ρ , the lower bound of the correlation, is 0.1 if $c \in [0.1, 0.2)$, 0.2 if $c \in [0.2, 0.3)$, and so on. In most cases, ρ is a single value hence we summarize the tuned values of $\hat{\rho}$ for a direct comparison between $\hat{\rho}$ and ρ . However, the true ρ for components with small correlation values in SCVs 4-6 of Case 2 and all

the components in SCVs 5-6 of Case 4 is not a single value because their correlation values have a large range. For example, the components in SCVs 5-6 of Case 4 have correlation values that change from 0 to 1, hence the true ρ of some components with $c \in [0.1, 0.2)$ is 0.1 while for those with $c \in [0.2, 0.3)$ is 0.2. We then summarize the differences between $\hat{\rho}$ and ρ to assess the performance of acIVA in these scenarios.

The simulation results summarized for 100 realizations demonstrate that the values of $\hat{\rho}$ are very close to the ground truth values, suggesting that acIVA is able to tune the closest lower bound for the correlation between the estimates and reference signals in difference scenarios, as shown in Fig. 6.1. With the constraint of the reference signals, the estimates are accurately recovered and hence yield high correlation values with the ground truth. When applied to real fMRI data for a dynamic study where the sources come from a sequential of windows, the correlation between the spatial maps of the estimates and the reference signals can be a good measure for sdba.

6.2.2 Application to real fMRI data

We apply acIVA using the IVA-L-SOS to the COBRE data to extract the temporal and spatial variations of BOLD activity of RSNs using the model shown in Fig. 5.1 with the constraint of the eight common components shown in Fig. 5.2, the same process as in Chapter 5. An example of the tuned value of $\hat{\rho}$ and the computed value of $\tilde{\rho}$ across 16 windows for one SZ subject and one HC subject is shown in Fig. 6.2. We can clearly see that the spatial variabilities of dBA in the same functional network varies significantly across different subjects. We use spatial maps of the DMN component as an example to demonstrate how $\tilde{\rho}$ quantifies spatial variability. High values of $\tilde{\rho}$ means the estimates are very similar to the reference signal while low values means the estimates deviate from the reference signal, indicating higher variability. It shows that the DMN component varies more across windows for the HC individual than for the SZ individual.

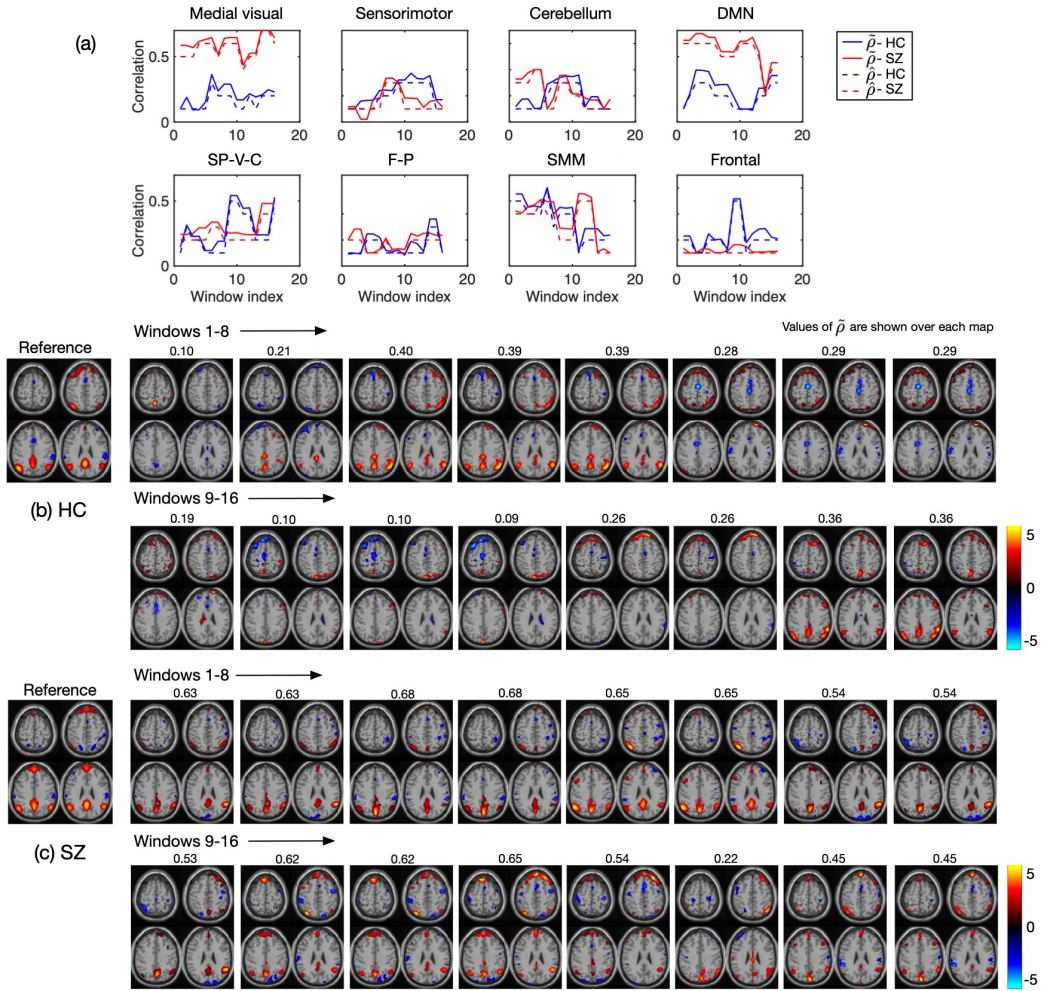


FIG. 6.2. The tuned values of $\hat{\rho}$ in acIVA and the computed correlation $\tilde{\rho}$ between the estimates and the reference signals as a function of windows for a HC subject and an SZ subject (a). The spatial activation of the DMN component varies across windows in HC subject (b) and SZ subject (c). The values of spatial activation are normalized to be z -scores and thresholded using $z_t = 2$.

Spontaneous slow fluctuations of correlated activity is a fundamental feature of the resting brain and can be captured as the BOLD signal that reflects neural synchrony between brain regions [29, 182]. A related measure is fALFF that quantifies the amplitude of these low frequency oscillations. Therefore, we measure tdba by computing the fALFF of time courses as the fraction of the square root of power spectrum integrated in a low

frequency band [0.025-0.15 Hz] that summarizes the most dominant frequencies of BOLD signal during resting-state [195, 199]. Since the variabilities of the spatial maps of RSNs reflect the spatial property of dBA, we quantify sdBA using correlation between the spatial maps of the estimates and the reference signals, $\tilde{\rho}_n = |\text{corr}((\mathbf{y}_n^{[k]})^T \mathbf{d}_n)|$. We hence introduce an effective metric to quantify the spatial variability of dBA which enables an investigation of the relationship between the temporal and spatial properties of dBA for identifying synchronized patterns. We compute the cross-correlation between $\tilde{\rho}$ and fALFF in order to study the association between sdBA and tdBA and denote the $\tilde{\rho}$ -fALFF cross-correlation matrix as $\mathbf{C}^{[k]}$ for each subject, as shown in Fig. 6.3(a). The mean $\tilde{\rho}$ -fALFF cross-correlation matrices $\bar{\mathbf{C}}$ that are averaged across the subjects in SZ group and HC group are shown in Fig. 6.4(a) and a one-sample t -test is performed on $\mathbf{C}^{[k]}$ with FDR control at $p \leq 0.05$. The statistical test results demonstrate that the temporal variabilities and spatial variabilities of dBA of the same brain functional network are more likely to be significantly correlated than those of different networks. SZ group has fewer significantly correlated sdBA and tdBA pairs when compared with HC group, indicating a less efficiently organized brain function in SZ.

6.3 Co-evolution of dBA and dFNC

As there is evidence that both BOLD activity and network connectivity are related to mental and cognitive processes in brain, it is desirable to study the activity-connectivity co-evolution. In this work, we make use of an effective metric $\tilde{\rho}$ for sdBA, enabling the study of activity-connectivity co-evolution in spatial domain using sdBA. We measure sdFNC using the normalized MI among the spatial maps. Pearson's correlation between $\tilde{\rho}$ and sdFNC is calculated and the activity-connectivity co-evolution matrix is denoted as $\mathbf{E}_n^{[k]}$ for each component and each subject, as shown in Fig. 6.3(b).

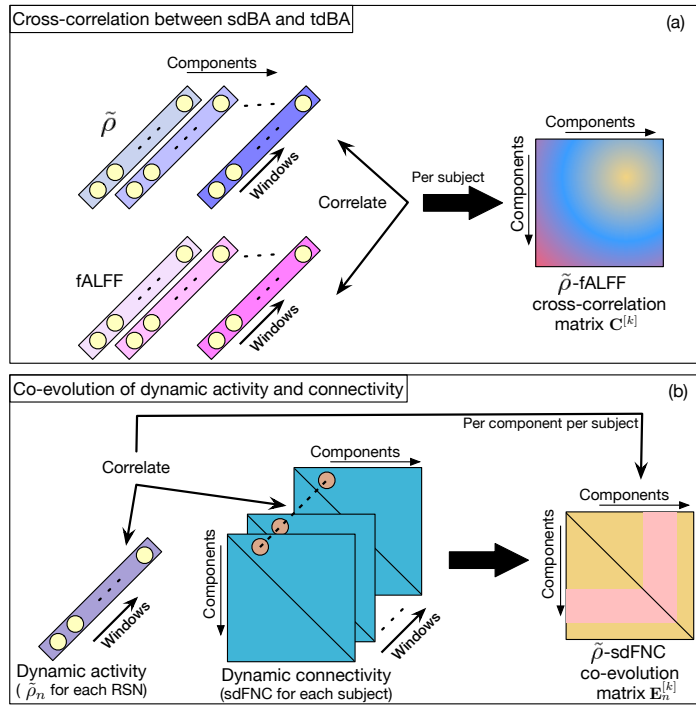


FIG. 6.3. Cross-correlation between sdBA ($\tilde{\rho}$) and tdBA (fALFF) (a) and activity-connectivity co-evolution computed using sdBA ($\tilde{\rho}$) and sdFNC (b).

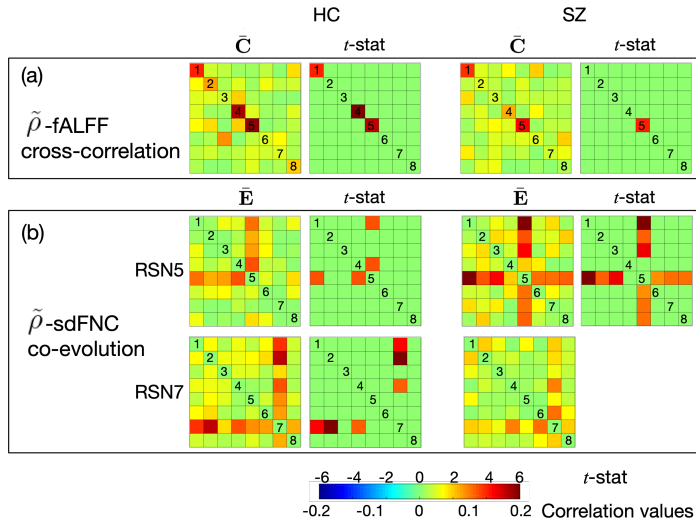


FIG. 6.4. Cross-correlation matrices of two types of dBA (a) and activity-connectivity co-evolution matrices computed using dBA and dFNC (b) that are averaged across subjects in SZ and HC groups. The values of t -statistic with an FDR control are shown.

The investigation of the activity-connectivity co-evolution in spatial domain is shown in Fig. 6.4(b) by demonstrating the mean co-evolution matrices $\bar{\mathbf{C}}$ for two groups and the t -statistics of a one-sample t -test with FDR control. There is a component (RSN5) yielding significant co-evolution between its sdBA and sdFNC in both SZ and HC groups. This component is a complex component that merges multiple brain regions—super parietal, visual, and cerebellum—and it’s the only component that show significant correlation between sdBA and sdFNC for SZ group. Its sdBA activity significantly correlates to more connectivity patterns in sdFNC for SZs compared with HCs. Note that these connectivity patterns are associated with this complex component. The preference of the complex component suggests the reduced efficiency of brain function in SZ because more regions are simultaneously activated for a certain intrinsic function in their brain. HC group has an additional component (RSN7), the superior and middle frontal component (supplementary motor area), that yields significant co-evolution between its sdBA and sdFNC. This illustrates that HCs show better functional organization in terms of the spatial variation patterns in the superior and middle frontal cortex compared with SZ group. The frontal cortex has been widely studied to better understand SZ and there is rich work showing the functional deficits in frontal lobe for SZ [54–56, 88, 144, 151, 159, 168].

6.4 Study of heterogeneity of SZ using dynamic features

The successful use of static features extracted from fMRI data for studying the heterogeneity of SZ motivates a further investigation of the effectiveness of using dynamic features for the study of subtypes of SZ. We study the heterogeneity of SZ by identifying subgroups of SZ subjects using k-means clustering to cluster the $\tilde{\rho}$ -fALFF cross-correlation matrices $\mathbf{C}^{[k]}$ and the activity-connectivity co-evolution matrices $\mathbf{E}_n^{[k]}$ separately. The unique entries of each matrix form a feature, with a length of 64 in the case of $\mathbf{C}^{[k]}$ and

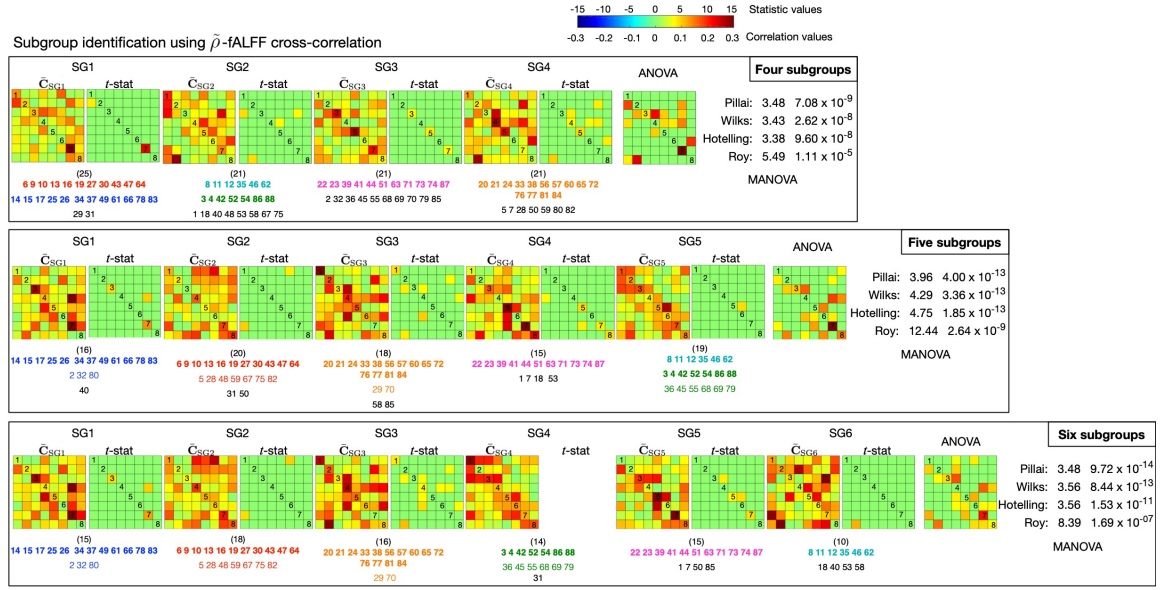


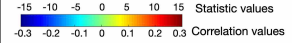
FIG. 6.5. Mean cross-correlation matrices of each subgroup and the statistical test results (with an FDR control) for three scenarios with different values of N_s . The robust clusters of SZ subjects are listed under the correlation matrices using different colors. The colored font in bold refer to clusters that are robustly detected in all three scenarios and the regular colored font refer to clusters that are detected in two scenarios. The font in black refer to subjects that are not belong to any robust clusters. The numbers in brackets denote the number of subjects in each subgroup.

28 in the case of $\mathbf{E}_n^{[k]}$. We use the elbow criterion, which is calculated as the ratio of within-cluster distance to between-cluster distance [10, 196], to determine the number of subgroups N_s . We run the elbow algorithm 100 times, yielding the mean value and standard deviation of 4.31 ± 0.51 and 4.63 ± 0.69 for the two cases respectively. We conduct an extensive investigation on the influence of N_s by forming three scenarios where four, five, and six subgroups of SZ subjects are identified by clustering the dynamic features into four, five, and six clusters.

The mean cross-correlation matrices $\bar{C}_{SGi}, i = 1, \dots, 6$ that are averaged across the subjects in each subgroup for the three scenarios are shown in Fig. 6.5 for the case where we use cross-correlation matrices $\mathbf{C}^{[k]}$. We perform a MANOVA on the correlation values across subgroups in order to identify differences across subgroups, and the four different

Subgroup identification using activity-connectivity co-evolution

	SG1	SG2	SG3	SG4	SG5	SG6	
Four subgroups	(22) 1 16 27 37 39 43 59 73 74 7 51 66 69 71 80 19 24 46 64 6 57	(22) 9 25 28 29 38 85 36 12 18 23 44 50 88 20 33 48 32 40 42 47 63 87	(23) 5 8 15 21 22 26 30 31 49 61 68 75 14 52 62 81 3 13 17 34 65 67 84	(21) 4 10 35 41 48 56 76 77 11 72 78 55 60 79 86 53 82 83 2 54 70 86			
Five subgroups	(17) 4 10 35 41 45 58 76 77 11 72 78 42 65 67 32 33 48	(16) 19 24 46 64 55 60 79 86 53 82 83 3 17 40 87 20	(19) 5 8 15 21 22 26 30 31 49 61 68 75 14 52 62 81 47 54 63	(18) 9 25 28 29 38 85 36 6 13 34 57 12 18 23 44 50 88 84	(18) 1 16 27 37 39 43 58 59 73 74 7 51 66 69 71 80 2 70		
Six subgroups	(16) 5 8 15 21 22 26 30 31 49 61 68 75 47 54 63 11	(15) 4 10 35 41 48 56 76 77 42 65 67 14 52 70 82	(15) 19 24 46 64 55 60 79 86 3 17 40 87 36 66 69	(12) 12 18 23 44 50 88 64 20 33 48 72 81	(15) 1 16 27 37 39 43 58 59 73 74 2 32 53 78 83	(15) 9 25 28 29 38 85 6 13 34 57 7 51 71 80 62	



$\bar{\rho}$ vs. sdFNC

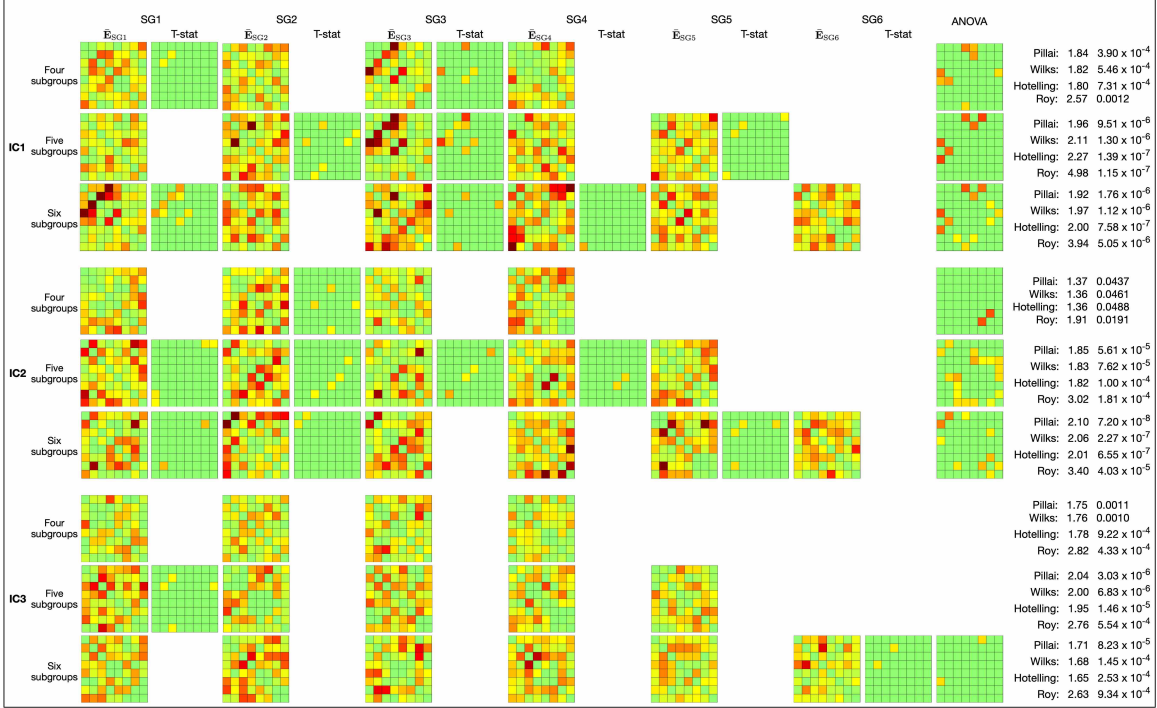


FIG. 6.6. (Part 1) Mean activity-connectivity co-evolution matrices \bar{E}_{SGi} , $i = 1, 2, 3, 4, 5, 6$, of each subgroup and the statistical test results (with an false discovery rate control at $p < 0.05$) for three scenarios with $N_s = 4, 5$, and, 6 . The robust clusters of SZ subjects that are denoted using numbers $k = 1, \dots, 88$ are listed on the top of the figure using different colors. The colored font in bold refer to clusters that are robustly detected in all three scenarios and the regular colored font refer to clusters that are detected in two scenarios. The font in black refer to subjects that are not belong to any robust clusters. The numbers in brackets denote the number of subjects in each subgroup. (*cont.*)

test statistic values—Pillai's, Wilks', Hotelling's, and Roy's—are reported. The MANOVA test results show that there exist significant differences across subgroups in all three scenarios with different values of N_s . To visually compare the correlation patterns across



FIG. 6.7. (Part 2) Mean activity-connectivity co-evolution matrices $\bar{\mathbf{E}}_{SGi}$, $i = 1, 2, 3, 4, 5, 6$, of each subgroup and the statistical test results (with an false discovery rate control at $p < 0.05$) for three scenarios with $N_s = 4, 5$, and 6 . The robust clusters of SZ subjects that are denoted using numbers $k = 1, \dots, 88$ are listed on the top of the figure using different colors. The colored font in bold refer to clusters that are robustly detected in all three scenarios and the regular colored font refer to clusters that are detected in two scenarios. The font in black refer to subjects that are not belong to any robust clusters. The numbers in brackets denote the number of subjects in each subgroup.

subgroups, we plot the statistic values of a one-sample t -test on $\mathbf{C}^{[k]}$ for each subgroup and an univariate analysis of variance (ANOVA) on $\mathbf{C}^{[k]}$ across subgroups with an FDR control at $p < 0.05$. The results from Fig. 6.5 show that each subgroup has a unique cross-correlation patterns and within each subgroup, the correlation values are statistically significant, except for subgroup 4 when $N_s = 6$. These results indicate that the dynamic features extracted from imaging data are effective in identifying unique subgroups of SZ subjects. We check subjects that are clustered into each subgroup, finding some subject clusters that are robustly grouped together, as shown in Fig. 6.5 with numbers denoting subject indices ($k = 1, \dots, 88$) under the correlation matrices. The numbers in bold font and color refer to clusters that are robustly detected in all three scenarios and those in regular font and color refer to clusters that are detected in two arbitrary scenarios. The black numbers refer to subjects that do not belong to any robust clusters. The numbers in brackets denote the number of subjects in each subgroup. In the case where the co-evolution matrices $\mathbf{E}_n^{[k]}$ are used to identify the subgroups of SZ subjects, we also detect significant differences across subgroups using statistical tests and find clusters of subjects that are robustly grouped together in three scenarios of different values for N_s . The results are summarized in Fig. 6.6 and 6.7.

The identified subgroups of SZ subjects are further verified by comparing the clinical symptoms, which are measured by PANSS scores [108]. There are a total of seven positive, seven negative, and sixteen general scales. A MANOVA is performed on five statistics—mean, standard deviation, median, minimum, and maximum—of all the thirty PANSS. The MANOVA detects significant difference across subgroups for the scenario of $N_s = 6$ with F-score=2.1148 ($p = 0.0012$) when using $\mathbf{C}^{[k]}$ and F-score=1.7942 ($p = 0.0100$) when using $\mathbf{E}_n^{[k]}$. We investigate the correlation between the positive, negative, and general PANSS scores for each subgroup for $N_s = 6$. The subgroups demonstrate different trends in the

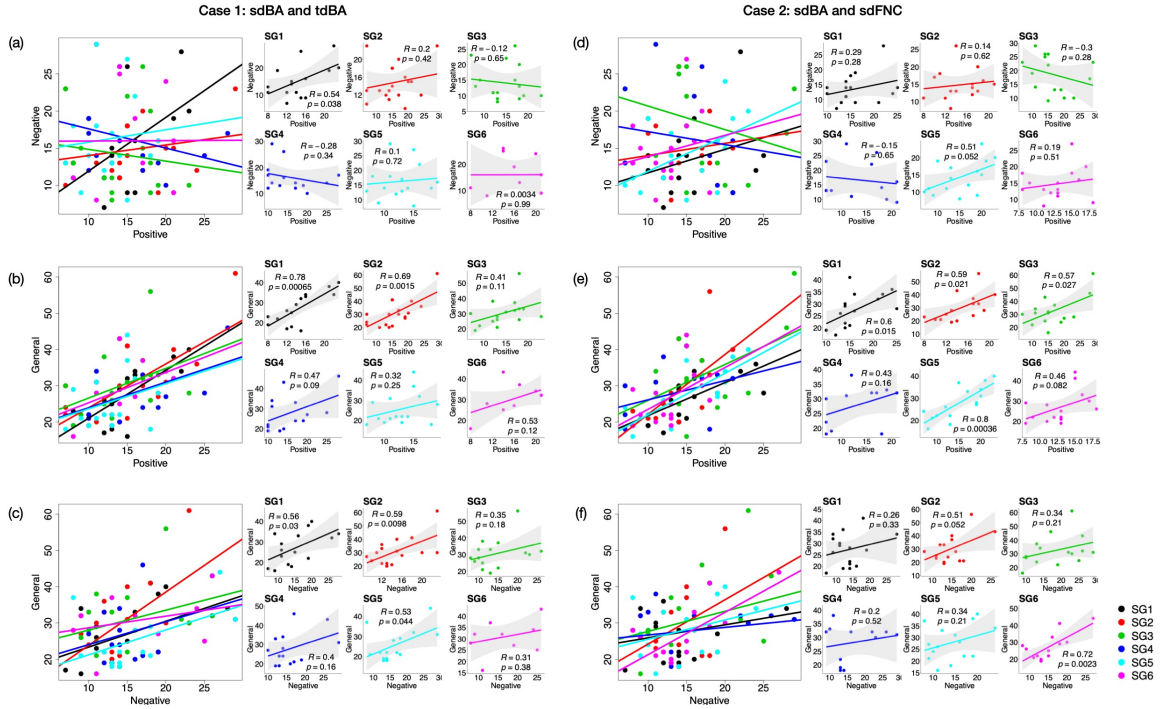


FIG. 6.8. Correlation between the positive, negative, and general PANSS scores for each subgroup when $N_s = 6$ for the case using $\mathbf{C}^{[k]}$ (a)-(c) and $\mathbf{E}_n^{[k]}$ (d)-(f). The large chart plots the data of six subgroups together for a easier visual comparison and the small charts on its right plot the data of individual subgroups with the correlation value and its associated significance level listed.

correlation between the positive and negative PANSS as shown in Fig. 6.8. In the case of $\mathbf{C}^{[k]}$, subgroups 1 and 2 show positive correlation, subgroups 3 and 4 show negative correlation, and the positive and negative PANSS of subgroups 5 and 6 are almost not correlated. Though all subgroups show positive correlation between their positive/negative PANSS and general PANSS, only the correlation of the two subgroups—subgroups 1 and 2—that show positive correlations between their positive and negative PANSS are significant. In the case of $\mathbf{E}_n^{[k]}$, four subgroups show positive correlation between their positive and negative PANSS scores and the other two subgroups show negative correlation. More subgroups show significant positive correlation between their positive and general PANSS than between their negative and general PANSS.

6.5 Summary

Besides the dFNC information that is widely used in dynamic studies, BOLD activity is also shown to be related to mental and cognitive processes in human brain, making a strong case for the desirability of using both BOLD activity and functional connectivity when studying the brain dynamics. We proposed a novel use of a recent method, acIVA, to effectively capture temporal and spatial properties of dBA and to quantify sdBA as part of the algorithm. The efficient quantification of sdBA allows the study of the association between tdBA and sdBA as well as the activity-connectivity co-evolution in spatial domain using sdBA and sdFNC. We conducted a simulation study to demonstrate the adaptive parameter-tuning process in acIVA helps to accurately capture the spatial variabilities and provides a nice metric to efficiently quantify the sdBA. The application of acIVA to the dynamic study of multi-subject resting-state fMRI data showed that dBA demonstrated synchronized patterns in temporal and spatial domains and dBA and dFNC were significantly correlated in spatial domain. SZs showed fewer significantly correlated sdBA and tdBA pairs and favored a complex component that merges multiple brain regions—super parietal, visual, and cerebellum—when compared with HCs, suggesting that the brain function is less efficiently organized in SZ hence more brain regions are simultaneously activated for a certain intrinsic function. In addition, we investigated the effectiveness of dynamic functional features extracted from fMRI in studying the heterogeneity of SZ by identifying unique subgroups of SZ subjects that demonstrate different dynamic patterns using the cross-correlation and co-evolution matrices separately. More importantly, significant differences were detected across the subgroups in terms of their clinical symptoms that are measured by PANSS. This observation again inspires further study of the heterogeneity of mental disorders using neuroimaging modalities such as fMRI.

Chapter 7

CONCLUSIONS AND FUTURE WORK

In this work, we made a number of important developments for the analysis of multi-subject resting-state fMRI data. We studied different forms of diversity used in important data-driven BSS algorithms that are common for fMRI data analysis and developed new methods by leveraging their strengths and addressing the key challenges in the process. In this chapter, we summarize our contributions. Also, we discuss several related directions for future research in multi-subject fMRI data.

7.1 Conclusions

Due to the popularity of using data-driven BSS techniques in extracting interpretable functional brain networks from fMRI data, there are a number of algorithms being developed. Different algorithms make use of different forms of diversity hence are expected to perform differently. However, there is no work performing a fair comparison across algorithms mainly due to the lack of objective metrics for performance assessment. As was discussed in Chapter 3, we provided insight into the comparative advantage of emphasizing one form of diversity over another in the decomposition of multi-subject fMRI data by using group analysis algorithms that assume a common signal space across datasets. Such a comparison is made more difficult due to the differences in the modeling assumptions among different algorithms. We proposed the use of objective global measures, such as

time course frequency power ratio, network connection summary, and graph-theoretical metrics, to gain insight into the role that different types of diversity have on the analysis of fMRI data. Four ICA algorithms that account for different types of diversity in addition of the independence assumption and one DL algorithm that makes use of the sparsity property are studied. We applied these algorithms to the resting-state COBRE data collected from subjects with SZ and a HC group. Our results suggested that no one particular method has the best performance using all metrics, implying that the optimal method will change depending on the goal of the analysis. However, we noted that in none of the scenarios we test the highly popular Infomax provides the best performance, demonstrating the cost of exploiting limited form of diversity.

Unlike the common signal space assumption made in the group analysis algorithms, IVA, another data-driven BSS technique, is developed to extend ICA to the analysis multiple datasets in a more flexible way. IVA makes effective use of dependence across datasets. In Chapter 4, we studied the strengths of IVA-G through a simulation study. IVA-G has a strong identification condition—*i.e.*, the ability to uniquely identify the underlying latent variables—that enables the preservation of subspace structure even by taking only SOS into consideration. IVA-G also provides efficient estimation with reliable convergence due to its desirable analytical properties. By leveraging these strengths of IVA-G, we proposed a new method, IVA-CS, for the subspace analysis of multi-subject fMRI data that is collected from at least a hundred of subjects and addressed the dimensionality issue of IVA. We showed that IVA-G-CS is powerful in discovering the subspace structure and estimating the subspaces through a careful study of the correlation structure of SCVs. The application of IVA-CS to real fMRI data identified interpretable common RSNs of the SZ and HC groups. The identified common components with two linked networks provided evidence of the functional dysconnectivity in the brain of SZs. More importantly, subgroups

of SZ subjects that demonstrate significant differences in terms of their brain networks as well as their clinical symptoms were identified by studying the extracted group-specific RSNs. This finding inspires further study of the heterogeneity of mental disorders using neuroimaging data.

Dynamic study of brain function using fMRI emerges due to the fact that the functional patterns in human brain change over the scanning period of fMRI. One commonly used feature in dynamic study is dFNC that measures the association among different functional networks. GT analysis is shown powerful in quantitatively summarizing the topological characteristics of an adjacent matrix—graph. In Chapter 5, we studied the dynamics of the brain of SZs and HCs by applying acIVA to the resting-state COBRE data to capture both the temporal and spatial variabilities of BOLD signal. We quantitatively studied dFNC using GT analysis and demonstrated that the analysis of sdFNC yielded more distinguishable GT metrics compare with a tdFNC analysis. We showed that the proposed goal-driven scheme, which is the systematic study of global GT metrics in this work, successfully determined the optimal value for the number of sdFNC states in a more interpretable way. The study of nodal GT metrics showed that the centrality is the most interesting GT metric in this application. We found four interesting components that yield interesting GT analysis results. The component that merges multiple brain regions demonstrated increased involvement in the brain function of SZs compared with HCs, illustrating the dysconnectivity of SZ brain. The two components that are parts of the cognitive network had higher values of centrality in HC group, potentially suggesting a more efficient cognitive control system in the brain of HCs.

Due to the fact that both the BOLD activity and FNC are related to mental and cognitive processes, it is desirable to investigate the activity-connectivity co-evolution of dBA and dFNC to gain a better interpretation of the dynamics in human brain. In Chapter 6,

we introduced our work of studying the activity-connectivity co-evolution in spatial domain using sdBA and sdfNC. We proposed the novel use of acIVA to efficiently quantify sdBA as a part of the algorithm along with its powerful ability to capture dynamics in both temporal and spatial domains. The efficient quantification of sdBA allows the study of the association between tdBA and sdBA as well as the activity-connectivity co-evolution in spatial domain using sdBA and sdfNC. We first conducted a simulation study to demonstrate that the adaptive parameter-tuning process in acIVA helps accurately capture the spatial variabilities and provides a nice metric to efficiently quantify the sdBA. The application of acIVA to the resting-state COBRE data showed that tdBA and sdBA pairs of the same functional network had higher correlation than those of different networks, and sdBA yielded higher correlation with the network connectivity that are associated with the same network. However, SZs showed fewer significantly correlated sdBA and tdBA pairs and favored a complex component that merges multiple brain regions—super parietal, visual, and cerebellum—when compared with HCs, suggesting that the brain function is less efficiently organized in SZ hence more brain regions are simultaneously activated for a certain intrinsic function. Most importantly, we identified subgroups of SZ using the tdBA-sdBA association and the sdBA-sdfNC co-evolution, and detected significant differences across subgroups in terms of their clinical symptoms that are measured by PANSS. This observation again inspires the study of the heterogeneity of mental disorders using neuroimaging modalities such as fMRI.

7.2 Future directions

The development of effective methods for the analysis of multi-subject fMRI data in this work motivates several promising directions for future research.

7.2.1 Full automation of IVA-CS

IVA-CS is shown to be powerful in subspace analysis of multi-subject fMRI data especially in identifying subgroups of subjects. Others have shown interest in applying IVA-CS to other datasets to find meaningful subgroups. As was introduced in Chapter 4.3, the identification of subgroups, starting with the dividing of three subspaces from IVA-G decomposition results, involves a set of user determined parameters. The use of these parameters potentially limits the generalization of IVA-CS. It is desirable to improve the subgroup identification process to make it as automatic as possible, hence it is easier to be used in other applications. We propose a pipeline as shown in Fig. 7.1 that reduces the number of parameters and identifies the subgroups of subjects using a clustering method instead of the modularization-permutation approach. The process starts from the IVA-G decomposition results. First, we compute the commonality q for each SCV. SCVs with $q = 1$ span the common subspace and SCVs with $q < q_0$ refers to the distinct components. We concentrate on the N_G SCVs with $q_0 \leq q < 1$ and perform a k-means clustering on them with the number of clusters being $\text{round}(N_G/3)$, allowing a relatively small number of components to be clustered together on average. Another k-means clustering is performed on the mean correlation matrix of each cluster by using each row as a feature for each subject to find the subgroups of subject. The number of subgroups will be determined using the elbow criterion.

Compared with the method described in Chapter 4.3 that requires a set of parameters, including correlation threshold t , σ_t^2 , δ_1 , δ_2 , and some percentage values, and so on, in the improved method, the users only need to determine the values of σ_t^2 and q_0 . In the example shown in Fig. 7.1, $\sigma_t^2 = 0.2$ and $q_0 = 0.6$. The determination of σ_t^2 and q_0 is highly related with the correlation level across datasets.

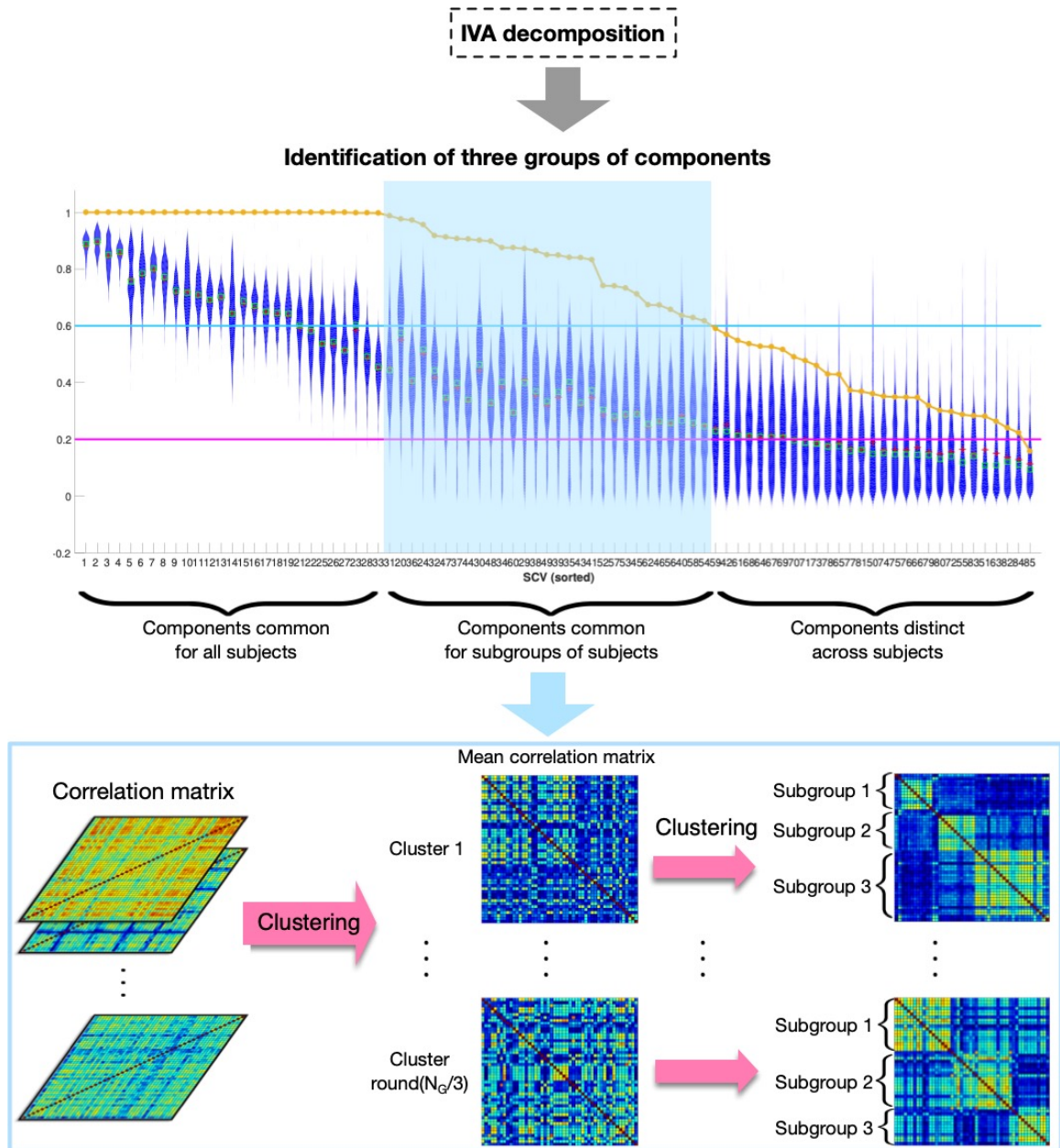


FIG. 7.1. Improved method for the identification of subgroups of subjects.

7.2.2 Subspace study across multiple groups/tasks/modalities

Studies that make use of the data collected from subjects of multiple groups when they are doing different tasks by using different techniques is common. In medical imaging data analysis such as neuroimaging data, studying the data of multiple groups enables us to gain

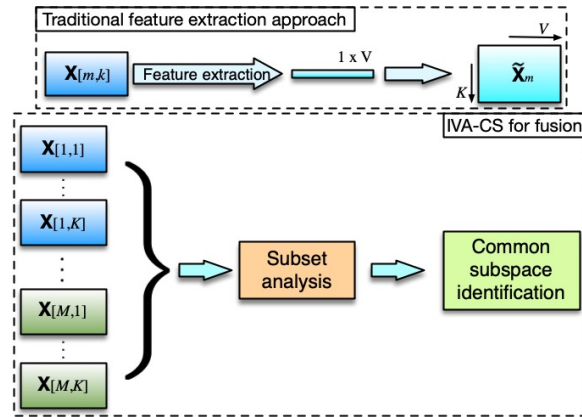


FIG. 7.2. IVA for joint study of multi-group/multi-task/multimodal data. Note that M denotes the number of groups/tasks/modalities, K denotes the number of datasets in each group/task/modality, and V denotes the sample number.

a better understanding of the connection and similarity of them as well as the uniqueness of each population. A joint analysis of the neuroimaging data of a subject collected when he is doing different tasks helps us to better interpret the functional patterns of his brain. Multi-modal data collected using different techniques is expected to provide complementary information that will benefit the extraction of useful details from the data. This forms an important research domain—data fusion—where the researchers develop effective algorithms that can jointly analyze multi-group, multi-task, and/or multi-modal neuroimaging data.

Among the data fusion techniques, many aim at extracting common and distinct subspaces of the data collected from multiple groups/tasks/modalities [5, 114, 135, 161, 176, 184]. However, most of these methods are suitable for a small number of datasets, which typically equals to the number of groups/tasks/modalities. To deal with the data collected from a large number of subjects, different kinds of features are extracted for individual subjects to form a single dataset for each group/task/modality [8, 174], as shown in Fig. 7.2. The performance of these methods therefore are highly dependent on the quality of

the extracted features. Reducing the original data from the dimensionality of hundreds to a one-dimensional feature is a rough process that might disregard a great deal of useful information.

IVA-CS, as was introduced in Chapter 4, is demonstrated to be able to jointly analyze a large number of datasets and powerful in identifying their common subspace without doing feature extraction. This makes it possible to make full use of the data collected from a large number of subjects of different groups, different tasks, and/or different modalities. Therefore, another possibility of the future work is to apply the proposed IVA-CS to the joint study of a large number of datasets with original dimensionality collected from multiple groups, tasks, and/or different modalities.

7.2.3 Subspace analysis of task-evoked fMRI data

Task-evoked neuroimaging modalities such as fMRI are also important in gaining a better understanding of the human brain. In the scenario where the fMRI data is acquired when the participants are doing a certain task and there are a number of stimuli involved in the task, it is possible to break down the problem into a number of subspaces. Each of these subspaces highly associates with a specific stimulus. For example, in the auditory odd-ball task fMRI data, there are three stimuli, the standard tone, the novel tone, and the target tone. We first perform a transposed IVA with a small model order N on the original multi-subject fMRI data. Among the N estimated independent temporal signals, we find three that are the highest correlated with the three stimuli. The corresponding back-reconstructed spatial maps are expected to merge multiple brain regions. The merged brain regions in each spatial map refer to the functional networks that are mostly associated with the brain function that is evoked by each stimulus. We then multiply the spatial maps with their corresponding temporal signal for each subject, yielding the subspaces that are mostly associated with the stimuli. Post-analysis such as individual IVA decompositions

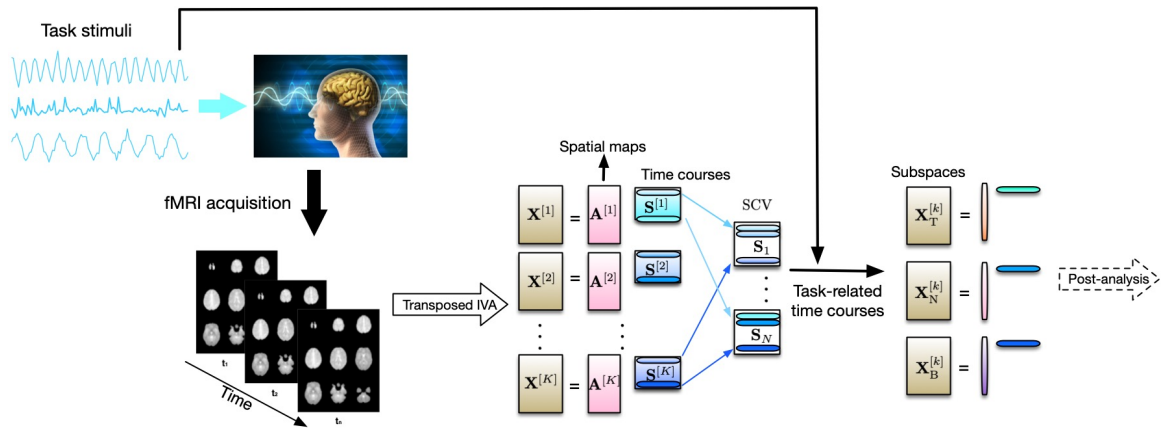


FIG. 7.3. Transposed IVA model for task subspaces extraction using task-evoked fMRI data.

can be performed on each subspace to extract both the temporal and spatial variabilities of BOLD and study the BOLD activity and FNC information that is only evoked by a specific stimulus.

REFERENCES

- [1] V. Abolghasemi, S. Ferdowsi, and S. Sanei. Fast and incoherent dictionary learning algorithms with application to fMRI. *Signal, Image and Video Processing*, 9(1):147–158, 2015.
- [2] A. Abou-Elseoud, T. Starck, J. Remes, J. Nikkinen, O. Tervonen, and V. Kiviniemi. The effect of model order selection in group pica. *Human brain mapping*, 31(8):1207–1216, 2010.
- [3] A. Abraham, E. Dohmatob, B. Thirion, D. Samaras, and G. Varoquaux. Extracting brain regions from rest fMRI with total-variation constrained dictionary learning. In *International Conference on Medical Image Computing and Computer-Assisted Intervention*, pages 607–615, 2013.
- [4] T. Adalı, M. Anderson, and G.-S. Fu. Diversity in independent component and vector analyses: Identifiability, algorithms, and applications in medical imaging. *IEEE Signal Processing Magazine*, 31(3):18–33, May 2014.
- [5] T. Adalı, Y. Levin-Schwartz, and V. D. Calhoun. Multi-modal data fusion using source separation: Application to medical imaging. *Proceedings of the IEEE*, 103(9):1494 – 1506, 2015.
- [6] T. Adalı, Y. Levin-Schwartz, and V. D. Calhoun. Multi-modal data fusion using source separation: Two effective models based on ICA and IVA and their properties. *Proceedings of the IEEE*, 103(9):1478 – 1493, 2015.
- [7] C. Aine, H. Bockholt, J. Bustillo, J. Cañive, A. Caprihan, C. Gasparovic, F. Hanlon,

- J. Houck, R. Jung, J. Lauriello, et al. Multimodal neuroimaging in schizophrenia: Description and dissemination. *Neuroinformatics*, 15(4):343–364, 2017.
- [8] M. A. Akhonda, Y. Levin-Schwartz, S. Bhinge, V. D. Calhoun, and T. Adali. Consecutive independence and correlation transform for multimodal fusion: Application to EEG and fMRI data. In *2018 IEEE International Conference on Acoustics, Speech and Signal Processing (ICASSP)*, pages 2311–2315. IEEE, 2018.
- [9] A. F. Alexander-Bloch, N. Gogtay, D. Meunier, R. Birn, L. Clasen, F. Lalonde, R. Lenroot, J. Giedd, and E. T. Bullmore. Disrupted modularity and local connectivity of brain functional networks in childhood-onset schizophrenia. *Frontiers in Systems Neuroscience*, 4, 2010.
- [10] E. A. Allen, E. Damaraju, S. M. Plis, E. B. Erhardt, T. Eichele, and V. D. Calhoun. Tracking whole-brain connectivity dynamics in the resting state. *Cerebral Cortex*, 24(3):663–676, 2014.
- [11] E. A. Allen, E. B. Erhardt, E. Damaraju, W. Gruner, J. M. Segall, R. F. Silva, M. Havlicek, S. Rachakonda, J. Fries, R. Kalyanam, et al. A baseline for the multivariate comparison of resting-state networks. *Frontiers in Systems Neuroscience*, 5:2, 2011.
- [12] S. Amari, A. Cichocki, and H. H. Yang. A new learning algorithm for blind signal separation. In *Advances in Neural Information Processing Systems*, volume 8, pages 757–763, Cambridge, MA, 1996. MIT Press.
- [13] S.-i. Amari. Estimating functions of independent component analysis for temporally correlated signals. *Neural Computation*, 12(9):2083–2107, Sep. 2000.

- [14] M. Anderson, T. Adalı, and X.-L. Li. Joint blind source separation with multivariate Gaussian model: Algorithms and performance analysis. *IEEE Transactions on Signal Processing*, 60(4):1672–1683, April 2012.
- [15] M. Anderson, G.-S. Fu, R. Phlypo, and T. Adalı. Independent vector analysis, the Kotz distribution, and performance bounds. In *2013 IEEE International Conference on Acoustics, Speech and Signal Processing (ICASSP)*, pages 3243–3247, 2013.
- [16] M. Anderson, G.-S. Fu, R. Phlypo, and T. Adalı. Independent vector analysis: Identification conditions and performance bounds. *IEEE Transactions on Signal Processing*, 62(17):4399–4410, Sep. 2014.
- [17] C. Arango, B. Kirkpatrick, and R. W. Buchanan. Neurological signs and the heterogeneity of schizophrenia. *American Journal of Psychiatry*, 157(4):560–565, 2000.
- [18] M. Assaf, K. Jagannathan, V. D. Calhoun, L. Miller, M. C. Stevens, R. Sahl, J. G. O’Boyle, R. T. Schultz, and G. D. Pearlson. Abnormal functional connectivity of default mode sub-networks in autism spectrum disorder patients. *NeuroImage*, 53(1):247–256, 2010.
- [19] M. Baiano, A. David, A. Versace, R. Churchill, M. Balestrieri, and P. Brambilla. Anterior cingulate volumes in schizophrenia: A systematic review and a meta-analysis of MRI studies. *Schizophrenia Research*, 93(1-3):1–12, 2007.
- [20] S. J. Banks, K. T. Eddy, M. Angstadt, P. J. Nathan, and K. L. Phan. Amygdala–frontal connectivity during emotion regulation. *Social cognitive and affective neuroscience*, 2(4):303–312, 2007.
- [21] D. S. Bassett, B. G. Nelson, B. A. Mueller, J. Camchong, and K. O. Lim. Altered resting state complexity in schizophrenia. *NeuroImage*, 59(3):2196–2207, 2012.

- [22] C. F. Beckmann, C. E. Mackay, N. Filippini, and S. M. Smith. Group comparison of resting-state fMRI data using multi-subject ICA and dual regression. *NeuroImage*, 47(Suppl 1):S148, 2009.
- [23] A. Bell and T. Sejnowski. An information maximization approach to blind separation and blind deconvolution. *Neural Computation*, 7:1129–1159, 1995.
- [24] K. Bhaganagarapu, G. D. Jackson, and D. F. Abbott. An automated method for identifying artifact in independent component analysis of resting-state fMRI. *Frontiers in Human Neuroscience*, 7:343, 2013.
- [25] S. Bhinge, Q. Long, V. D. Calhoun, and T. Adali. Spatial dynamic functional connectivity analysis identifies distinctive biomarkers in schizophrenia. *Frontiers in neuroscience*, 13, 2019.
- [26] S. Bhinge, Q. Long, Y. Levin-Schwartz, Z. Boukouvalas, V. D. Calhoun, and T. Adali. Non-orthogonal constrained independent vector analysis: Application to data fusion. In *Acoustics, Speech and Signal Processing (ICASSP), 2017 IEEE International Conference on*, pages 2666–2670, 2017.
- [27] S. Bhinge, R. Mowakeaa, V. D. Calhoun, and T. Adali. Extraction of time-varying spatiotemporal networks using parameter-tuned constrained IVA. *IEEE Transactions on Medical Imaging*, 38(7):1715–1725, 2019.
- [28] B. B. Biswal, M. Mennes, X.-N. Zuo, S. Gohel, C. Kelly, S. M. Smith, C. F. Beckmann, J. S. Adelstein, R. L. Buckner, S. Colcombe, et al. Toward discovery science of human brain function. *Proceedings of the National Academy of Sciences*, 107(10):4734–4739, 2010.

- [29] R. L. Bluhm, J. Miller, R. A. Lanius, E. A. Osuch, K. Boksman, R. Neufeld, J. Théberge, B. Schaefer, and P. Williamson. Spontaneous low-frequency fluctuations in the BOLD signal in schizophrenic patients: Anomalies in the default network. *Schizophrenia Bulletin*, 33(4):1004–1012, 2007.
- [30] R. L. Bluhm, P. C. Williamson, E. A. Osuch, P. A. Frewen, T. K. Stevens, K. Boksman, R. W. Neufeld, J. Théberge, and R. A. Lanius. Alterations in default network connectivity in posttraumatic stress disorder related to early-life trauma. *Journal of Psychiatry & Neuroscience: JPN*, 34(3):187, 2009.
- [31] S. Boccaletti, V. Latora, Y. Moreno, M. Chavez, and D.-U. Hwang. Complex networks: Structure and dynamics. *Physics Reports*, 424(4):175–308, 2006.
- [32] P. Bonacich. Power and centrality: A family of measures. *American Journal of Sociology*, 92(5):1170–1182, 1987.
- [33] P. Bonacich. Some unique properties of eigenvector centrality. *Social Networks*, 29(4):5, 2007.
- [34] Z. Boukouvalas, G.-S. Fu, and T. Adalı. An efficient multivariate generalized Gaussian distribution estimator: Application to IVA. In *2015 49th Annual Conference on Information Sciences and Systems (CISS)*, pages 1–4, 2015.
- [35] Z. Boukouvalas, Y. Levin-Schwartz, and T. Adalı. Enhancing ICA performance by exploiting sparsity: Application to fMRI analysis. In *Acoustics, Speech and Signal Processing (ICASSP), 2017 IEEE International Conference on*, pages 2532–2536, 2017.
- [36] Z. Boukouvalas, Y. Levin-Schwartz, V. D. Calhoun, and T. Adalı. Sparsity and

- independence: Balancing two objectives in optimization for source separation with application to fMRI analysis. *Journal of the Franklin Institute*, 2017.
- [37] J. Britz, T. Landis, and C. M. Michel. Right parietal brain activity precedes perceptual alternation of bistable stimuli. *Cerebral Cortex*, 19(1):55–65, 2009.
- [38] E. Bullmore, S. Frangou, and R. Murray. The dysplastic net hypothesis: An integration of developmental and dysconnectivity theories of schizophrenia. *Schizophrenia Research*, 28(2):143–156, 1997.
- [39] E. Bullmore and O. Sporns. Complex brain networks: Graph theoretical analysis of structural and functional systems. *Nature Reviews Neuroscience*, 10(3):186–198, 2009.
- [40] E. T. Bullmore and D. S. Bassett. Brain graphs: Graphical models of the human brain connectome. *Annual Review of Clinical Psychology*, 7:113–140, 2011.
- [41] E. T. Bullmore, J. Suckling, S. Overmeyer, S. Rabe-Hesketh, E. Taylor, and M. J. Brammer. Global, voxel, and cluster tests, by theory and permutation, for a difference between two groups of structural MR images of the brain. *IEEE Transactions on Medical Imaging*, 18(1):32–42, 1999.
- [42] C. C Abbott, A. Jaramillo, C. E Wilcox, and D. A Hamilton. Antipsychotic drug effects in schizophrenia: a review of longitudinal fmri investigations and neural interpretations. *Current medicinal chemistry*, 20(3):428–437, 2013.
- [43] V. Calhoun, M. Stevens, G. Pearlson, and K. Kiehl. fmri analysis with the general linear model: removal of latency-induced amplitude bias by incorporation of hemodynamic derivative terms. *Neuroimage*, 22(1):252–257, 2004.

- [44] V. D. Calhoun and T. Adalı. Unmixing fMRI with independent component analysis. *IEEE Engineering in Medicine and Biology Magazine*, 25(2):79–90, 2006.
- [45] V. D. Calhoun and T. Adalı. Feature-based fusion of medical imaging data. *IEEE Transactions on Information Technology in Biomedicine*, 13(5):711–720, Sep. 2009.
- [46] V. D. Calhoun and T. Adalı. Multisubject independent component analysis of fMRI: A decade of intrinsic networks, default mode, and neurodiagnostic discovery. *IEEE Reviews in Biomedical Engineering*, 5:60–73, 2012.
- [47] V. D. Calhoun, T. Adalı, G. Pearlson, and K. Kiehl. Neuronal chronometry of target detection: Fusion of hemodynamic and event related potential data. *NeuroImage*, 30:544–553, 2006.
- [48] V. D. Calhoun, T. Adalı, G. D. Pearlson, and J. J. Pekar. A method for making group inferences from functional MRI data using independent component analysis. *Human Brain Mapping*, 14(3):140–151, 2001.
- [49] V. D. Calhoun, T. Eichele, and G. Pearlson. Functional brain networks in schizophrenia: A review. *Frontiers in Human Neuroscience*, 3:17, 2009.
- [50] V. D. Calhoun, J. Liu, and T. Adalı. A review of group ICA for fMRI data and ICA for joint inference of imaging, genetic, and ERP data. *NeuroImage*, 45(1):S163–S172, 2009.
- [51] V. D. Calhoun, R. Miller, G. Pearlson, and T. Adalı. The chronnectome: Time-varying connectivity networks as the next frontier in fMRI data discovery. *Neuron*, 84(2):262–274, 2014.

- [52] V. D. Calhoun, J. J. Pekar, and G. D. Pearlson. Alcohol intoxication effects on simulated driving: Exploring alcohol-dose effects on brain activation using functional MRI. *Neuropsychopharmacology*, 29(11):2097–2107, 2004.
- [53] V. D. Calhoun, V. K. Potluru, R. Rhlypo, R. F. Silva, B. A. Pearlmutter, A. Caprihan, S. M. Plis, and T. Adalı. Independent component analysis for brain fMRI does indeed select for maximal independence. *PLoS ONE*, 8(10):e73309, 2013.
- [54] J. H. Callicott, A. Bertolino, V. S. Mattay, F. J. Langheim, J. Duyn, R. Coppola, T. E. Goldberg, and D. R. Weinberger. Physiological dysfunction of the dorsolateral prefrontal cortex in schizophrenia revisited. *Cerebral cortex*, 10(11):1078–1092, 2000.
- [55] J. H. Callicott, V. S. Mattay, B. A. Verchinski, S. Marenco, M. F. Egan, and D. R. Weinberger. Complexity of prefrontal cortical dysfunction in schizophrenia: more than up or down. *American Journal of Psychiatry*, 160(12):2209–2215, 2003.
- [56] C. S. Carter, W. Perlstein, R. Ganguli, J. Brar, M. Mintun, and J. D. Cohen. Functional hypofrontality and working memory dysfunction in schizophrenia. *American Journal of Psychiatry*, 155(9):1285–1287, 1998.
- [57] M. S. Çetin, F. Christensen, C. C. Abbott, J. M. Stephen, A. R. Mayer, J. M. Cañive, J. R. Bustillo, G. D. Pearlson, and V. D. Calhoun. Thalamus and posterior temporal lobe show greater inter-network connectivity at rest and across sensory paradigms in schizophrenia. *NeuroImage*, 97:117 – 126, 2014.
- [58] C. Chang and G. H. Glover. Time–frequency dynamics of resting-state brain connectivity measured with fmri. *Neuroimage*, 50(1):81–98, 2010.

- [59] D. M. Cole, S. M. Smith, and C. F. Beckmann. Advances and pitfalls in the analysis and interpretation of resting-state fmri data. *Frontiers in systems neuroscience*, 4:8, 2010.
- [60] D. Cordes, V. M. Haughton, K. Arfanakis, J. D. Carew, P. A. Turski, C. H. Moritz, M. A. Quigley, and M. E. Meyerand. Frequencies contributing to functional connectivity in the cerebral cortex in resting-state data. *American Journal of Neuroradiology*, 22(7):1326–1333, 2001.
- [61] N. Correa, T. Adalı, and V. D. Calhoun. Performance of blind source separation algorithms for fMRI analysis using a group ICA method. *Magnetic Resonance Imaging*, 25(5):684–694, 2007.
- [62] E. Damaraju, E. A. Allen, A. Belger, J. Ford, S. McEwen, D. Mathalon, B. Mueller, G. Pearlson, S. Potkin, A. Preda, et al. Dynamic functional connectivity analysis reveals transient states of dysconnectivity in schizophrenia. *NeuroImage: Clinical*, 5:298–308, 2014.
- [63] I. Daubechies, E. Roussos, S. Takerkart, M. Benharrosh, C. Golden, K. D’Ardenne, W. Richter, J. D. Cohen, and J. Haxby. Independent component analysis for brain fMRI does not select for independence. *Proceedings of the National Academy of Sciences*, 106(26):10415–10422, 2009.
- [64] O. Demirci, M. C. Stevens, N. C. Andreasen, A. Michael, J. Liu, T. White, G. D. Pearlson, V. P. Clark, and V. D. Calhoun. Investigation of relationships between fMRI brain networks in the spectral domain using ICA and Granger causality reveals distinct differences between schizophrenia patients and healthy controls. *NeuroImage*, 46(2):419–431, 2009.

- [65] K. Dontaraju, S.-J. Kim, M. Akhonda, and T. Adalı. Capturing common and individual components in fMRI data by discriminative dictionary learning. In *2018 52nd Asilomar Conference on Signals, Systems, and Computers*, pages 1351–1356, 2018.
- [66] W. Du, Y. Levin-Schwartz, G.-S. Fu, S. Ma, V. D. Calhoun, and T. Adalı. The role of diversity in complex ICA algorithms for fMRI analysis. *Journal of Neuroscience Methods*, 264:129–135, 2016.
- [67] W. Du, H. Li, X.-L. Li, V. D. Calhoun, and T. Adalı. ICA of fMRI data: Performance of three ICA algorithms and the importance of taking correlation information into account. In *2011 IEEE International Symposium on Biomedical Imaging: From Nano to Macro*, pages 1573–1576, April 2011.
- [68] Y. Du, D. Lin, Q. Yu, J. Sui, J. Chen, S. Rachakonda, T. Adalı, and V. D. Calhoun. Comparison of IVA and GIG-ICA in brain functional network estimation using fMRI data. *Frontiers in Neuroscience*, 11, 2017.
- [69] D. B. Dwyer, C. Cabral, L. Kambeitz-Illankovic, R. Sanfelici, J. Kambeitz, V. Calhoun, P. Falkai, C. Pantelis, E. Meisenzahl, and N. Koutsouleris. Brain subtyping enhances the neuroanatomical discrimination of schizophrenia. *Schizophrenia Bulletin*, 44(5):1060–1069, 2018.
- [70] A. M. Engberg, K. W. Andersen, M. Mørup, and K. H. Madsen. Independent vector analysis for capturing common components in fMRI group analysis. In *Pattern Recognition in Neuroimaging (PRNI), 2016 International Workshop on*, pages 1–4, 2016.
- [71] E. B. Erhardt, S. Rachakonda, E. J. Bedrick, E. A. Allen, T. Adalı, and V. D. Cal-

- houn. Comparison of multi-subject ICA methods for analysis of fMRI data. *Human Brain Mapping*, 32(12):2075–2095, 2011.
- [72] A. Etkin, K. E. Prater, A. F. Schatzberg, V. Menon, and M. D. Greicius. Disrupted amygdalar subregion functional connectivity and evidence of a compensatory network in generalized anxiety disorder. *Archives of General Psychiatry*, 66(12):1361–1372, 2009.
- [73] L. Freire, A. Roche, and J.-F. Mangin. What is the best similarity measure for motion correction in fMRI time series? *IEEE Transactions on Medical Imaging*, 21(5):470–484, 2002.
- [74] K. J. Friston. Schizophrenia and the disconnection hypothesis. *Acta Psychiatrica Scandinavica*, 99:68–79, 1999.
- [75] K. J. Friston, A. P. Holmes, J. Poline, P. Grasby, S. Williams, R. S. Frackowiak, R. Turner, et al. Analysis of fmri time-series revisited. *Neuroimage*, 2(1):45–53, 1995.
- [76] K. J. Friston, A. P. Holmes, K. J. Worsley, J. P. Poline, C. D. Frith, and R. S. J. Frackowiak. Statistical parametric maps in functional imaging: A general linear approach. *Human Brain Mapping*, 2(4):189–210, 1994.
- [77] K. J. Friston, P. Jezzard, and R. Turner. Analysis of functional mri time-series. *Human brain mapping*, 1(2):153–171, 1994.
- [78] G.-S. Fu, M. Anderson, and T. Adalı. Likelihood estimators for dependent samples and their application to order detection. *IEEE Transactions on Signal Processing*, 62(16):4237–4244, Aug. 2014.

- [79] Z. Fu, Y. Du, and V. D. Calhoun. The dynamic functional network connectivity analysis framework. *Engineering*, 5(2):190–193, 2019.
- [80] Z. Fu, Y. Tu, X. Di, Y. Du, G. D. Pearlson, J. A. Turner, B. B. Biswal, Z. Zhang, and V. D. Calhoun. Characterizing dynamic amplitude of low-frequency fluctuation and its relationship with dynamic functional connectivity: An application to schizophrenia. *NeuroImage*, 180:619–631, 2018.
- [81] Z. Fu, Y. Tu, X. Di, Y. Du, J. Sui, B. B. Biswal, Z. Zhang, N. de Lacy, and V. D. Calhoun. Transient increased thalamic-sensory connectivity and decreased whole-brain dynamism in autism. *NeuroImage*, 190:191–204, 2019.
- [82] D. Geisler, E. Walton, M. Naylor, V. Roessner, K. O. Lim, S. C. Schulz, R. L. Gollub, V. D. Calhoun, S. R. Sponheim, and S. Ehrlich. Brain structure and function correlates of cognitive subtypes in schizophrenia. *Psychiatry Research: Neuroimaging*, 234(1):74–83, 2015.
- [83] M. N. Goria, N. N. Leonenko, V. V. Mergel, and P. L. Novi Inverardi. A new class of random vector entropy estimators and its applications in testing statistical hypotheses. *Journal of Nonparametric Statistics*, 17(3):277–297, 2005.
- [84] M. D. Greicius, B. Krasnow, A. L. Reiss, and V. Menon. Functional connectivity in the resting brain: A network analysis of the default mode hypothesis. *Proceedings of the National Academy of Sciences*, 100(1):253–258, 2003.
- [85] C. C. Guo, F. Kurth, J. Zhou, E. A. Mayer, S. B. Eickhoff, J. H. Kramer, and W. W. Seeley. One-year test–retest reliability of intrinsic connectivity network fmri in older adults. *Neuroimage*, 61(4):1471–1483, 2012.

- [86] Y. Guo and L. Tang. A hierarchical model for probabilistic independent component analysis of multi-subject fMRI studies. *Biometrics*, 69(4):970–981, 2013.
- [87] R. E. Gur, P. E. Cowell, A. Latshaw, B. I. Turetsky, R. I. Grossman, S. E. Arnold, W. B. Bilker, and R. C. Gur. Reduced dorsal and orbital prefrontal gray matter volumes in schizophrenia. *Archives of General Psychiatry*, 57(8):761–768, 2000.
- [88] B. Hahn, B. M. Robinson, C. J. Leonard, S. J. Luck, and J. M. Gold. Posterior parietal cortex dysfunction is central to working memory storage and broad cognitive deficits in schizophrenia. *Journal of Neuroscience*, 38(39):8378–8387, 2018.
- [89] J. F. Hallmayer, L. Kalaydjieva, J. Badcock, M. Dragović, S. Howell, P. T. Michie, D. Rock, D. Vile, R. Williams, E. H. Corder, et al. Genetic evidence for a distinct subtype of schizophrenia characterized by pervasive cognitive deficit. *The American Journal of Human Genetics*, 77(3):468–476, 2005.
- [90] C. He, Y. Chen, T. Jian, H. Chen, X. Guo, J. Wang, L. Wu, H. Chen, and X. Duan. Dynamic functional connectivity analysis reveals decreased variability of the default-mode network in developing autistic brain. *Autism Research*, 11(11):1479–1493, 2018.
- [91] M. J. Hoptman, X.-N. Zuo, P. D. Butler, D. C. Javitt, D. D’Angelo, C. J. Mauro, and M. P. Milham. Amplitude of low-frequency oscillations in schizophrenia: R resting state fMRI study. *Schizophrenia Research*, 117(1):13–20, 2010.
- [92] N. Hurley and S. Rickard. Comparing measures of sparsity. *IEEE Transactions on Information Theory*, 55(10):4723–4741, Oct. 2009.
- [93] R. M. Hutchison and J. B. Morton. It’s a matter of time: Reframing the development

- of cognitive control as a modification of the brain's temporal dynamics. *Developmental Cognitive Neuroscience*, 18:70–77, 2016.
- [94] R. M. Hutchison, T. Womelsdorf, E. A. Allen, P. A. Bandettini, V. D. Calhoun, M. Corbetta, S. Della Penna, J. H. Duyn, G. H. Glover, J. Gonzalez-Castillo, et al. Dynamic functional connectivity: promise, issues, and interpretations. *Neuroimage*, 80:360–378, 2013.
- [95] R. M. Hutchison, T. Womelsdorf, J. S. Gati, S. Everling, and R. S. Menon. Resting-state networks show dynamic functional connectivity in awake humans and anesthetized macaques. *Human brain mapping*, 34(9):2154–2177, 2013.
- [96] A. Hyvärinen, J. Karhunen, and E. Oja. *Independent Component Analysis*. John Wiley & Sons, Inc., 2001.
- [97] A. Iqbal, A.-K. Seghouane, and T. Adalı. Shared and subject-specific dictionary learning (ShSSDL) algorithm for multisubject fMRI data analysis. *IEEE Transactions on Biomedical Engineering*, 65(11):2519–2528, 2018.
- [98] A. Irajı, T. P. Deramus, N. Lewis, M. Yaesoubi, J. M. Stephen, E. Erhardt, A. Belger, J. M. Ford, S. McEwen, D. H. Mathalon, et al. The spatial chronnectome reveals a dynamic interplay between functional segregation and integration. *Human Brain Mapping*, 40(10):3058–3077, 2019.
- [99] A. Irajı, Z. Fu, E. Damaraju, T. P. DeRamus, N. Lewis, J. R. Bustillo, R. K. Lenroot, A. Belger, J. M. Ford, S. McEwen, et al. Spatial dynamics within and between brain functional domains: A hierarchical approach to study time-varying brain function. *Human Brain Mapping*, 40(6):1969–1986, 2019.

- [100] A. Iraj, R. Miller, T. Adali, and V. D. Calhoun. Space: A missing piece of the dynamic puzzle. *Trends in Cognitive Sciences*, 24(2):135–149, 2020.
- [101] A. Jablensky. Subtyping schizophrenia: Implications for genetic research. *Molecular Psychiatry*, 11(9):815, 2006.
- [102] A. Jablensky. The diagnostic concept of schizophrenia: Its history, evolution, and future prospects. *Dialogues in Clinical Neuroscience*, 12(3):271, 2010.
- [103] M. J. Jafri, G. D. Pearlson, M. Stevens, and V. D. Calhoun. A method for functional network connectivity among spatially independent resting-state components in schizophrenia. *NeuroImage*, 39(4):1666 – 1681, 2008.
- [104] G. Jager, M. M. De Win, I. Van Der Tweel, T. Schilt, R. S. Kahn, W. Van Den Brink, J. M. Van Ree, and N. F. Ramsey. Assessment of cognitive brain function in ecstasy users and contributions of other drugs of abuse: results from an fmri study. *Neuropsychopharmacology*, 33(2):247–258, 2008.
- [105] B. Jie, M. Liu, and D. Shen. Integration of temporal and spatial properties of dynamic connectivity networks for automatic diagnosis of brain disease. *Medical image analysis*, 47:81–94, 2018.
- [106] O. Josephs, R. Turner, and K. Friston. Event-related f mri. *Human brain mapping*, 5(4):243–248, 1997.
- [107] N. Kanahara, Y. Sekine, T. Haraguchi, Y. Uchida, K. Hashimoto, E. Shimizu, and M. Iyo. Orbitofrontal cortex abnormality and deficit schizophrenia. *Schizophrenia Research*, 143(2-3):246–252, 2013.
- [108] S. R. Kay, A. Fiszbein, and L. A. Opler. The positive and negative syndrome scale (PANSS) for schizophrenia. *Schizophrenia Bulletin*, 13(2):261–276, 1987.

- [109] A. C. Kelly, L. Q. Uddin, B. B. Biswal, F. X. Castellanos, and M. P. Milham. Competition between functional brain networks mediates behavioral variability. *Neuroimage*, 39(1):527–537, 2008.
- [110] J. R. Kettenring. Canonical analysis of several sets of variables. *Biometrika*, 58(3):433–451, 1971.
- [111] T. Kim, T. Eltoft, and T.-W. Lee. Independent vector analysis: An extension of ica to multivariate components. In *International Conference on Independent Component Analysis and Signal Separation*, pages 165–172. 2006.
- [112] T. Kim, I. Lee, and T.-W. Lee. Independent vector analysis: Definition and algorithms. In *Proc. of 40th Asilomar Conference on Signals, Systems, and Computers*, pages 1393–1396, Oct. 2006.
- [113] V. Kiviniemi, T. Starck, J. Remes, X. Long, J. Nikkinen, M. Haapea, J. Veijola, I. Moilanen, M. Isohanni, Y.-F. Zang, et al. Functional segmentation of the brain cortex using high model order group PICA. *Human Brain Mapping*, 30(12):3865–3886, 2009.
- [114] A. Klami, S. Virtanen, and S. Kaski. Bayesian canonical correlation analysis. *Journal of Machine Learning Research*, 14(Apr):965–1003, 2013.
- [115] R. Kohavi. A study of cross-validation and bootstrap for accuracy estimation and model selection. In *International Joint Conference on Artificial Intelligence (IJCAI), 1995*, volume 14, pages 1137–1145, 1995.
- [116] A. Kottaram, L. Johnston, E. Ganella, C. Pantelis, R. Kotagiri, and A. Zalesky. Spatio-temporal dynamics of resting-state brain networks improve single-subject

- prediction of schizophrenia diagnosis. *Human Brain Mapping*, 39(9):3663–3681, 2018.
- [117] S. Kühn and J. Gallinat. Resting-state brain activity in schizophrenia and major depression: A quantitative meta-analysis. *Schizophrenia Bulletin*, 39(2):358–365, 2013.
- [118] J. Laney, K. Westlake, S. Ma, E. Woytowicz, and T. Adalı. Capturing subject variability in data driven fMRI analysis: A graph theoretical comparison. In *48th Annual Conference on Information Sciences and Systems (CISS)*, pages 1–6, March 2014.
- [119] J. Laney, K. P. Westlake, S. Ma, E. Woytowicz, V. D. Calhoun, and T. Adalı. Capturing subject variability in fMRI data: A graph-theoretical analysis of GICA vs. IVA. *Journal of Neuroscience Methods*, 247:32–40, 2015.
- [120] J.-H. Lee, T.-W. Lee, F. A. Jolesz, and S.-S. Yoo. Independent vector analysis (IVA): Multivariate approach for fMRI group study. *NeuroImage*, 40(1):86–109, 2008.
- [121] K. Lee, S. Tak, and J. C. Ye. A data-driven sparse GLM for fMRI analysis using sparse dictionary learning with MDL criterion. *IEEE Transactions on Medical Imaging*, 30(5):1076–1089, 2011.
- [122] S.-I. Lee, H. Lee, P. Abbeel, and A. Y. Ng. Efficient L_1 regularized logistic regression. In *Proceedings of the National Conference on Artificial Intelligence*, volume 6, pages 401–408, 2006.
- [123] T.-W. Lee, M. Girolami, and T. J. Sejnowski. Independent component analysis using an extended infomax algorithm for mixed subgaussian and supergaussian sources. *Neural Computation*, 11(2):417–441, 1999.

- [124] W. H. Lee, E. Bullmore, and S. Frangou. Quantitative evaluation of simulated functional brain networks in graph theoretical analysis. *Neuroimage*, 146:724–733, 2017.
- [125] S. Lefebvre, M. Demeulemeester, A. Leroy, C. Delmaire, R. Lopes, D. Pins, P. Thomas, and R. Jardri. Network dynamics during the different stages of hallucinations in schizophrenia. *Human brain mapping*, 37(7):2571–2586, 2016.
- [126] Y. Levin-Schwartz, V. D. Calhoun, and T. Adalı. Quantifying the interaction and contribution of multiple datasets in fusion: Application to the detection of schizophrenia. *IEEE Transactions on Medical Imaging*, 36(7):1385–1395, 2017.
- [127] K. Li, L. Guo, J. Nie, G. Li, and T. Liu. Review of methods for functional brain connectivity detection using fMRI. *Computerized Medical Imaging and Graphics*, 33(2):131–139, 2009.
- [128] X.-L. Li and T. Adalı. Blind spatiotemporal separation of second and/or higher-order correlated sources by entropy rate minimization. In *2010 IEEE International Conference on Acoustics Speech and Signal Processing (ICASSP)*, pages 1934–1937, March 2010.
- [129] X.-L. Li and T. Adalı. Independent component analysis by entropy bound minimization. *IEEE Transactions on Signal Processing*, 58(10):5151–5164, Dec. 2010.
- [130] X.-L. Li, S. Ma, V. D. Calhoun, and T. Adalı. Order detection for fMRI analysis: Joint estimation of downsampling depth and order by information theoretic criteria. In *2011 IEEE International Symposium on Biomedical Imaging: From Nano to Macro*, pages 1019–1022, April 2011.
- [131] X.-L. Li and X.-D. Zhang. Nonorthogonal joint diagonalization free of degenerate solution. *IEEE Transactions on Signal Processing*, 55(5):1803–1814, May 2007.

- [132] Y.-O. Li, T. Adalı, and V. D. Calhoun. Estimating the number of independent components for functional magnetic resonance imaging data. *Human Brain Mapping*, 28(11):1251–1266, 2007.
- [133] Y.-O. Li, T. Adalı, W. Wang, and V. D. Calhoun. Joint blind source separation by multiset canonical correlation analysis. *IEEE Transactions on Signal Processing*, 57(10):3918–3929, 2009.
- [134] E.-M. Løberg, M. Nygård, S. Helle, J. Ø. Berle, E. Johnsen, R. Kroken, H. Jørgensen, and K. Hugdahl. An fmri study of neuronal activation in schizophrenia patients with and without previous cannabis use. *Frontiers in Psychiatry*, 3:94, 2012.
- [135] E. F. Lock, K. A. Hoadley, J. S. Marron, and A. B. Nobel. Joint and individual variation explained (JIVE) for integrated analysis of multiple data types. *The Annals of Applied Statistics*, 7(1):523, 2013.
- [136] Q. Long, S. Bhinge, V. D. Calhoun, and T. Adalı. Independent vector analysis for common subspace analysis: Application to multi-subject fMRI data yields meaningful subgroups of schizophrenia. *NeuroImage*, page 116872, 2020.
- [137] Q. Long, S. Bhinge, Y. Levin-Schwartz, Z. Boukouvalas, V. D. Calhoun, and T. Adalı. The role of diversity in data-driven analysis of multi-subject fMRI data: Comparison of approaches based on independence and sparsity using global performance metrics. *Human Brain Mapping*, 40(2):489–504, 2019.
- [138] Q. Long, S. Bhinge, Y. Levin-Schwartz, V. D. Calhoun, and T. Adalı. A graph theoretical approach for performance comparison of ICA for fMRI analysis. In *Infor-*

mation Sciences and Systems (CISS), 2017 51st Annual Conference on, pages 1–6, 2017.

- [139] M.-E. Lynall, D. S. Bassett, R. Kerwin, P. J. McKenna, M. Kitzbichler, U. Muller, and E. Bullmore. Functional connectivity and brain networks in schizophrenia. *Journal of Neuroscience*, 30(28):9477–9487, 2010.
- [140] S. Ma, V. D. Calhoun, T. Eichele, W. Du, and T. Adalı. Modulations of functional connectivity in the healthy and schizophrenia groups during task and rest. *NeuroImage*, 62(3):1694–1704, Sep. 2012.
- [141] S. Ma, V. D. Calhoun, R. Phlypo, and T. Adalı. Dynamic changes of spatial functional network connectivity in healthy individuals and schizophrenia patients using independent vector analysis. *NeuroImage*, 90:196–206, 2014.
- [142] J. Mairal, F. Bach, J. Ponce, and G. Sapiro. Online learning for matrix factorization and sparse coding. *Journal of Machine Learning Research*, 11(Jan):19–60, 2010.
- [143] D. Malaspina, J. Harkavy-Friedman, C. Corcoran, L. Mujica-Parodi, D. Printz, J. M. Gorman, and R. Van Heertum. Resting neural activity distinguishes subgroups of schizophrenia patients. *Biological Psychiatry*, 56(12):931–937, 2004.
- [144] D. S. Manoach. Prefrontal cortex dysfunction during working memory performance in schizophrenia: Reconciling discrepant findings. *Schizophrenia Research*, 60(2-3):285–298, 2003.
- [145] H. A. Marusak, V. D. Calhoun, S. Brown, L. M. Crespo, K. Sala-Hamrick, I. H. Gotlib, and M. E. Thomason. Dynamic functional connectivity of neurocognitive networks in children. *Human brain mapping*, 38(1):97–108, 2017.

- [146] A. R. McIntosh, N. Kovacevic, and R. J. Itier. Increased brain signal variability accompanies lower behavioral variability in development. *PLoS computational biology*, 4(7), 2008.
- [147] M. J. Mckeown, S. Makeig, G. G. Brown, T.-P. Jung, S. S. Kindermann, A. J. Bell, and T. J. Sejnowski. Analysis of fMRI data by blind separation into independent spatial components. *Human Brain Mapping*, 6:160–188, 1998.
- [148] A. Michael, M. Anderson, R. Miller, T. Adali, and V. D. Calhoun. Preserving subject variability in group fMRI analysis: Performance evaluation of GICA versus IVA. *Frontiers in Systems Neuroscience*, 8:106–123, 2014.
- [149] G. Mingoa, G. Wagner, K. Langbein, R. Maitra, S. Smesny, M. Dietzek, H. P. Burmeister, J. R. Reichenbach, R. G. Schlösser, C. Gaser, et al. Default mode network activity in schizophrenia studied at resting state using probabilistic ICA. *Schizophrenia Research*, 138(2-3):143–149, 2012.
- [150] B. Morar, J. C. Badcock, M. Phillips, O. P. Almeida, and A. Jablensky. The longevity gene Klotho is differentially associated with cognition in subtypes of schizophrenia. *Schizophrenia Research*, 193:348–353, 2018.
- [151] A. Mubarik and H. Tohid. Frontal lobe alterations in schizophrenia: A review. *Trends in Psychiatry and Psychotherapy*, 38(4):198–206, 2016.
- [152] A. Mucci, S. Galderisi, B. Kirkpatrick, P. Bucci, U. Volpe, E. Merlotti, F. Centanaro, F. Catapano, and M. Maj. Double dissociation of N1 and P3 abnormalities in deficit and nondeficit schizophrenia. *Schizophrenia Research*, 92(1-3):252–261, 2007.
- [153] M. E. Newman. Modularity and community structure in networks. *Proceedings of the National Academy of Sciences*, 103(23):8577–8582, 2006.

- [154] F. Nielsen and R. Nock. A closed-form expression for the Sharma–Mittal entropy of exponential families. *Journal of Physics A: Mathematical and Theoretical*, 45(3):023003, 2011.
- [155] B.-y. Park, T. Moon, and H. Park. Dynamic functional connectivity analysis reveals improved association between brain networks and eating behaviors compared to static analysis. *Behavioural brain research*, 337:114–121, 2018.
- [156] R. D. Pascual-Marqui, D. Lehmann, T. Koenig, K. Kochi, M. C. Merlo, D. Hell, and M. Koukkou. Low resolution brain electromagnetic tomography (LORETA) functional imaging in acute, neuroleptic-naive, first-episode, productive schizophrenia. *Psychiatry Research: Neuroimaging*, 90(3):169–179, 1999.
- [157] R. S. Patel, F. D. Bowman, and J. K. Rilling. Determining hierarchical functional networks from auditory stimuli fMRI. *Human Brain Mapping*, 27(5):462–470, 2006.
- [158] H. Peng, F. Long, and C. Ding. Feature selection based on mutual information criteria of max-dependency, max-relevance, and min-redundancy. *IEEE Transactions on Pattern Analysis and Machine Intelligence*, 27(8):1226–1238.
- [159] W. M. Perlstein, C. S. Carter, D. C. Noll, and J. D. Cohen. Relation of prefrontal cortex dysfunction to working memory and symptoms in schizophrenia. *American Journal of Psychiatry*, 158(7):1105–1113, 2001.
- [160] M. Pievani, W. de Haan, T. Wu, W. W. Seeley, and G. B. Frisoni. Functional network disruption in the degenerative dementias. *The Lancet Neurology*, 10(9):829–843, 2011.
- [161] S. P. Ponnappalli, M. A. Saunders, C. F. Van Loan, and O. Alter. A higher-order gen-

- eralized singular value decomposition for comparison of global mRNA expression from multiple organisms. *PLoS ONE*, 6(12):e28072+, Dec. 2011.
- [162] B. Rashid, E. Damaraju, G. D. Pearlson, and V. D. Calhoun. Dynamic connectivity states estimated from resting fMRI identify differences among schizophrenia, bipolar disorder, and healthy control subjects. *Frontiers in Human Neuroscience*, 8:897, 2014.
- [163] S. Robinson, G. Basso, N. Soldati, U. Sailer, J. Jovicich, L. Bruzzone, I. Kryspin-Exner, H. Bauer, and E. Moser. A resting state network in the motor control circuit of the basal ganglia. *BMC Neuroscience*, 10(1):1, 2009.
- [164] M. Rubinov and O. Sporns. Complex network measures of brain connectivity: Uses and interpretations. *NeuroImage*, 52(3):1059–1069, 2010.
- [165] C. C. Schultz, K. Koch, G. Wagner, I. Nenadic, C. Schachtzabel, D. Güllmar, J. R. Reichenbach, H. Sauer, and R. G. Schlösser. Reduced anterior cingulate cognitive activation is associated with prefrontal–temporal cortical thinning in schizophrenia. *Biological Psychiatry*, 71(2):146–153, 2012.
- [166] A. Scott, W. Courtney, D. Wood, R. De la Garza, S. Lane, R. Wang, M. King, J. Roberts, J. A. Turner, and V. D. Calhoun. COINS: An innovative informatics and neuroimaging tool suite built for large heterogeneous datasets. *Frontiers in Neuroinformatics*, 5:33, 2011.
- [167] S. Senn. Statistical pitfalls of personalized medicine. *Nature*, 563:619–621, 2018.
- [168] J. M. Sheffield and D. M. Barch. Cognition and resting-state functional connectivity in schizophrenia. *Neuroscience & Biobehavioral Reviews*, 61:108–120, 2016.

- [169] C. Sheng, M. Xia, H. Yu, Y. Huang, Y. Lu, F. Liu, Y. He, and Y. Han. Abnormal global functional network connectivity and its relationship to medial temporal atrophy in patients with amnesic mild cognitive impairment. *PloS one*, 12(6):e0179823, 2017.
- [170] M. E. Shenton, R. Kikinis, F. A. Jolesz, S. D. Pollak, M. LeMay, C. G. Wible, H. Hokama, J. Martin, D. Metcalf, M. Coleman, et al. Abnormalities of the left temporal lobe and thought disorder in schizophrenia: A quantitative magnetic resonance imaging study. *New England Journal of Medicine*, 327(9):604–612, 1992.
- [171] J. Shin, S. Ahn, and X. Hu. Correction for the T1 effect incorporating flip angle estimated by Kalman filter in cardiac-gated functional MRI. *Magnetic Resonance in Medicine*, 70(6):1626–1633, 2013.
- [172] S. M. Silverstein, S. Berten, B. Essex, I. Kovacs, T. Susmaras, and D. M. Little. An fMRI examination of visual integration in schizophrenia. *Journal of Integrative Neuroscience*, 8(02):175–202, 2009.
- [173] K. E. Stephan, K. J. Friston, and C. D. Frith. Dysconnection in schizophrenia: From abnormal synaptic plasticity to failures of self-monitoring. *Schizophrenia Bulletin*, 35(3):509–527, 2009.
- [174] J. Sui, T. Adalı, G. Pearlson, H. Yang, S. R. Sponheim, T. White, and V. D. Calhoun. A CCA+ICA based model for multi-task brain imaging data fusion and its application to schizophrenia. *NeuroImage*, 51:123 – 134, 2010.
- [175] J. Sui, T. Adalı, G. D. Pearlson, and V. D. Calhoun. An ICA-based method for the identification of optimal fMRI features and components using combined group-discriminative techniques. *NeuroImage*, 46(1):73–86, 2009.

- [176] J. Sui, T. Adalı, Q. Yu, J. Chen, and V. D. Calhoun. A review of multivariate methods for multimodal fusion of brain imaging data. *Journal of Neuroscience Methods*, 204(1):68 – 81, 2012.
- [177] H. Takahashi, M. Koeda, K. Oda, T. Matsuda, E. Matsushima, M. Matsuura, K. Asai, and Y. Okubo. An fMRI study of differential neural response to affective pictures in schizophrenia. *NeuroImage*, 22(3):1247–1254, 2004.
- [178] Q. K. Telesford, J. H. Burdette, and P. J. Laurienti. An exploration of graph metric reproducibility in complex brain networks. *Frontiers in neuroscience*, 7, 2013.
- [179] P.-C. Tu, J.-C. Hsieh, C.-T. Li, Y.-M. Bai, and T.-P. Su. Cortico-striatal disconnection within the cingulo-opercular network in schizophrenia revealed by intrinsic functional connectivity analysis: a resting fmri study. *Neuroimage*, 59(1):238–247, 2012.
- [180] J. A. Turner, E. Damaraju, T. G. Van Erp, D. H. Mathalon, J. M. Ford, J. Voyvodic, B. A. Mueller, A. Belger, J. Bustillo, S. C. McEwen, et al. A multi-site resting state fMRI study on the amplitude of low frequency fluctuations in schizophrenia. *Frontiers in neuroscience*, 7:137, 2013.
- [181] L. Q. Uddin, K. S. Supekar, S. Ryali, and V. Menon. Dynamic reconfiguration of structural and functional connectivity across core neurocognitive brain networks with development. *Journal of Neuroscience*, 31(50):18578–18589, 2011.
- [182] V. G. van de Ven, E. Formisano, D. Prvulovic, C. H. Roeder, and D. E. Linden. Functional connectivity as revealed by spatial independent component analysis of fMRI measurements during rest. *Human brain mapping*, 22(3):165–178, 2004.

- [183] M. P. Van Den Heuvel and H. E. H. Pol. Exploring the brain network: A review on resting-state fMRI functional connectivity. *European Neuropsychopharmacology*, 20(8):519–534, 2010.
- [184] K. Van Deun, I. Van Mechelen, L. Thorrez, M. Schouteden, B. De Moor, M. J. van der Werf, L. De Lathauwer, A. K. Smilde, and H. A. Kiers. DISCO-SCA and properly applied GSVD as swinging methods to find common and distinctive processes. *PLoS One*, 7(5):e37840, 2012.
- [185] H. H. van Hell, M. Vink, L. Ossewaarde, G. Jager, R. S. Kahn, and N. F. Ramsey. Chronic effects of cannabis use on the human reward system: an fmri study. *European neuropsychopharmacology*, 20(3):153–163, 2010.
- [186] G. Varoquaux, A. Gramfort, F. Pedregosa, V. Michel, and B. Thirion. Multi-subject dictionary learning to segment an atlas of brain spontaneous activity. In *Biennial International Conference on Information Processing in Medical Imaging*, pages 562–573, 2011.
- [187] P. E. Vértes, A. F. Alexander-Bloch, N. Gogtay, J. N. Giedd, J. L. Rapoport, and E. T. Bullmore. Simple models of human brain functional networks. *Proceedings of the National Academy of Sciences*, 109(15):5868–5873, 2012.
- [188] V. A. Vorobyev, K. Alho, S. V. Medvedev, S. V. Pakhomov, M. S. Roudas, J. M. Rutkovskaya, M. Tervaniemi, T. L. Van Zuijen, and R. Näätänen. Linguistic processing in visual and modality-nonspecific brain areas: PET recordings during selective attention. *Cognitive Brain Research*, 20(2):309–322, 2004.
- [189] S. Weber, E. Johnsen, R. A. Kroken, E.-M. Løberg, S. Kandilarova, D. Stoyanov, K. Kompus, and K. Hugdahl. Dynamic functional connectivity patterns in

- schizophrenia and the relationship with hallucinations. *Frontiers in psychiatry*, 11:227, 2020.
- [190] M. N. Wernick, Y. Yang, J. G. Brankov, G. Yourganov, and S. C. Strother. Machine learning in medical imaging. *IEEE Signal Processing Magazine*, 27(4):25–38, 2010.
- [191] H. C. Whalley, V.-E. Gountouna, J. Hall, A. McIntosh, M.-C. Whyte, E. Simonotto, D. E. Job, D. G. Owens, E. C. Johnstone, and S. M. Lawrie. Correlations between fMRI activation and individual psychotic symptoms in un-medicated subjects at high genetic risk of schizophrenia. *BMC Psychiatry*, 7(1):61, 2007.
- [192] X. Wu, R. Li, A. S. Fleisher, E. M. Reiman, X. Guan, Y. Zhang, K. Chen, and L. Yao. Altered default mode network connectivity in alzheimer’s diseasea resting functional mri and bayesian network study. *Human brain mapping*, 32(11):1868–1881, 2011.
- [193] Q. Yu, E. B. Erhardt, J. Sui, Y. Du, H. He, D. Hjelm, M. S. Cetin, S. Rachakonda, R. L. Miller, G. Pearlson, et al. Assessing dynamic brain graphs of time-varying connectivity in fMRI data: Application to healthy controls and patients with schizophrenia. *NeuroImage*, 107:345–355, 2015.
- [194] A. Zalesky, A. Fornito, and E. T. Bullmore. Network-based statistic: Identifying differences in brain networks. *NeuroImage*, 53(4):1197–1207, 2010.
- [195] Y.-F. Zang, Y. He, C.-Z. Zhu, Q.-J. Cao, M.-Q. Sui, M. Liang, L.-X. Tian, T.-Z. Jiang, and Y.-F. Wang. Altered baseline brain activity in children with ADHD revealed by resting-state functional MRI. *Brain and Development*, 29(2):83–91, 2007.
- [196] W. Zhang, S. Li, X. Wang, Y. Gong, L. Yao, Y. Xiao, J. Liu, S. K. Keedy, Q. Gong, J. A. Sweeney, et al. Abnormal dynamic functional connectivity between speech and

auditory areas in schizophrenia patients with auditory hallucinations. *NeuroImage: Clinical*, 19:918–924, 2018.

- [197] D. Zhi, X. Ma, L. Lv, Q. Ke, Y. Yang, X. Yang, M. Pan, S. Qi, R. Jiang, Y. Du, et al. Abnormal dynamic functional network connectivity and graph theoretical analysis in major depressive disorder. pages 558–561, 2018.
- [198] Y. Zhou, M. Liang, T. Jiang, L. Tian, Y. Liu, Z. Liu, H. Liu, and F. Kuang. Functional dysconnectivity of the dorsolateral prefrontal cortex in first-episode schizophrenia using resting-state fmri. *Neuroscience letters*, 417(3):297–302, 2007.
- [199] Q.-H. Zou, C.-Z. Zhu, Y. Yang, X.-N. Zuo, X.-Y. Long, Q.-J. Cao, Y.-F. Wang, and Y.-F. Zang. An improved approach to detection of amplitude of low-frequency fluctuation (ALFF) for resting-state fMRI: Fractional ALFF. *Journal of neuroscience methods*, 172(1):137–141, 2008.

